UNIVERSIDADE FEDERAL DO PARANÁ
ADELITA CAROLINA RODRIGUES

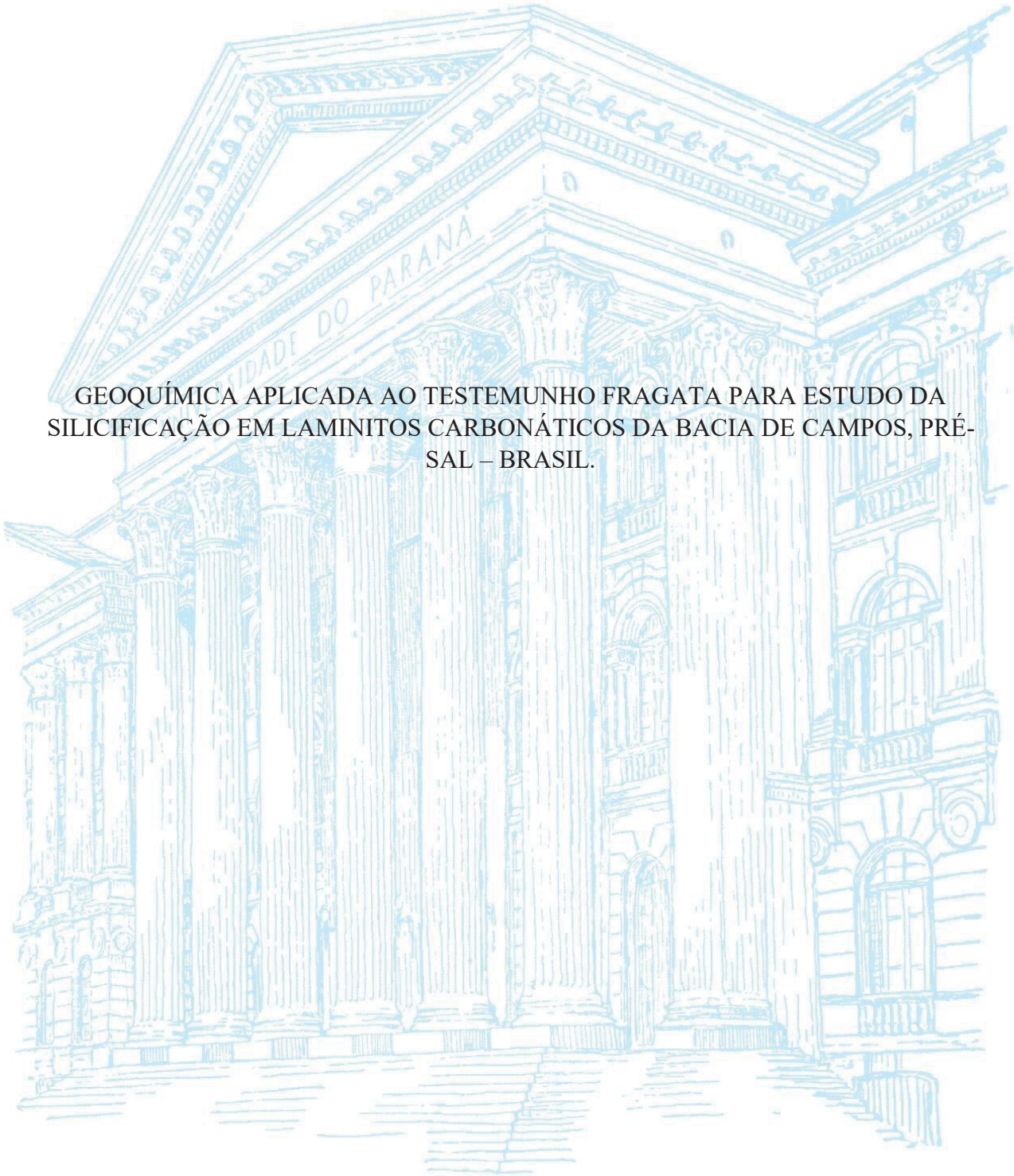

GEOQUÍMICA APLICADA AO TESTEMUNHO FRAGATA PARA ESTUDO DA SILICIFICAÇÃO EM LAMINITOS CARBONÁTICOS DA BACIA DE CAMPOS, PRÉ-SAL – BRASIL.

CURITIBA
2023

ADELITA CAROLINA RODRIGUES

GEOQUÍMICA APLICADA AO TESTEMUNHO FRAGATA PARA ESTUDO DA SILICIFICAÇÃO EM LAMINITOS CARBONÁTICOS DA BACIA DE CAMPOS, PRÉ-SAL – BRASIL.

Dissertação apresentada ao Programa de pós Graduação em Geologia, Setor de Ciências da Terra da Universidade Federal do Paraná, como requerimento para obtenção do título de Mestre em Geologia.

Orientação: Profª. Dra. Anelize Manuela Bahniuk Rumbelsperger.
Coorientação: Dra. Larissa da Rocha Santos.

CURITIBA

2023

DADOS INTERNACIONAIS DE CATALOGAÇÃO NA PUBLICAÇÃO (CIP)
UNIVERSIDADE FEDERAL DO PARANÁ
SISTEMA DE BIBLIOTECAS – BIBLIOTECA DE CIÊNCIA E TECNOLOGIA

Rodrigues, Adelita Carolina
Geoquímica aplicada ao testemunho Fragata para estudo da silicificação em laminitos carbonáticos da Bacia de Campos, Pré-sal – Brasil / Adelita Carolina Rodrigues. – Curitiba, 2023.
1 recurso on-line: PDF.

Dissertação (Mestrado) - Universidade Federal do Paraná, Setor de Ciências da Terra, Programa de Pós-Graduação em Geologia.

Orientador: Anelize Manuela Bahniuk Rumbelsperger
Coorientador: Larissa da Rocha Santos

1. Carbonatos. 2. Hidrocarbonetos. 3. Bacias sedimentares. 4. Pré-sal – Brasil. I. Universidade Federal do Paraná. II. Programa de Pós-Graduação em Geologia. III. Rumbelsperger, Anelize Manuela Bahniuk. IV. Santos, Larissa da Rocha. V. Título.

Bibliotecário: Elias Barbosa da Silva CRB-9/1894

MINISTÉRIO DA EDUCAÇÃO
SETOR DE CIENCIAS DA TERRA
UNIVERSIDADE FEDERAL DO PARANÁ
PRÓ-REITORIA DE PESQUISA E PÓS-GRADUAÇÃO
PROGRAMA DE PÓS-GRADUAÇÃO GEOLOGIA - 40001016028P

TERMO DE APROVAÇÃO

Os membros da Banca Examinadora designada pelo Colegiado do Programa de Pós-Graduação GEOLOGIA da Universidade Federal do Paraná foram convocados para realizar a arguição da dissertação de Mestrado de **ADELITA CAROLINA RODRIGUES** intitulada: **GEOQUÍMICA APLICADA AO TESTEMUNHO FRAGATA PARA ESTUDO DA SILICIFICAÇÃO EM LAMINITOS CARBONÁTICOS DA BACIA DE CAMPOS, PRÉ-SAL BRASIL**, sob orientação da Profa. Dra. ANELIZE MANUELA BAHNIUK RUMBELSPERGER, que após terem inquirido a aluna e realizada a avaliação do trabalho, são de parecer pela sua APROVAÇÃO no rito de defesa.

A outorga do título de mestra está sujeita à homologação pelo colegiado, ao atendimento de todas as indicações e correções solicitadas pela banca e ao pleno atendimento das demandas regimentais do Programa de Pós-Graduação.

CURITIBA, 27 de Junho de 2023.

Assinatura Eletrônica
30/06/2023 15:16:20.0
ANELIZE MANUELA BAHNIUK RUMBELSPERGER
Presidente da Banca Examinadora

Assinatura Eletrônica
29/06/2023 14:09:52.0
LEONARDO FADEL CURY
Avaliador Interno (UNIVERSIDADE FEDERAL DO PARANÁ)

Assinatura Eletrônica 29/08/2023 13:22:03.0
JOACHIM EMIL AMTHOR
Avaliador Externo (RWTH AACHEN UNIVERSITY)

ACKNOWLEDGEMENTS

I express my gratitude to the Federal University of Paraná for my academic degree in geology and to the team of professors & geologists associated with the geology department (DEGEOL/UFPR) for all guidance and teaching during my student time. In special, I want to thank Professor *Dra. Anelize Manuela Bahniuk Rumbelsperger,* my closest advisor, for guidance and support during the years we worked together. I also direct a special thanks to *Dra. Larissa da Rocha Santos* as my co-author in my first published scientific research and my closest advisor with *Anelize*. I hope that together we will continue to contribute to science.

I am grateful to Lamir Institute (iLamir UFPR) for hosting me and allowing me to conduct scientific geoscience research. I also thank the iLamir collaborators team for their support, partnership, and friendship. I am very grateful for the social assistance provided by the PRAE/UFPR (Dean of student affairs at UFPR) through the PROBEM scholarship that allowed me access to the graduation curse, enabling me to obtain a bachelor's degree in geology.

Furthermore, I am grateful for the two projects that support my scholarship and analysis for my master dissertation: 1) DIAGENESIS - *Diagenesis of Pre-Salt non-marine carbonate sequences and its impact on Exploration and Production of hydrocarbon reservoir*, Shell Brazil, for the financial resources in analytical procedures and scholarship (04/21 to 10/22); (2) GeoQI - *High-Resolution Geochemical Characterization in the Aptian Sequence of the Santos Basin (through the technique of Clustered Isotopes and Sr in situ)* for scholarship in the last months (11/22 to 06/23). Both projects are a Technical-Scientific Cooperation with the Paraná Federal University (UFPR) / Institute LAMIR, as a part of the supporting program on scientific research and technological development applied to the petroleum, natural gas, and biofuel industry in Brazil, in compliance with the provisions of Law 9,478 of August 6, 1997 (Petroleum Law) and Clause 22.2 of the Concession Contract executed with ANP – the National Petroleum, Natural Gas, and Biofuel Agency. I also thank ANP for providing the studied material allowing sampling and destructive analysis [SEI/ANP – Official document number 424/2019/SDT-e-ANP. Process number 48610.211854/2019-70].

I thank *André*, *Kamilla & Ademar Rodrigues*, and *Adriana & Cezar Nemetz* for personal support during this academic journey. I especially thank *Lucas Nemetz,* who has been by my side. *And in memory of Vilma Beatriz Kaujon Rodrigues,* I express my gratitude for my life.

My gratitude to all collaborators and institutions involved in this research:

DIAGENESIS PROJECT – [Grant number 23075.193990/2017-07]

Joachim E. Amthor (Shell)

Leonardo Fadel Cury

Anelize Manuela Bahniuk Rumbelsperger

GeoQI PROJECT – [23075.039121/2022-97]

Felipe Farias (Petrobras)

Anelize Manuela Bahniuk Rumbelsperger

Leonardo Fadel Cury

FRAGATA WELL PREVIOUS STUDIES

Almério França, Felipe Varejão

MATERIAL AVAILABILITY:

ANP (Agência Nacional do Petróleo)

INFRASTRUCTURE:

Lamir Institute (Laboratório de Análises de Minerais e Rochas)

DEGEOL | CT | UFPR (Departamento de Geologia, Setor Ciências da Terra, Universidade Federal do Paraná)

ADMINISTRATIVE SUPPORT:

Adriana Nascimento, Rodrigo Barbosa, Rosemari Fabianovicz

Bianca Luciano, Estela Dagma, Maria Eduarda dos Santos

SAMPLE PREPARATION:

Ivan Bindo, Bruno Cunha, Flávio Perraro – Tungsten carbide mil powdered samples

Flávia Afonso, Shirley Cezar – Conventional and double-polished thin sections

ANALYTICAL TECHNIQUES:

Ana Maria Guerreiro Antunes - Scanning electron microscopic (SEM-EDX)

Leandro Keiji Ozahata - X-ray computed microtomography analysis (μCT)

Guilherme Fedalto – X-ray diffration, Fluid inclusion (Test procedures)

Franciele Czerzinski, Inaiara Casapula – X-ray fluorescence

Diego Portela, Luis Mancini – Carbon and Oxygen Stable Isotopes, Clumped Isotopes (Test procedures)

Joicy Micheletto – Sr Isotopes (Test procedures)

ADITIONAL SUPPORT IN ANALYTICAL TECHNIQUES:

Israel Bini, Celene Candido| CTAF/UFPR (Centro de Tecnologias Avançadas em Fluorescência)

Luis G. Santos, Paula Ferreira, Rosangela Freitas | CME/UFPR (Centro de Microscopia eletrônica)

Antoine G. Cremiere | Caltech (California Institute of Technology)

EVENTUAL SUPPORT AND DISCUSSIONS – DEGEOL|UFPR CLASSMATES

Carolina Velenzuela, Guido Alonso, Joyce Rodrigues, Malton Fraga, Paulo Quezada, Tatiana Stepanenko.

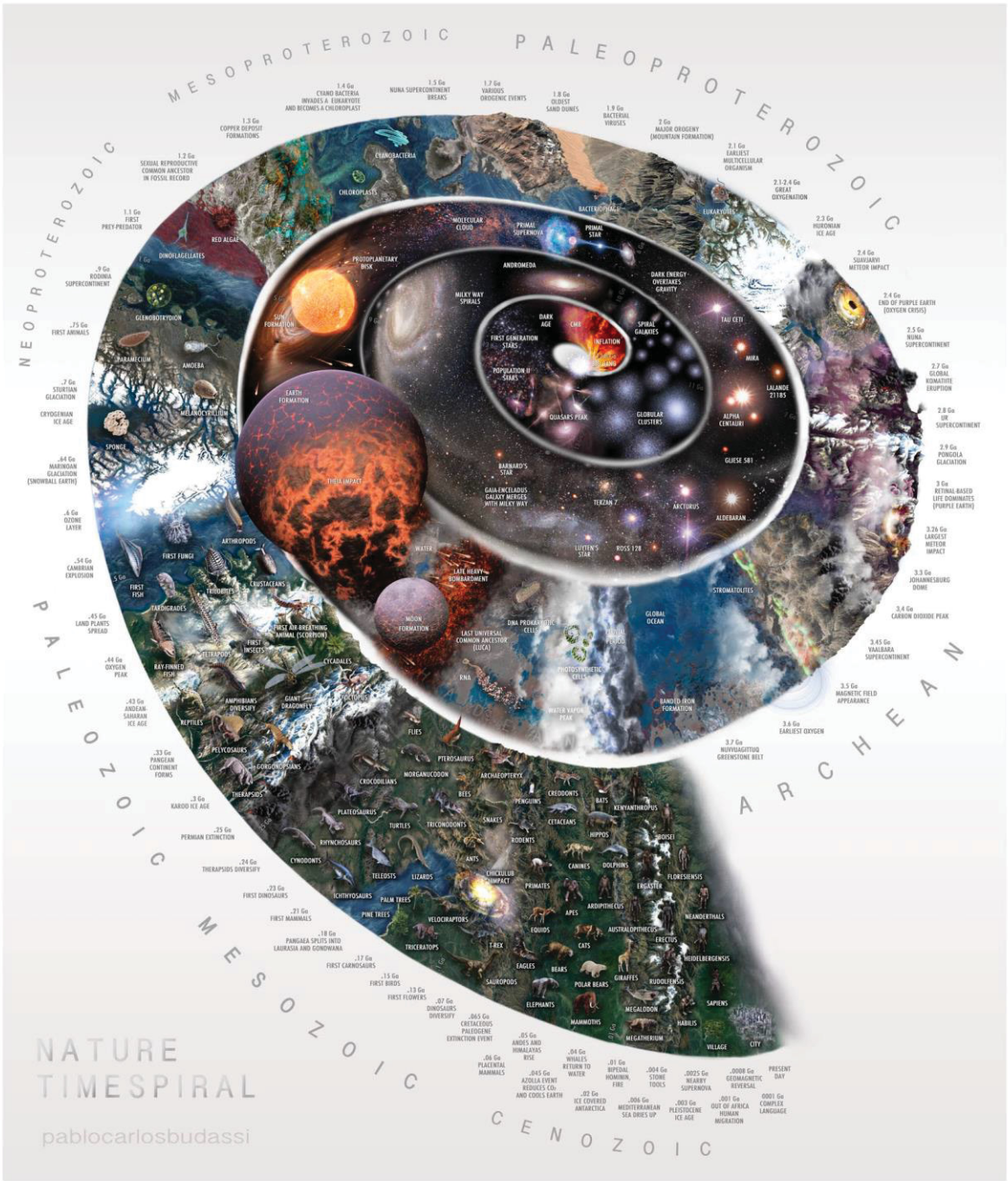

Nature Timespiral.

Pablo Carlos Budassi (2022)

"Isn't life exciting! Everything can change all of a sudden and for no reason at all!"

Moomintroll, in: Moominpappa at Sea, by Tove Jansson (1965).

RESUMO

Os reservatórios de hidrocarbonetos são importantes para o desenvolvimento da sociedade como fonte de combustível e matéria-prima em produtos industriais. Portanto, entender esses reservatórios quanto à deposição, diagênese e influência dos processos tectônicos é essencial para uma melhor explotação. Nesse contexto, o Pré-sal brasileiro está entre as maiores reservas do mundo, com gênese relacionada à separação das placas tectônicas sul-americana e africana durante a formação do Oceano Atlântico, no rompimento do continente Gondwana desde o Jurássico Superior até o Cretáceo Inferior. Esta pesquisa visa contribuir para o conhecimento dos reservatórios de hidrocarbonetos, fornecendo uma caracterização detalhada das feições diagenéticas e da circulação de fluidos, enfatizando a silicificação que impacta significativamente a permeabilidade e porosidade dos reservatórios, e os processos de sulfetação que afetam a qualidade dos hidrocarbonetos. Este trabalho apresenta um estudo de caso do testemunho Fragata [6DEV-18PA-RJS] da Sequência Transicional - Bacia de Campos (Fm. Macabú), com três testemunhos selecionados para análise laboratorial em termos de petrografia (ótica, fluorescência UV e microscopia eletrônica de varredura), mineralogia (difração de raios X), química (fluorescência de raios X) e espectrometria de isótopos estáveis de carbono e oxigênio. A litologia principal nas amostras do Fragata consiste em carbonatos laminados compostos de calcita, Mg-calcita, Ca-dolomita/anquerita, sílica, traços de barita, pirita, gypsita e halita. Em resumo, três feições texturais caracterizam a sílica: (1) Chert (Granular Cripto/Microcristalina) – ocorre associado a minerais carbonáticos, como esferulitos de calcita e Mg-calcita com substituição parcial, além de Ca-dolomita/anquerita romboédrica e em sela, em cristais dispersos; (2) Calcedônia (Fibrosa Cripto /Microcristalina) – de cor branca, altamente associada com halita (NaCl) cimentando porosidades vugulares e canais, geralmente com um eixo-c perpendicular à parede da porosidade, ou formando esferóides; (3) Mega-Quartzo (Granular macrocristalino) – Cresce quando há espaço, apresentando uma fina textura cristalina com aspecto transparente e limpo, preenchendo parcialmente a porosidade remanescente. A mineralógia das amostras termina com sulfetos (pirita cubica e octaédrica) e sulfatos (barita, Sr-barita e gypsita), preenchendo as porosidades remanescentes, junto com a matéria orgânica amorfa (Carbono). Os principais resultados obtidos nesta pesquisa sugerem uma fase de silicificação relacionada a um processo pós-deposicional para o caso Fragata. A principal evidência considerada é a relação petrográfica entre cristais de carbonato e sílica, sendo que a entrada de silica no sistema ocorre após certo grau de compactação, estilolitização e dolomitização. Com base na literatura sobre o Pré-sal, a fonte mais provável para a disponibilidade de sílica é a circulação de fluidos através do vulcanismo toleítico e depósitos siliciclásticos das camadas adjacentes (Sequência Rift - Fm. Cabiúnas e Itabapoana) com possível dissolução sob influência de processos termogênicos, migração de sílica remanescente e precipitação com resfriamento. As últimas fases minerais indicam migração de matéria orgânica, com liberação de enxofre em reação química com fases evaporíticas (anidrita), permitindo estimar fO2, pH e temperatura.

Palavras-chave: Pré-sal; carbonatos; silicificação; reservatórios de hidrocarbonetos; bacias sedimentares.

ABSTRACT

Hydrocarbon reservoirs are important for society's development as a source of fuel and raw materials in industrial products. Therefore, understanding these reservoirs regarding deposition, diagenesis, and tectonic processes influence is essential to better exploitation. In this context, the Brazilian Pre-salt is among the largest reserves in the world, with genesis related to South American and African tectonic plates separated during Atlantic Ocean formation when the Gondwana continent breakup from Late Jurassic until the Early Cretaceous. This research aims to contribute to hydrocarbon reservoir knowledge, providing a detailed characterization of diagenetic and fluid circulation features, emphasizing silicification that significantly impacts reservoirs' permeability and porosity, and sulfidation processes that affect the hydrocarbon quality. This work presents a case study of the Fragata well [6DEV-18PA-RJS] from Transitional Sequence - Campos Basin (Macabú Fm.), with three core samples selected for laboratory analysis in terms of petrography (optical, UV fluorescence, and scanning electron microscopy), mineralogy (X-Ray Diffraction), chemistry (X-Ray Fluorescence), and Carbon & Oxygen stable isotopes spectrometry. The main lithology in Fragata samples consists of laminated carbonates composed of calcite, Low Mg-calcite, Ca-dolomite/ankerite and silica, traces of barite, pyrite, gypsum, and halite. In summary, three textural features characterize the silica: (1) Chert (Granular Crypto/Microcrystalline) – occurs associated with carbonates minerals, such as spherulite of calcite and Low-Mg calcite with partial replacement, in addition to the saddle, and rhomb Ca-dolomite/ankerite, dispersed with a floating structure; (2) Chalcedony (Fibrous Crypto/Microcrystalline) – white in color, highly associated with halite (NaCl) cementing vuggy and channels porosities, usually with a c-axis perpendicular to the porosity wall, or forming spheroids; (3) Mega-Quartz (Granular macrocrystalline) – Growing when space is available, showing a fine crystalline texture with a transparent and clean aspect, partially filling the remaining porosity. The mineralogical assemblage of the samples ends with sulfides (hexagonal and octahedron pyrite) and sulfates (barite, Sr-barite, and gypsum), filling the remaining porosities associated with amorphous organic matter (Carbon). The main results obtained through this research suggest a silicification phase related to a post-depositional process for the Fragata case. The main evidence considered is the petrographic relation between carbonate crystals and silica, with the silica layers probably entering the system after some degree of compaction, stylolitization, and dolomitization. Based on the Pre-salt previous literature, the most likely source for silica availability is fluid circulation through the tholeiitic volcanism and siliciclastic deposits from adjacent layers (Rift Sequence – Cabiúnas and Itabapoana Fm.) with possible dissolution under thermogenic process influence, remaining silica migration and precipitation with cooling. The last mineral phases indicate organic matter migration, with sulfur liberation in a chemical reaction with evaporite phases (anhydrite), allowing fO_2, pH, and temperature estimation.

Keywords: Pre-salt; carbonates; silicification; hydrocarbon reservoirs; sedimentary basins.

SÚMARIO

ESTRUTURA DA DISSERTAÇÃO

A presente dissertação foi desenvolvida no Programa de Pós Graduação em Geologia da Universidade Federal do Paraná (PPGEOL|UFPR), como requerimento para obtenção do título de Mestre em Geologia. Sob orientação da Prof.ª Dra. Anelize Manuela Bahniuk Rumbelsperger e Coorientação da Dra. Larissa da Rocha Santos, com apoio e infraestrutura do Instituto Lamir, e financiamento pela Shell Brasil e Petrobras S.A. A dissertação segue o modelo alternativo do manual de normalização da UFPR 2022, e as diretrizes do PPGEOL|UFPR para publicação de capítulo em revista geocientífica, com a seguinte estrutura:

CHAPTER 1 – LITERATURE REVIEW: traz uma revisão do conhecimento atual sobre assembleias mineralógicas em ambientes sedimentares, com ênfase para carbonatos e sílica. Faz uma revisão sobre as classificações de nomenclatura que foram utilizadas nesta pesquisa.

CHAPTER 2 – GEOLOGICAL SETTINGS: traz uma revisão com o intuito de apresentar o contexto geológico e localização do Pré-Sal, no contexto da origem das bacias marginais brasileiras, durante a compartimentação do supercontinente Gondwana (Cretáceo).

CHAPTER 3 – METHODS: Apresenta métodos de preparação das amostras e as técnicas analíticas utilizadas durante as etapas de laboratório. Além de informações litológicas gerais do testemunho Fragata.

CHAPTER 4 – RESULTS: em formato de manuscrito para publicação em periódico de geociências, com foco no Jornal *"Marine and Petroleum Geology"*. Neste capitulo são apresentados resultados e discussões obtidos a partir de análises de detalhe em três amostras do testemunho Fragata. Com ênfase para a ordem de precipitação dos minerais, e nos processos de silicificação pós-deposicional.

DISSERTATION STRUCTURE

This dissertation was developed in the Postgraduate Program in Geology at the Federal University of Paraná (PPGEOL|UFPR) as a requirement to obtain a master's degree in Geology, under the guidance of Prof. Dr. Anelize Manuela Bahniuk Rumbelsperger and Dra. Larissa da Rocha Santos, with support and infrastructure from Lamir Institute and funding from Shell Brazil and Petrobras S.A. The dissertation follows the alternative model of the UFPR 2022 standardization manual and the PPGEOL|UFPR guidelines for publishing a chapter in a geoscientific journal and consists of the following structure:

CHAPTER 1 – LITERATURE REVIEW: reviews current knowledge about mineralogical assemblages in sedimentary environments, emphasizing carbonates and silica. It addresses an overview of the nomenclature classifications used in this research.

CHAPTER 2 – GEOLOGICAL SETTINGS: brings a review to present the Pre-Salt's geological settings and location, in the context of the Brazilian marginal basins origins, during the compartmentalization of the Gondwana supercontinent (Cretaceous).

CHAPTER 3 – METHODS: Presents sample preparation methods, analytical techniques used during laboratory steps, and general lithological data from Fragata.

CHAPTER 4 – RESULTS: presented in a manuscript format for publication in a geoscience journal, focusing on "*Marine and Petroleum Geology*". This chapter presents results and discussions from detailed analyses of three samples from the Fragata well, emphasizing the precipitation order of the observed minerals and the post-depositional silicification processes.

CHAPTER 1 – LITERATURE REVIEW

AUTIGENIC MINERALS: CARBONATES x SILICA

1 INTRODUCTION

This chapter presents a review of carbonates and silica, considering the current classification scheme according to genesis, framework features, and geological implications. In addition, this chapter aims to review basic concepts concerning minerals observed in sedimentary basins since the following chapters will present mineralogical assemblages observed in the Pre-salt section of the Brazilian marginal sedimentary basins. The specific goals are: (1) to provide a basic and summarized review of mineral groups and precipitation processes; (2) to review textural, structural, and morphological aspects to clarify the next chapters descriptions; (3) to present the more frequently accepted classifications also adopted as descriptive guides in the development of this research;

2 CARBONATES [$X(CO_3)_x$]: CLASSIFICATIONS AND GEOLOGICAL IMPLICATIONS

Carbonates refer to minerals formed from the ionic bond of a metal with the carbonate anion $(CO_3)^{-2}$. The carbonate sedimentary rocks precipitation can occur by chemical or biochemical processes in areas without significant deposition of clastic detritus (Dupraz et al., 2009; Flügel, 2010; Ford and Pedley, 1996).

2.1 MINERAL GROUPS – CALCITE, ARAGONITE, AND DOLOMITE

The carbonates precipitation products are summarized in three isochemical compounds: Calcite ($CaCO_3$), Aragonite ($CaCO_3$), and Dolomite ($CaMg(CO_3)_2$), where the main difference concerns the crystallographic arrangement (Flügel, 2010; Klein and Dutrow, 2012; Nichols, 2009).

(1) *Calcite Group* - consists of a group of five isomorphous members crystalized at the trigonal system, including calcite ($CaCO_3$), magnesite ($MgCO_3$), siderite ($FeCO_3$), rhodochrosite ($MnCO_3$), smithsonite ($ZnCO_3$). Calcite is the most common and familiar carbonate mineral, where magnesium ions can substitute calcium in the calcite crystal structure, forming low-Mg calcite (<4% - Mg) and high-Mg calcite (>4% - Mg - <19%). The minerals from the calcite group are similar in physical properties and can partially replace one another, forming solid solution series. The rhombohedral crystal is the most common mineral habit in

the calcite group. However, they also can present scalenohedral, tabular, acicular, fibrous, prismatic, flaky, and needle habits; (Flügel, 2010; Klein and Dutrow, 2012; Nichols, 2009).

(2) *Aragonite Group* - represents a group of four members at the orthorhombic system, including aragonite ($CaCO_3$), witherite ($BaCO_3$), strontianite ($SrCO_3$), cerussite ($PbCO_3$). Calcite and aragonite are polymorphous with the same chemical composition but different crystal structures. Aragonite has a high density of 2.95 compared to calcite (range of 2.72 - 2.94), which invertebrates have preferably synthesized; (Flügel, 2010; Klein and Dutrow, 2012; Nichols, 2009).

(3) *Dolomite Group* - the calcium magnesium carbonate group (> 20% - Mg) includes dolomite [$CaMg(CO_3)_2$], ankerite [$Ca(Fe^{2+}, Mg/Mn^{2+})(CO_3)_2$], and kutnohorite [$CaMn^{2+}(CO_3)_2$], they form a group of isomorphous carbonates at the hexagonal system. With crystal structures similar to calcite, the difference is the alternations along the crystallographic axis, between layer compound by Ca with layer compound by Mg. The Ankerite member can form two mineral series with dolomite (Mg-rich member) and kutnohorite (Mn-rich member). (Flügel, 2010; Klein and Dutrow, 2012; Nichols, 2009).

2.2 CHEMICAL CARBONATES

Carbonates precipitated by chemical processes occur in saturated environments depending on: (1) solution chemistry composition, with cations and anions availability (Ca^{2+}, Mg^{2+}, Na^{1+}, SiO_2, CO_3^{2-}, SO_4^{2+}, Cl^{1-}); (2) alkaline hydrogen ionic potential (pH), commonly related to CO_2 input or withdrawal. Common examples of chemical carbonates include travertines and tufas (Capezzuoli et al., 2014; Dupraz et al., 2009; Ford and Pedley, 1996).

Chemical carbonates are formed due to water saturation, related to a source rock dissolution, and subsequent precipitation by CO_2 concentration and pH changes. In places with a basement where carbonate rocks are abundant, the water circulation can cause their dissolution. This process is due to the low pH caused by the atmospheric water enrichment in CO_2 (Meteogenesis). In other words, surface water flows dissolving preterit carbonates rocks, becoming enriched and supersaturated in cations and anions (Capezzuoli et al., 2014; Dupraz et al., 2009; Ford and Pedley, 1996).

Eq.1 - $CaCO_{3(s)} + CO_{2(g)} + H_2O \leftrightarrow Ca^{2}{}_{(aq)} + 2HCO_3^-{}_{(aq)}$

As the solution travels across the surface, it loses CO_2 by degassing, which leads to a consequent increase in pH and carbonate precipitation. The CO_2 withdrawal is mostly due to

surface obstacles, such as changes in relief (Capezzuoli et al., 2014; Dupraz et al., 2009; Ford and Pedley, 1996).

Eq.2 - $Ca^{2+}_{(aq)} + 2HCO_3^-{}_{(aq)} \leftrightarrow CaCO_{3(s)} \downarrow + CO_{2(g)} \uparrow + H_2O$

2.2.1 Travertines

Usually, the term travertine defines carbonates precipitated by the influence of thermogenic processes commonly associated with hot springs, volcanism, deep faults, or tectonic. Upon reaching the surface, water under pressure in the subsurface undergoes a loss of CO_2 and, consequently, an increase in alkalinity. Despite the common presence of thermophile organisms, these case does not represent biochemical process (biomineralization or organomineralization). Instead, the process prevailing in the travertine system is chemical precipitation due to saturation and changes in pH and pCO_2. (Capezzuoli et al., 2014; Ford and Pedley, 1996). Examples of recent travertines from Japan (Fig. 1) and Argentine (Fig. 2):

Figure 1: Japan travertines; A. Pool formed in hydrothermal spring Futamata station, Hokkaido; B. Travertine with shrub-like structure, Kyushu Island; C. Highlight for crystal-ray shrub habit under petrographic microscopy (Mattos, 2016).

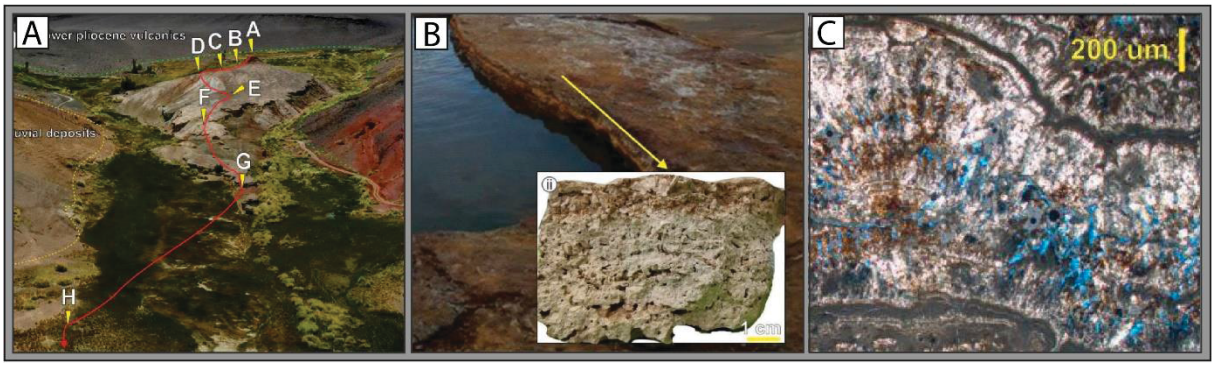

Figure 2: Travertine systems in Botijuela, South Puna – Argentina; A. Field view of travertine system; B. Travertine hand sample; C. Highlight for crystal-ray shrub under petrographic microscopy. (Alonso, 2022).

2.2.2 Tufas

Tufa defines carbonates precipitated under superficial conditions through meteoric water circulation without thermogenic process influence. Tufas occurs in surface environments, then a wide variety of organisms can be associated. In this way, the photosynthesis promoted by macrophytes and algae organisms often causes differences in the framework's structural aspects, as examples of tufa systems from Midwest Brazil (Fig. 3). However, these case does not represent biochemical process predominance (biomineralization or organomineralization). Instead, the process prevailing in this system is chemical precipitation due to saturation and changes in pH and pCO_2. (Capezzuoli et al., 2014; Oliveira et al., 2017; Oste et al., 2021)..

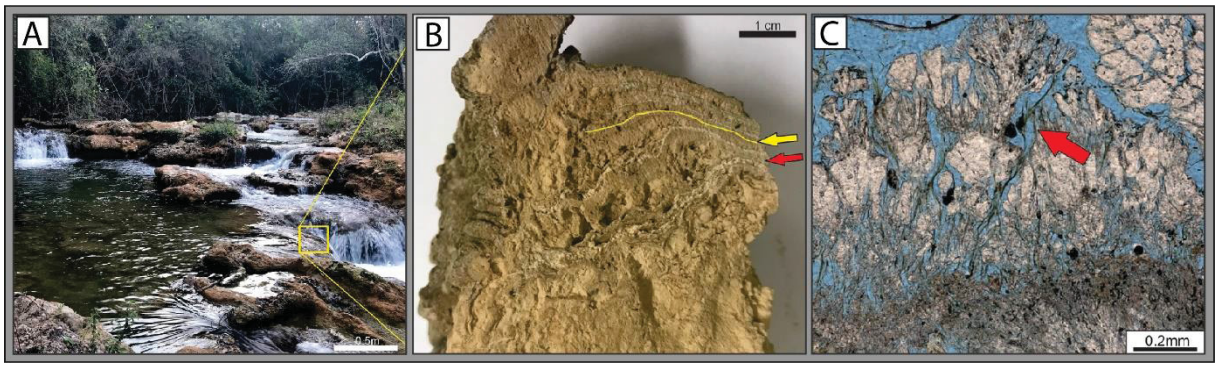

Figure 3: Tufa system, Bonito city, Midwest Brazil; A. Tufa forming pools and cascades; B. Tufa hand sample with the laminated framework; C. Highlight for the shrub-like structure under petrographic microscopy; (Oste et al., 2021).

2.3 BIOCHEMICAL CARBONATES

Biochemical carbonates have their genesis related to biological processes when DNA/RNA controls mineralization (Biomineralization) or organisms act as catalyzers for precipitation (Organomineralization).

2.3.1 Biomineral

Biomineralization processes are intrinsically related to biological processes when genetic control (DNA/RNA) directly drives the formation of carbonate minerals, also named Skeletal components, as examples coral reefs, ostracods, bivalves, and gastropod shells. However, despite the need for direct genetic control, environmental conditions may favor or inhibit the proliferation of organisms responsible for forming these skeletal components (Défarge et al., 2009; Dupraz et al., 2009; Perry et al., 2007). Examples of biomineralization from Bonito City in Midwest Brazil consist of Gastropods, bivalve shells, and Chara algae gyrogonites collected from Quaternary mudstones to packstone carbonates (Fig. 4).

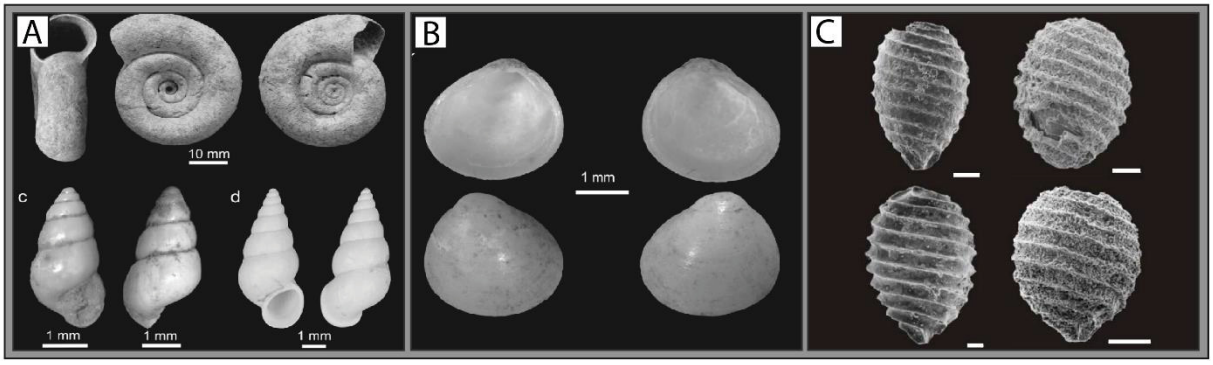

Figure 4: Biomineralization examples, carbonates biominerals from Bonito City, Midwest Brazil; A. *Gastropods*; B. *Bivalves*; C. *Chara* Algae Gyrogonites; (Utida, 2009; Utida et al., 2017).

2.3.2 Organomineral

Organomineralization is a terminology used when organisms participate in carbonate precipitation, subdivided into biologically *induced* or *influenced*:

(1) where *induced organomineralization* means an active process related to specific organisms that generate an organic matrix for precipitation (EPS- Extracellular polymeric substance), for example, stromatolites building organisms. Ex: Stromatolites from Rio de Janeiro, Brazil (Fig. 5).

(2) While *influenced organomineralization* means a passive process related to photosynthesis in favorable environments (ions availability, pH, and T), wherever an organism can realize the photosynthesis will lead to changes in these environments' chemistry conditions due to CO_2 uptake, leading to an increase in alkalinity and consequent precipitation (Decho et al., 2005; Dupraz et al., 2009; Riding and Awramik, 2000).

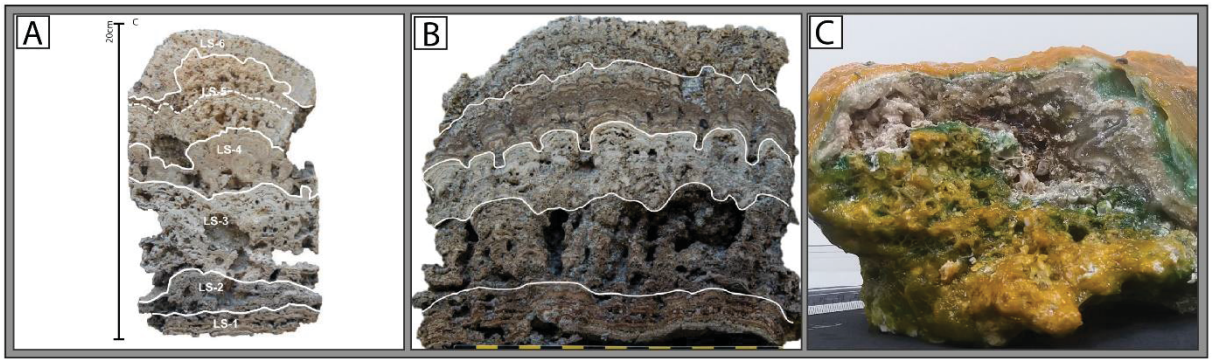

Figure 5: *Induced Organomineralization* examples, stromatolites from Rio de Janeiro - Brazil; A. Lagoa Salgada lithified stromatolite. (Bahniuk, 2013); B. Lagoa Salgada lithified stromatolite. (Dorneles, 2018); C. Lagoa Vermelha recent stromatolite (live biofilm), base associated with *Barnacle* shells (biomineralization), sample hosted at iLamir.

2.4 DESCRIPTION AND CLASSIFICATION

The classification of carbonate rocks was first proposed by Dunham (1962) to provide a description system regarding the main textural aspects intrinsic to the depositional environment. His proposal turned into the most widely used classification scheme. The three main criteria to define these classes were: (1) determine the original sediment fabric supporting, as matrix or clast supported; (2) the texture related to the proportion of mud in the framework (grains under <20 μm); (3) evidence of sediment organically-bound during deposition.

Late Embry & Klovan (1971) suggest a modification including three new classes for organically-bound (Bafflestone, Bindstone, Framestone) and two for coarse-grained carbonates (Floatstone and Rudstone) (Fig. 6). The second part of the description concerns the framework's main compound, turning possible naming a rock type with textural and compositional criteria components (Dunham, 1962; Embry and Klovan, 1971; Nichols, 2009).

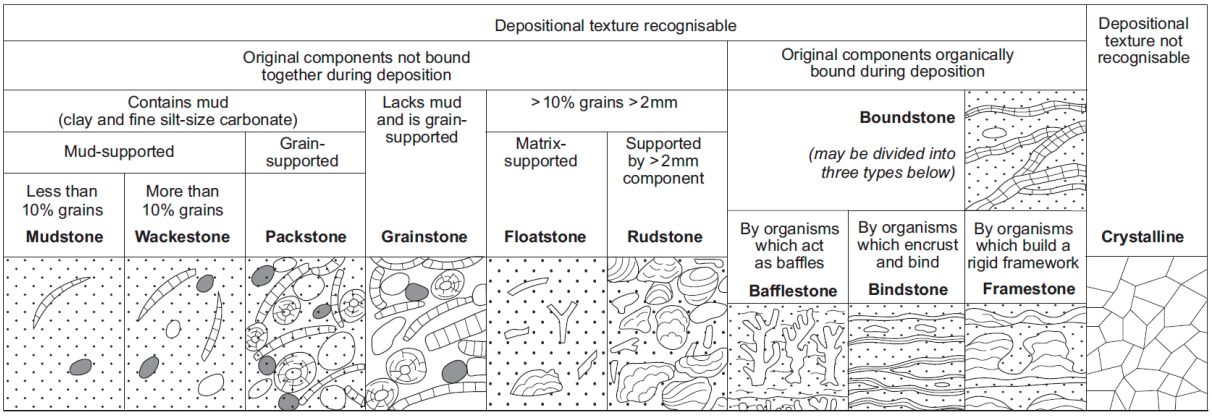

Figure 6: Carbonates classification following Dunham (1962) modified by Embry e Klovan (1971). (Nichols, 2009).

Choquette and Pray (1970) define porosity classification into fifteen pore types according to shape, genesis, fabric relationship, and pore size (Fig. 7).

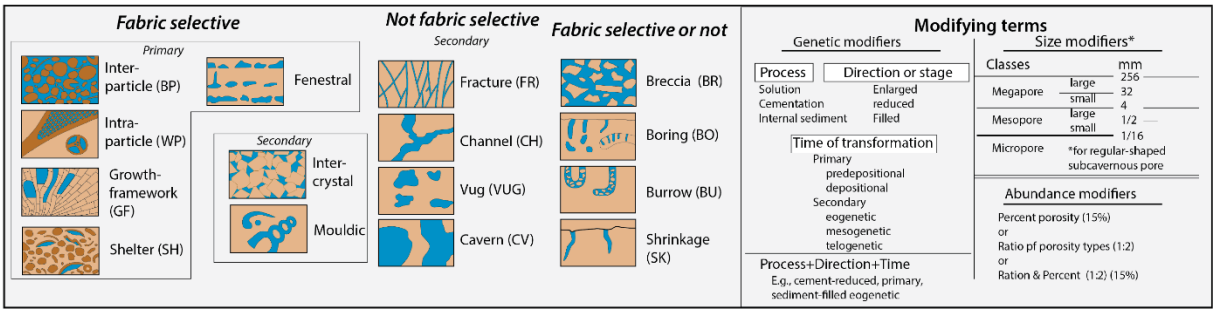

Figure 7: Porosity classification (Choquette and Pray, 1970).

The classification of dolomite *Fabrics* (Fig. 8) followed Friedman's basic terminology of crystallization textures (1965). It adapted to a descriptive classification guide by Randazzo

and Zachos (1983), combined with basic texture types defined by Sibley and Greg (1987), later compiled by Flugel (2010) (Flügel, 2010; Randazzo and Zachos, 1984; Sibley and Gregg, 1987).

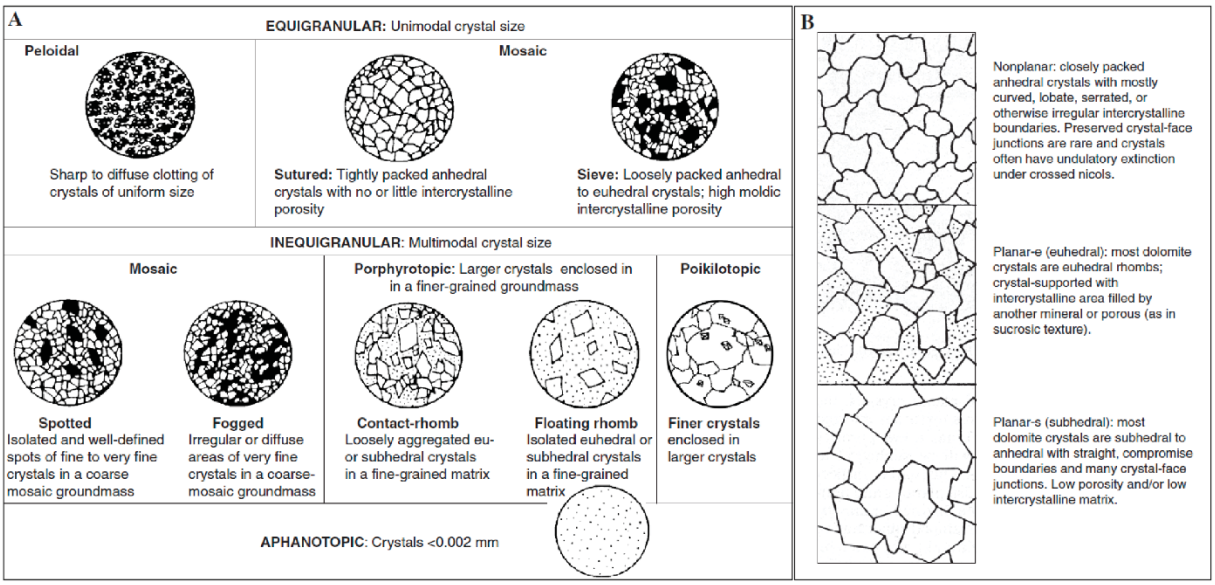

Figure 8: Classification of dolomite Fabrics compiled by (Flügel, 2010). A. Terminology of crystallization textures (Randazzo and Zachos, 1984); B. Textural type according to crystal shape (Sibley and Gregg, 1987).

Diagenetic textures description and classification (Fig. 9) follow Flügel's compilation, including mechanical compaction description, chemical compaction with pressure solution description, and classification guides (Choquette and James, 1987; Flügel, 2010).

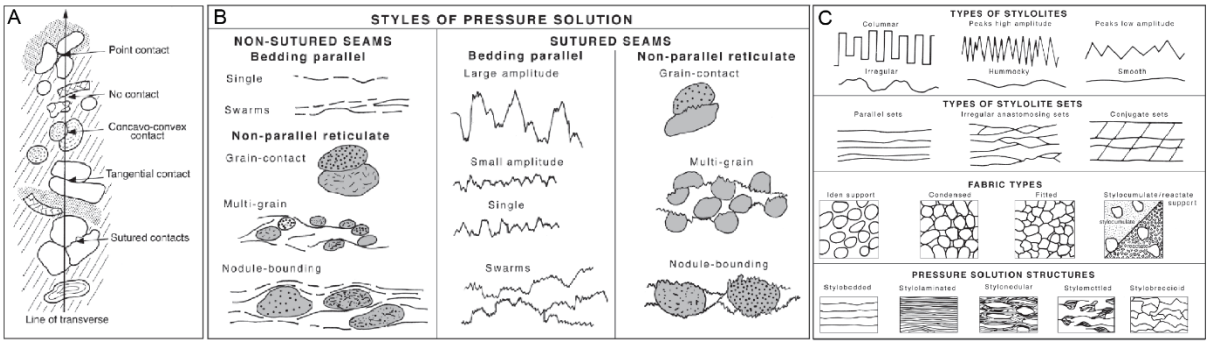

Figure 9: Diagenetic textures description and classification (Choquette and James, 1987; Flügel, 2010). A. Mechanical compaction description; B. Description of pressure solution features; C. Classification of pressure solution;

3 SILICATES (SiO_2): CLASSIFICATIONS AND GEOLOGICAL IMPLICATIONS

Minerals of the silicate class are among the most important rock-formers, making up approximately 90% of the Earth's crust. The fundamental structure of the silicates consists of a silicon atom (Si^{+4}) surrounded by four oxygen atoms (O^{-2}), forming a tetrahedron with a 50% ionic and 50% covalent bound that guarantees this compound the polymerization ability. The sharing of oxygen (O^{-2}) between silicon (Si^{+4}) makes possible the diversity of structural configurations into seven structural arrangements that form the basis of most rock-forming minerals (Dana and Ford, 1960; Klein and Dutrow, 2012; Wenk and Bulakh, 2004).

3.1 SILICA (SiO_2) POLYMORPHS - TECTOSILICATES

Minerals from the tectosilicate class make up approximately 64% of crustal rocks in three main polymorphs Quartz, Tridymite, and Cristobalite (Fig. 10A), according to earth's natural temperature and pressure conditions (Fig. 10B), with addition to stishovite and coesite as high-pressure polymorphs found in meteor impact craters (Berry, 1981; Götze, 2009; Wenk and Bulakh, 2004).

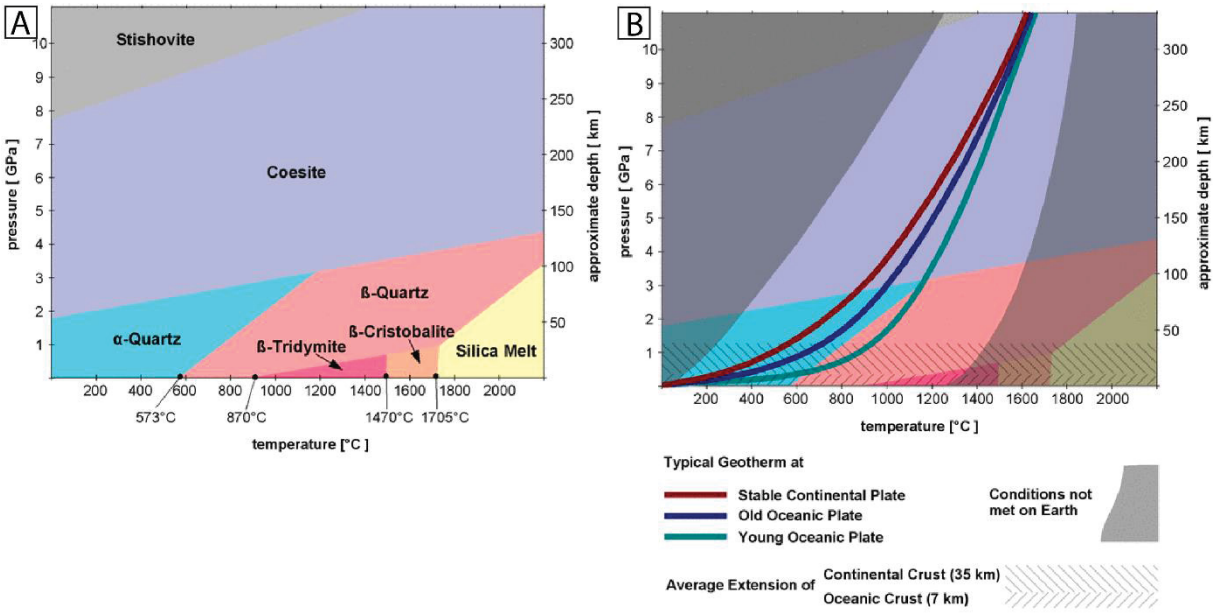

Figure 10: A. Silica (SiO_2) polymorphs according to temperature and pressure; B. Silica (SiO_2) polymorphs under earth p/T natural conditions and geotherm for continental and oceanic plates (Wenk and Bulakh, 2004).

However, considering each polymorph's low and high-temperature variation, eight geometric arrangement shapes are possible, as summarized in Table 1 (Berry, 1981; Götze, 2009; Klein and Dutrow, 2012). Since this research focuses on Quartz-α (Low-temperature quartz), the next topic describes their occurrence and textural variations.

Table 1: Silica (SiO_2) polymorphs.

Mineral name	Symmetrical system	Relative density	Refractive index	Si-O-Si angle	Stability temperature (Low pressure)
Stishovite	Tetragonal	4.35	1.81	-	High pressure
Coesite	Monoclinic	3.01	1.59	-	High pressure
α Quartz	Trigonal	2.65	1.55	144º	< 573 ºC
β Quartz	Hexagonal	2.53	1.54	153º	573 – 870 ºC
α Tridimite	Monoclinic/Orthorhombic	2.26	1.47	140º	< 117 ºC
β Tridimite	Hexagonal	2.22	1.47	180º	117 – 870 | 870 – 1470 ºC
α Cristobalite	Tetragonal	2.32	1.48	147º	< 270 ºC
β Cristobalite	Isometric/Cubic	2.20	1.48	151º	270 – 1470 | >1470 ºC

3.2 α-QUARTZ TEXTURAL VARIETIES

The components most commonly found in earth's surface environments are low-temperature silica polymorphs in special α-Quartz, composing igneous, sedimentary, and metamorphic rocks, as the most stable mineral under surface conditions. In contrast, β varieties have the expected occurrence associated with fast-rising magmatism. Normally α-Quartz appears with different petrographic textural aspects, macrocrystalline silica, popularly recognized as drusiform quartz or mega-quartz, and two types of microcrystalline silica, the granular recognized as chert and the fibrous type named chalcedony. In addition to α-Cristobalite/Tridymite in opal-CT form and rarely amorphous silica. Considering the growth process where macrocrystalline quartz is formed from molecules addition layer by layer. In contrast, microcrystalline quartz formed due to colloidal solutions precipitation (silica gel). This overview will focus on the descriptions following the crystalline form classification (Berry, 1981; Götze, 2009; Schmidt et al., 2013).

3.2.1 Granular Crypto/Microcrystalline Silica – Chert

The Chert terminology nominates granular microcrystalline silica, usually measuring > 4 μm for cryptocrystalline, and around 4-32 μm for microcrystalline, forming a porous, spongy texture. Chert origins are typically related to dissolution-reprecipitation processes in various geological environments. Silica solubility and precipitation can be a function of pH changes, with solubility increasing above pH 9, causing dissolutions in silica from previous rocks/minerals. Consequently, silica gel precipitation occurs with a minor alkalinity reduction from pH>9 (Trewin and Fayers, 2004). When related to hydrothermal systems, the water

circulation through convective currents can be responsible for the dissolution of depth rocks. Since the silicate solubility also increases with temperature, the silica-saturated water will consequently face silica precipitation with the water cooling (Schmidt et al., 2013).

Reported cases from sedimentary basins suggesting low-temperature phases changes of Amorphous silica (Opal-A) from biogenic sources (radiolarian, diatoms, sponge spicules) to α-Quartz, through disordered transformations, following the Sequence: Opal-A (Amorphous SiO_2) → Opal-CT [α-Cristobalite/tridymite (SiO_2*nH_2O)] → Chalcedony (Fibrous Microcrystalline - SiO_2) → α-Quartz (Macrocrystalline - SiO_2) (Heaney, 1993; Heaney et al., 1994).

A textural sequence is curiously observed and found in many situations related to chert occurrence, consisting of granular microcrystalline silica (Chert) overlayed by layers of fibrous microcrystalline silica (Chalcedony), with the remaining porosity filled by macrocrystalline silica (Drusiform quartz). However, the mechanisms related to this Sequence remains poorly understood (Trewin and Fayers, 2004).

3.2.2 Fibrous Crypto/Microcrystalline Silica - Chalcedony

Chalcedony occurs in various geological environments and is associated with the most varied types of rocks and minerals, from acid or basic igneous to metamorphic or sedimentary. Often found filling open spaces as cavities (Fig. 11), vesicles, dissolutions channels, vugular porosities, or fossil cavities (moldic porosity). Sometimes, it occurs as a cementing component of the sedimentary rock framework. It can also occur as a component of partial or total replacement of other minerals, forming pseudomorphs. (Navarro et al., 2017; Schmidt et al., 2013; Trewin and Fayers, 2004)

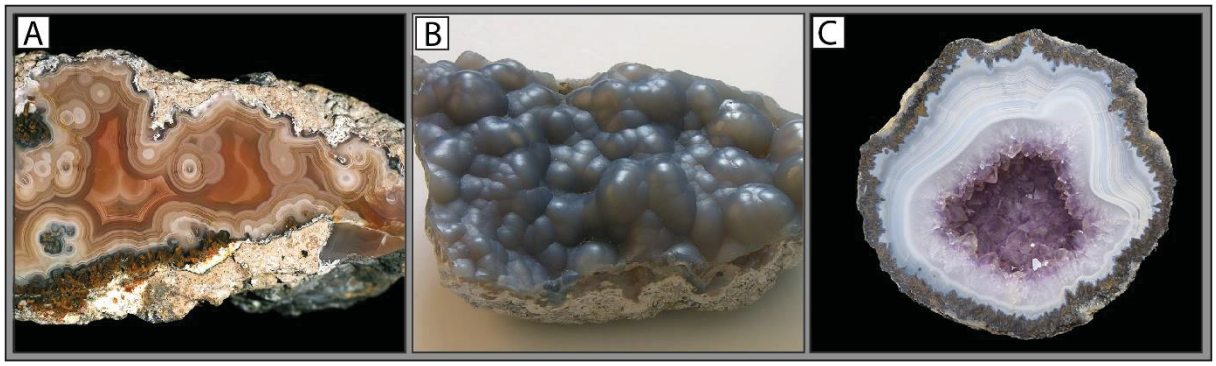

Figure 11: Examples of chalcedony filling rock cavities; A. Highlight for spheroidal habit (Ahumada City, Chihuahua – Mexico); B. Botryoidal/spheroidal habit (Trebisov City, Slovakia); C. Chalcedony filling a cavity, ending in mega-quartz (macrocrystalline | Drusiform quartz) variety amethyst (Ahumada City, Chihuahua – Mexico) (Ralph, 2023).

The term chalcedony defines quartz crystals with an aligned fibrous microcrystalline structure. The fibers commonly have tens to hundreds of micrometers in length. Their radial growth can naturally form bands, spherulites, botryoids (Fig. 12), or stalactite-like habits. Chalcedony is considered a secondary mineral deposited from watery colloidal solutions at low temperatures (<100ºC) as a product of weathering and meteoric water circulation or a product of low-temperature hydrothermal fluids. (Heaney, 1993).

Chalcedony occurs in two types according to the fiber orientation along the c-axis, based on polarized light behavior: (1) *Length-Fast chalcedony* – the crystallites grow perpendicular to the c-axis, with fibers twisted along the elongation axis, resulting in fibers along [1120] or [1010]; (2) *Length-Slow chalcedony* (*Quartzine and Letucite)* –The *Quartzine* variety with crystallites parallel to the c-axis, resulting in fibers along [0001], similar to macrocrystalline quartz. Intergrow or alternation between chalcedony and quartzine can occur. While *Letucite* consists of an intermediate type among LF chalcedony and LS quartzine, with the fibers elongated around 30º degrees with the c-axis. (Heaney, 1993; Schmidt et al., 2013; Trewin and Fayers, 2004).

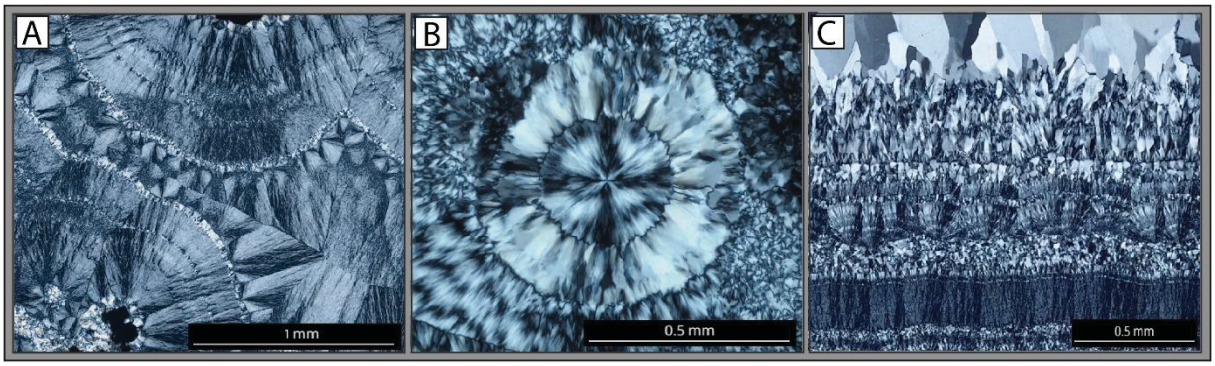

Figure 12: Chalcedony under cross-polarized petrography; A. Fibrous microcrystalline structure forming hemispheroids (Masullas, Oristano - Italy); B. Spheroidal *Length-Fast* Chalcedony (Kenifra region – Morocco); C. Layer alternation between silica with textural variations - Granular microcrystalline (chert), fibrous microcrystalline (chalcedony) forming hemispheroidal structure, ending with macrocrystalline silica (mega-quartz) (Palo Verde, California – USA) (Ralph, 2023).

3.2.3 Macrocrystalline Silica – Mega-quartz or Drusiform Quartz

Drusiform or Mega-quartz refers to euhedral crystals, with granulation ranging from millimeters to meters, usually forming prismatic crystals with horizontal striations and hexagonal basal sections. Quartz varieties usually receive trivial names due to color or habit variations. However, some of these names are not generally accepted depending on the author's preferences (Klein and Dutrow, 2012; Trewin and Fayers, 2004).

The occurrence of well-formed quartz crystals depends on the abundance of silica in the system. Since the silicates comprise the base structure for most other rock-forming minerals, their crystallization processes will remove silica from the system before allowing quartz crystallization. In this way, large quartz crystals with euhedral habits are incompatible with geological environments where high pressure and temperature prevail. These environments are preferable for all other silicate minerals formation (Rudnick and Gao, 2003; White and Klein, 2013).

Quartz is the most stable mineral near-surface conditions. However, at higher temperatures and pressures, their dissolution potential increases. This way, a watery solution circulating at depth through faults, fractures, or structural porosities, will be enrichened in silica from other rock-forming silicate minerals due to heating and pressure increase. This silica oversaturated-fluid circulation will ascend, leading to quartz crystallization through silica precipitation due to cooling. Another important source is residual silica-rich fluids from magma bodies' solidifications (Bons, 2001; Schmidt et al., 2013; Trewin and Fayers, 2004).

CHAPTER 2 – GEOLOGICAL SETTINGS

BRAZILIAN PRE-SALT

1 INTRODUCTION

Considering the importance of hydrocarbon reservoirs for society, an overview and compilation of previous geological data from Brazilian Pre-salt is presented in this chapter and includes: (1) A stratigraphic overview of Brazilian marginal basins, with a focus on Campos and Santos Basin; (2) A revision of the previously described lithologies for the Pre-salt section and recent analogous models; Focusing on a compilation of publications since the Brazilian Pre-salt public announcement (2009) and the beginning of the scientific research development in the field.

2 PETROLIFEROUS SYSTEMS

The hydrocarbon storage and generation in petroliferous systems through sedimentary basins involve three lithological requirements: (1) Source rock – means a lithology with deposition/precipitation direct or indirectly related to biological activities, and able to release an amount of organic matter after deposition, formed under marine or freshwater systems, most common examples are carbonates and shales; (2) Reservoir rock – consists in a rock where porosity and permeability properties allow migration and accumulation of fluids, as oil, gas or water. The most common examples of rocks with good porosity are high-maturity sandstones. However, recent studies show carbonates as a good source and reservoir rocks; (3) Seal rock – consists of a lithology with low permeability able to trap the fluids, as an example, evaporites (halite, anhydrite) or volcanic rocks (Rochelle-Bates, 2019). In addition, petroliferous systems also include processes related to organic matter maturation through temperature elevation until it turns into a hydrocarbon (oil/gas). However, this chapter will focus on the lithological requirements to present and describe the Brazilian Pre-salt reservoirs concerning the location and geological context.

3 REGIONAL GEOLOGY

The Pre-salt reservoirs are located on the Brazilian continental margin of the Central South Atlantic (Fig. 1) and inserted in the context of the Brazilian marginal sedimentary basins. In summary, the Brazilian Pre-salt is a stratum of sedimentary rocks composed of continental carbonates (source and reservoir) with an important hydrocarbon content, around 5000 meters

below sea level. These carbonates are sealed by the evaporites of the upper layers (Salt layer – seal), which gives rise to the Pre-salt name (Fig. 2).

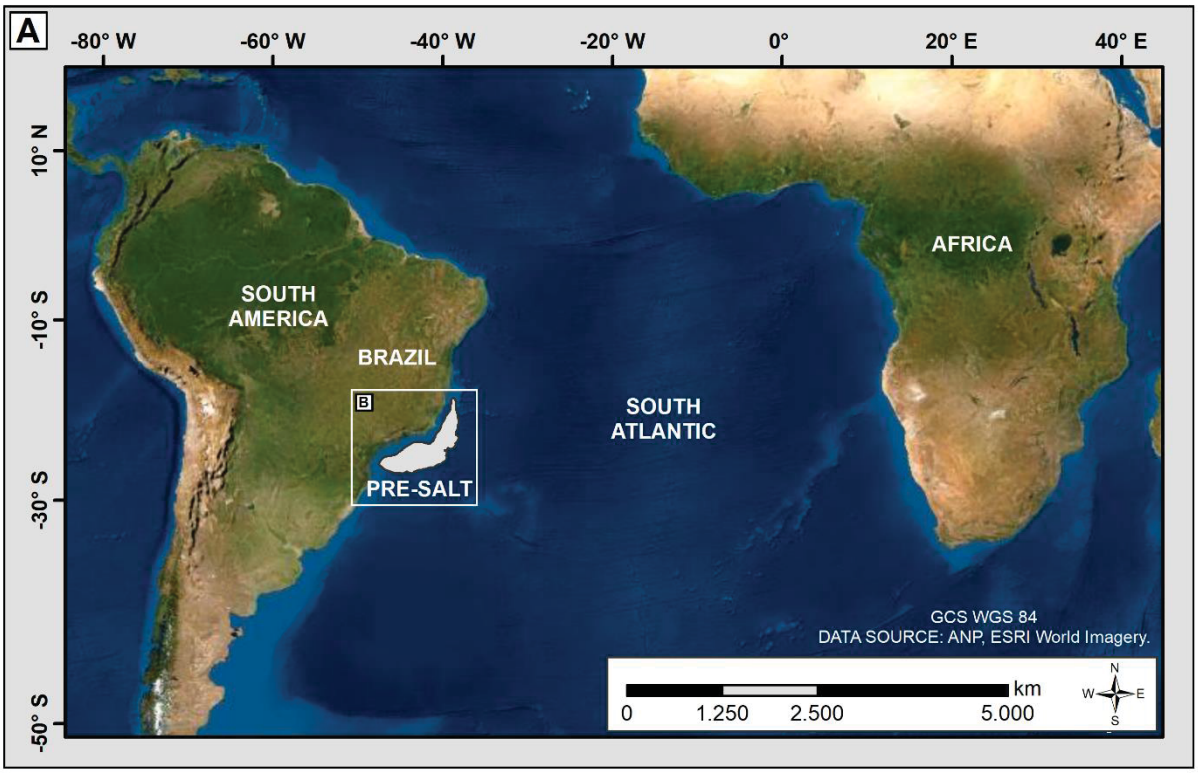

Figure 1: Location of the Brazilian Pre-salt reservoir on the continental margin of the Central South Atlantic.

Several studies have shown that Brazilian and African Pre-salt lithologies have similarities according to geological time and processes related to their genesis. Currently, the observed lithologies receive different names according to the region and sedimentary basin location. However, these Formation names are more related to local linguistics than geology. So then, we bring a review emphasizing the geological record, lithology, time, and environmental process considering the Central South Atlantic context instead focus on local Formation. Therefore, they can be grouped as the Geological record of the Central South Atlantic compartmentation.

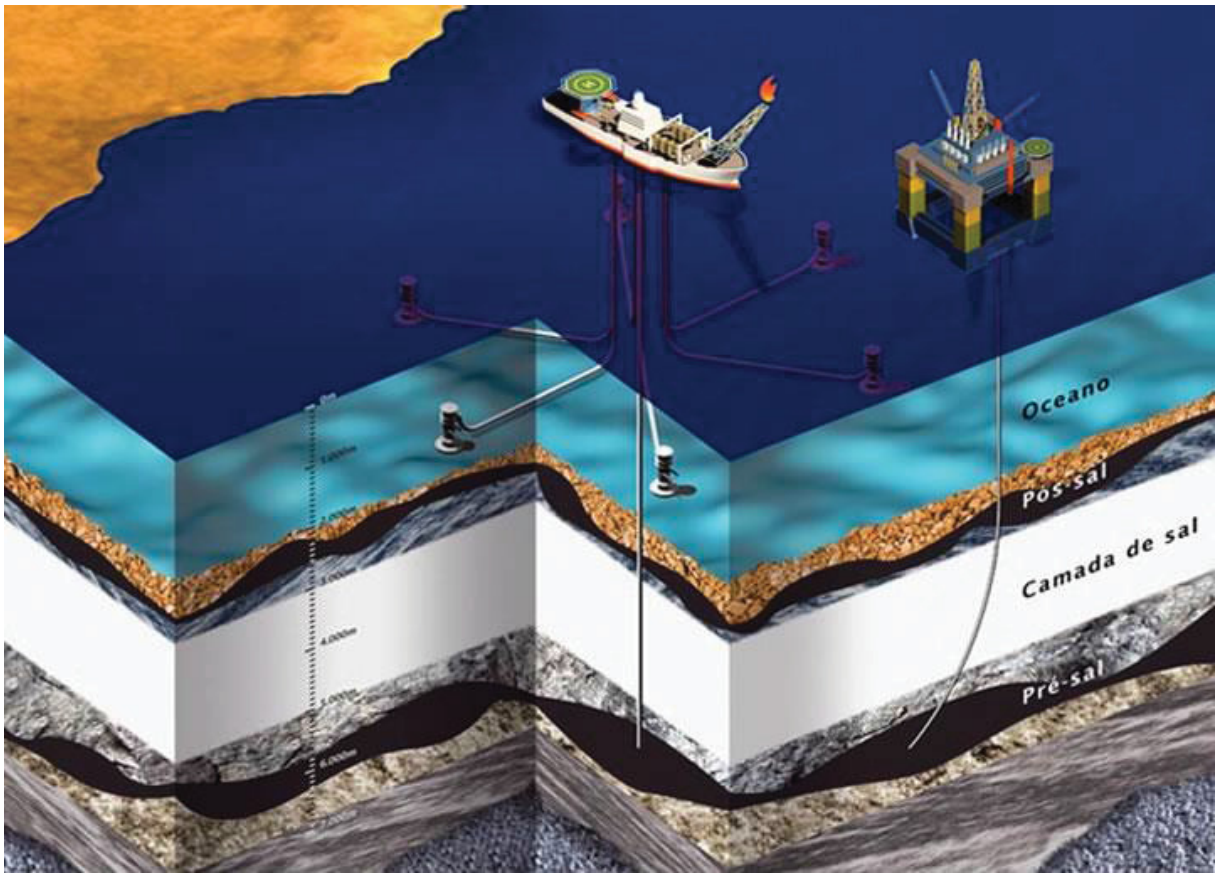

Figure 2: Brazilian Pre-salt reservoirs representative model. Carbonates with hydrocarbon content are located around 5000m to 7000m below the sea level, covered by evaporite (salt) layers (Gouveia, 2010).

3.1 GONDWANA CONTINENT BREAK UP – MARGINAL BASINS ORIGIN

The stratigraphic compartmentation in the Brazilian (Campos and Santos) and African (Angola, Congo, Kwanza) marginal basins evidences their genesis in an extensional paleogeographic context, which represents the Gondwana continent breakup during the Late Jurassic until the Early Cretaceous. This extension process precedes the South Atlantic Ocean genesis while separating African and South American plates (Castro and Picolini, 2015; Guardado et al., 2000).

The Central South Atlantic Marginal Basins represent three tectonosedimentary units of extensional context: (1) Rift Sequence; (2) Transitional Sequence; and (3) Final Drift or Passive Margin Sequence (Castro and Picolini, 2015; Guardado et al., 2000; Thomaz Filho and Milani, 2018) with a similar lithostratigraphy sequence observed on the African side of Kwanza, Congo, and Namibian Basins (Rochelle-Bates, 2019; Teboul et al., 2019).

3.2 RIFT SEQUENCE

The geological record of the Central South Atlantic Marginal Basins starts with the Rift Sequence, around 135 to 118 Ma (Valanginian to Aptian) (Fig. 3A). This stage represents an increased lithospheric extension with an asthenosphere elevation forming the Paraná-Etendeka province. Tholeiitic volcanism and continental sedimentation fill elongated deep lakes during the rifting phase (Fig. 3B) (Cainelli and Mohriak, 1999; Mohriak et al., 2012; Thomaz Filho and Milani, 2018).

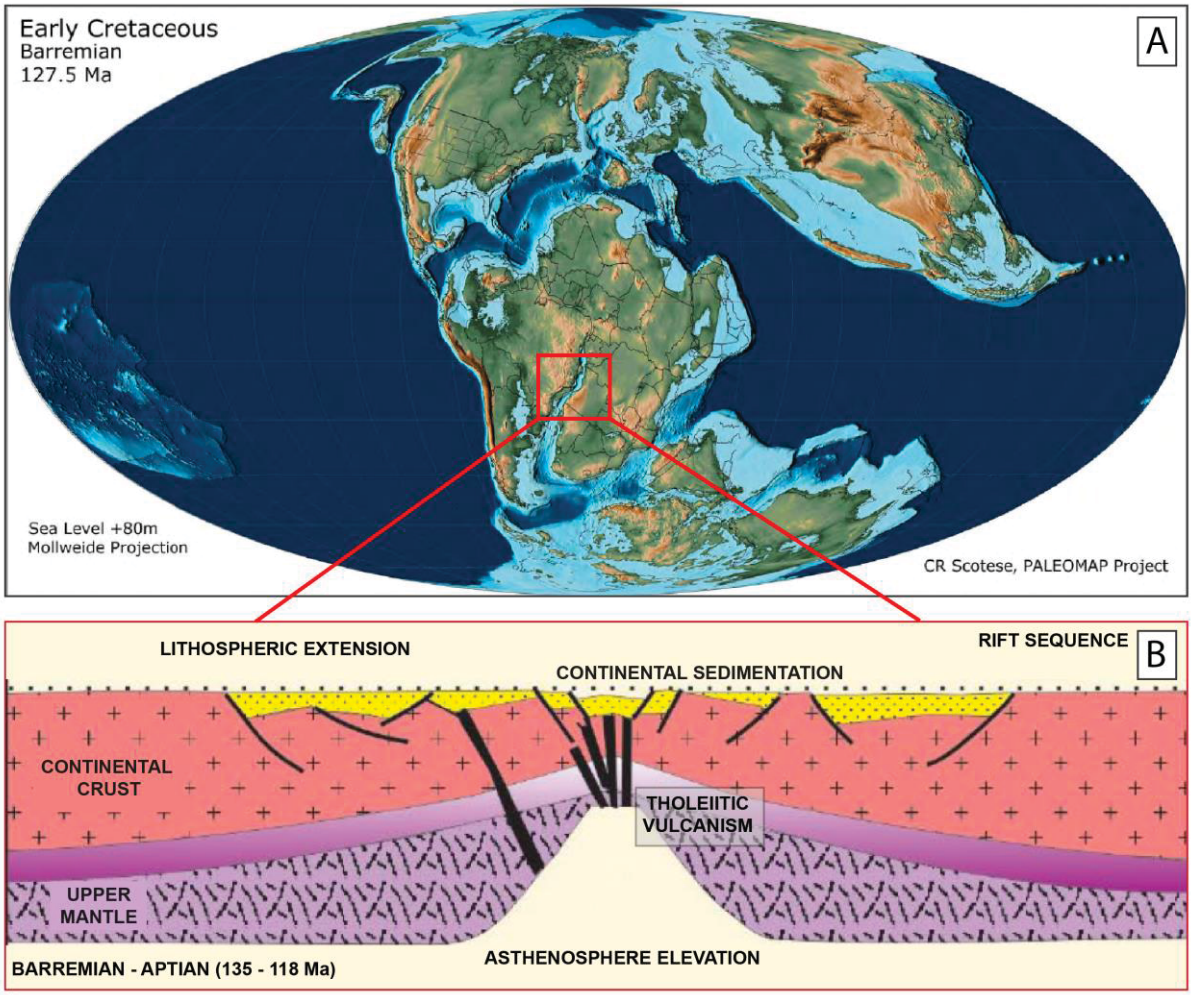

Figure 3: Rift Sequence, 135 to 118 Ma (Early Cretaceous - Valanginian to Aptian). A. Paleogeographic map of Barremian (Early Cretaceous 127.5Ma). (Scotese, 2014); B. Rift evolution model, illustrating lithospheric extension and asthenosphere elevation during the rift stage, with consequent tholeiitic volcanism and continental sedimentation. (Cainelli and Mohriak, 1999).

In this context, the Walvis ridge volcanic high, associated with the Tristan da Cunha hotspot, is an important feature in the Pre-salt geological record. Since the topographic high stopped marine seaways, allowing fluvial-lacustrine conditions (Rochelle-Bates, 2019).

After the tholeiitic volcanism, still during the Rift development, the crustal stretching and the subsidence led to elongated lakes filled by continental sedimentation. These records are mostly fluvial and lacustrine deposits with delta fans composed of siliciclastic sedimentation, including conglomerates, sandstones, siltstones, and shale (Herlinger et al., 2017; Lima et al., 2019; Mohriak et al., 2012)

The Upper Rift phase is marked by bivalve bioclast (Coquinas) and oncolytic deposits, classified as rudstones and grainstones related to playa-lake and pluvial lake deposits (Antunes, 2021). The Pre-Alagoas regional unconformity bounds the Rift Sequence, which onsets uplift and rift-shoulder erosion (Castro and Picolini, 2015; Herlinger et al., 2017; Mohriak et al., 2012).

3.2.1 Upper Rift - Bioclastic and oncolytic deposits (Reservoir)

Commonly termed *Coquinas*, the main framework component of this grainstone and rudstone are the bivalve (Fig. 4A), ostracods, or gastropod shells (Fig. 4B), forming massive deposits, showing variable degrees of reworking. These lithofacies contain small amounts of carbonate mud, such as peloids, ooid particles, and siliciclastic or volcanic fragments. The cementation consists of calcite, dolomite, or silica (Fig. 4C) but depends on the diagenetic processes involved. When dissolution prevails, the bioclasts' moldic porosity is preserved. Therefore, diagenetic assemblages, such as sulfides and sulfates, are rare for these lithofacies (Antunes, 2021; Herlinger et al., 2017; Lima et al., 2019; Teboul et al., 2019).

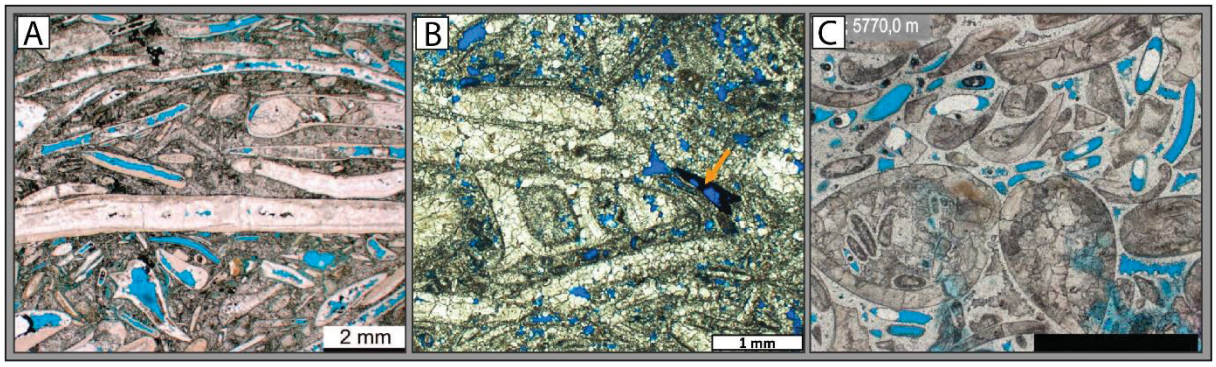

Figure 4: Coquinas from the Presalt Upper Rift Sequence. A. Poorly sorted bivalve rudstones with intraparticle porosity. (Herlinger et al., 2017); B. Bivalve-Gastropd rudstones with interparticle porosity partially filled by bitumen (Lima et al., 2019); C. Massive rudstones with matrix/cement recrystallization and silicification, showing well-preserved articulate bivalve shells (Antunes, 2021).

The coated grains, as the framework's main component, are restricted and described at the upper rift section in some wells (Barnett et al., 2018; Gomes et al., 2020; Herlinger et al., 2017; Lima et al., 2019). The carbonate-coated grains are mostly oncoids. They consist of

carbonate laminations forming concentric layers around bioclastic or lithoclastic nuclei by microbial activity, commonly cyanobacteria with genesis related to shallow water environments, including marine to freshwater. Indeed, there are some classifications concerning sizes. However, oncoids terminology is most accepted and largely used for these concentric grains related to microbial activities (Dahanayake, 1978; Flügel, 2010; Logan et al., 1964; Riding and Awramik, 2000).

The oncoidal grainstones and rudstones frequently show dissolutions features (Fig. 5A) and variable degrees of cementation (Fig. 5B) and fracturing. The cementation phases are usually composed of calcite, dolomite, and silica. Bivalves and gastropod shells appear as oncoids nuclei or compounds in a bimodal matrix (Fig. 5C) (Antunes, 2021; Barnett et al., 2018; Lima et al., 2019).

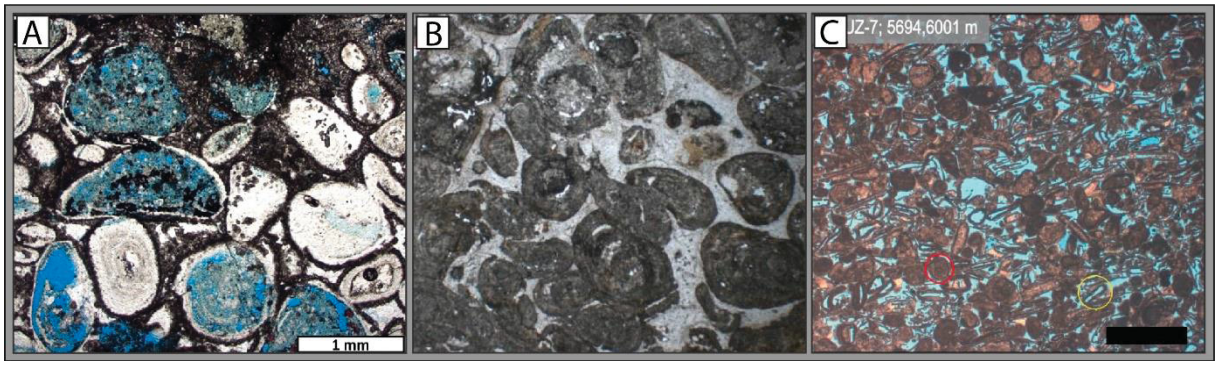

Figure 5: Carbonate-coated grains (oncoids) from Presalt *Upper Rift* Sequence. A. Oncoidal grainstone showing degrees of dissolution and silicification, initially described as stevensitic arenites. (Lima et al., 2019); B. Silicified oncoidal grainstone, also described as microbialite (Barnett et al., 2018); C. Oncoids and bivalve grainstone with interparticle and intraparticle porosities (Antunes, 2021).

3.2.2 Stevensitic Magnesian Clay

The most common syngenetic magnesian clay mineral is the stenvensite (smectite group) and usually occurs as a matrix compound on the bivalve and oncoidal rudstones/grainstones (*coquinas*). They are interpreted as precipitation in a high alkaline (pH ≥ 10) lacustrine environment, low pCO_2, elevated magnesium, and silica concentration (Wright and Tosca, 2016). The deposition of the laminated stevensite was probably in low-energy environments. And the dissolution features are probably an eodiagenetic process under a pH ≤ 8 and high pCO_2 conditions (Herlinger et al., 2017; Lima et al., 2019). The magnesian clay deposits are pale to dark brown (thin section, uncrossed polarized), occurring in peloids (variable sizes), ooids (2mm), intraclasts, and massive or laminated aggregates. Although dissolution and deformation evidence frequently appear, the original fabric appears scarcely

preserved due to the chemical stability of magnesian clay (Herlinger et al., 2017; Lima et al., 2020, 2019).

3.3 TRANSITIONAL SEQUENCE (SAG SECTION)

The Transitional Sequence involves continental to marine sedimentation, dating from 118 to 112 Ma (Fig. 6A). This sequence consists of carbonate deposits (Fig. 6B) described by basic high-frequency cycles, around 1-2m thickness, with regular facies repetition, mainly: (1) laminated mudstones (calcimudstones); (2) calcite spherulites; (3) fascicular calcite crusts (Shrub); (4) microbialites (stromatolite). In addition to the Upper Rift lithofacies, these carbonates consist of the denominated Pre-salt reservoirs (Barnett et al., 2018; Gomes et al., 2020; Herlinger et al., 2017; Lima et al., 2019; Muniz and Bosence, 2015).

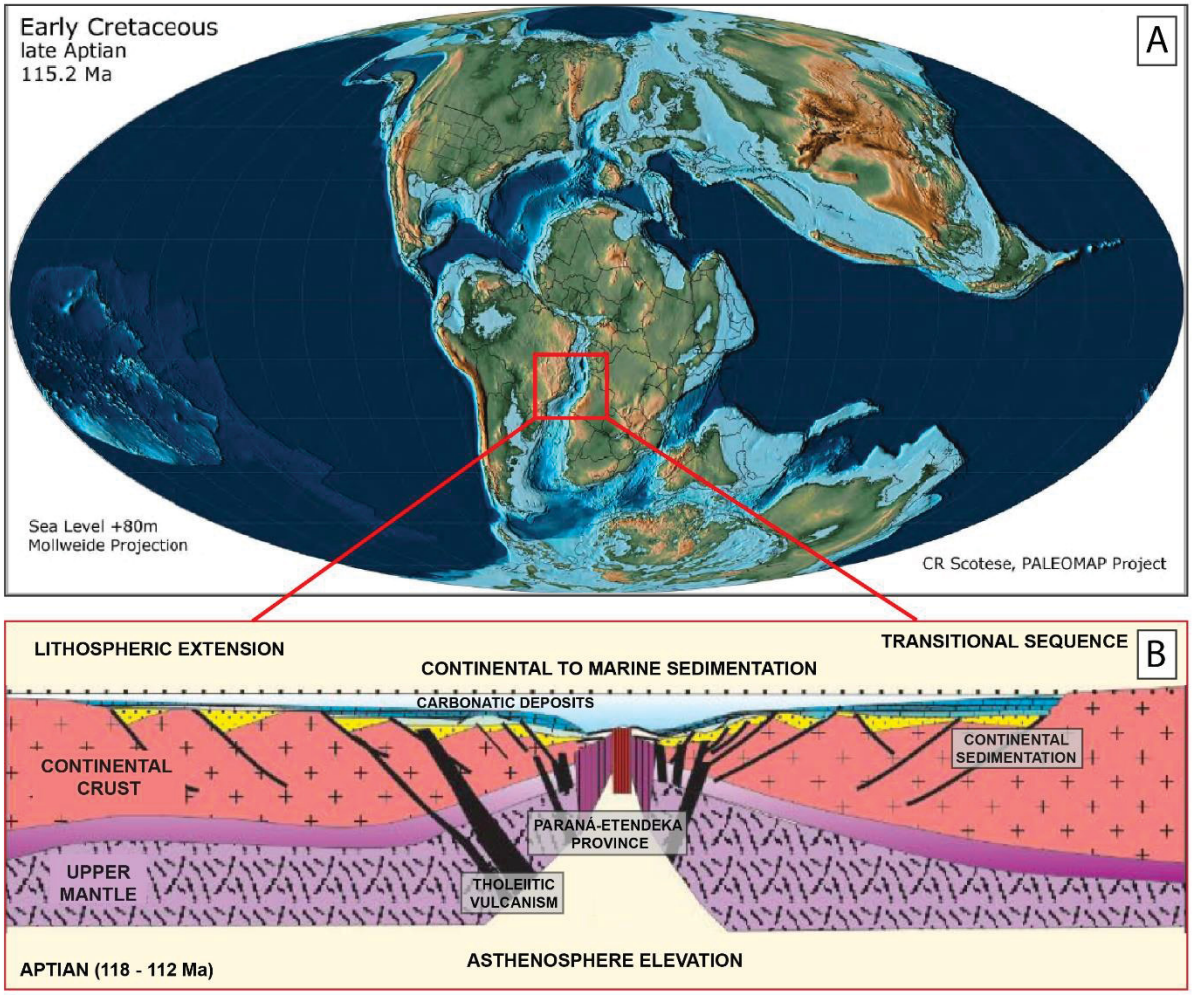

Figure 6: Transitional Sequence, 118 to 112 Ma (Early Cretaceous – Aptian). A. Paleogeographic map of Aptian (Early Cretaceous 115.2 Ma) (Scotese, 2014); B. Transitional sequence evolution model, illustrating lithospheric extension and asthenosphere elevation after the rift stage, with Paraná-Etendeka province development and continental to marine sedimentation (Cainelli and Mohriak, 1999).

The interval ends with evaporite accumulations and provides a seal for the Pre-Salt reservoirs. They are composed of anhydrite, halite, and bittern salts (sylvite and carnallite), formed under dry conditions due to restricted marine incursions from the southerly portion of the Atlantic Ocean. The Walvis Ridge subsidence probably allowed the marine incursions, leading to the evaporite formation (Gomes et al., 2020; Herlinger et al., 2017; Lima et al., 2019; Rochelle-Bates, 2019; Wright and Tosca, 2016).

3.3.1 Carbonatic deposits (Reservoir)

Carbonates are the main components of the Transitional Sequence (Local stage Alagoas), with deposition during the Aptian (Lower Cretaceous). Despite the need for further research and lack of consensus for lithofacies denominations, the carbonate material described and detailed in several studies shows a similarity in content. It can be summarized in four main features: (1) mudstones (calcimudstones); (2) spherulites; (3) fascicular calcite crusts (Shrub); (4) microbialites (stromatolite);

(1) Mudstones:

The carbonate mudstone framework frequently forms laminated deposits (Fig. 7A) and comprises fine-grained material, commonly composed of calcite (Fig. 7B) and sometimes magnesium-calcite (Fig. 7C). They have also been denominated calcimudstones or laminites. Some cases contain well-preserved vertebrate remains as fish fragments. The main interpretation concerning this lithofacies suggests a flooding (pluvial) event with a lake level increasing. This interpretation considers the alkalinity pH (9-10) favorable for carbonates with a pH limit > 10 considered lethal fish species (Barnett et al., 2018; Gomes et al., 2020; Lima et al., 2019).

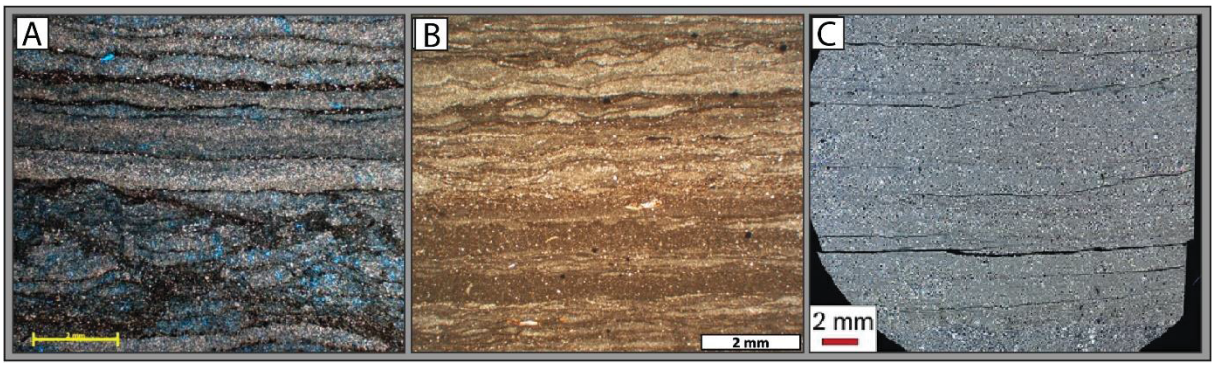

Figure 7: Mudstones from Presalt Transitional Sequence. A. Laminated calcimudstone (Barnett et al., 2018); B. Wavy laminated mudstone (Lima et al., 2019); C. Mg-Clay mudstone (Gomes et al., 2020).

(2) Spherulites:

Spherulite morphologies are a common structure formed by growth under non-equilibrium conditions due to rapid cooling. Commonly found in various natural and industrial compounds, including polymers (Crist and Schultz, 2016; Magill, 2001), metal oxides, silicate, or volcanic glasses (Lofgren, 1971). They also are formed in a range of carbonate systems, such as lacustrine or hypersaline (Mercedes-Martín et al., 2017, 2016).

There is no consensus regarding the Pre-salt spherulites (Fig. 8A). Recent studies suggest nucleation from magnesium stevensitic clays (Fig. 8B) and point to the possibility of spherulites as nucleation sites for the fascicular calcite growth (Fig. 8C) (Herlinger et al., 2017; Lima et al., 2019; Rochelle-Bates, 2019). However, these microfacies still require further studies and discussions.

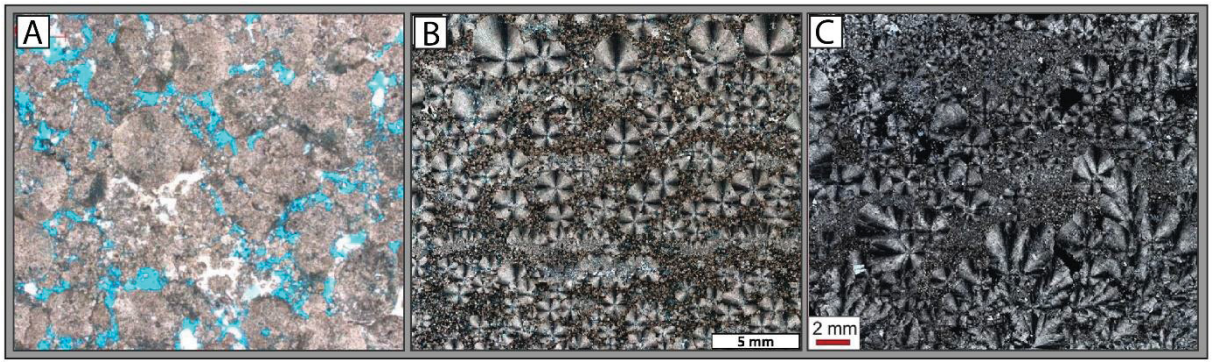

Figure 8: Spherulites from Presalt Transitional Sequence. A. Spherulitic grainstone/rudstones (Barnett et al., 2018); B. Calcite spherulites in Mg-Clay matrix (Lima et al., 2019); C. Calcite spherulites associated with fascicular calcite (shrubs) (Gomes et al., 2020).

(3) Fascicular calcite crusts | Shrubs:

The main facies that constitute the reservoirs of the pre-salt sag section are fascicular calcite crusts. These facies contain non-magnesian calcite in fascicular optic crystals aggregates (Fig. 9A), with vertical orientation and length around 1.5 to 12 mm, displaying a coalescent shrub shape forming calcite crusts (up to 80 cm thick) (Gomes et al., 2020; Herlinger et al., 2017; Lima et al., 2020, 2019).

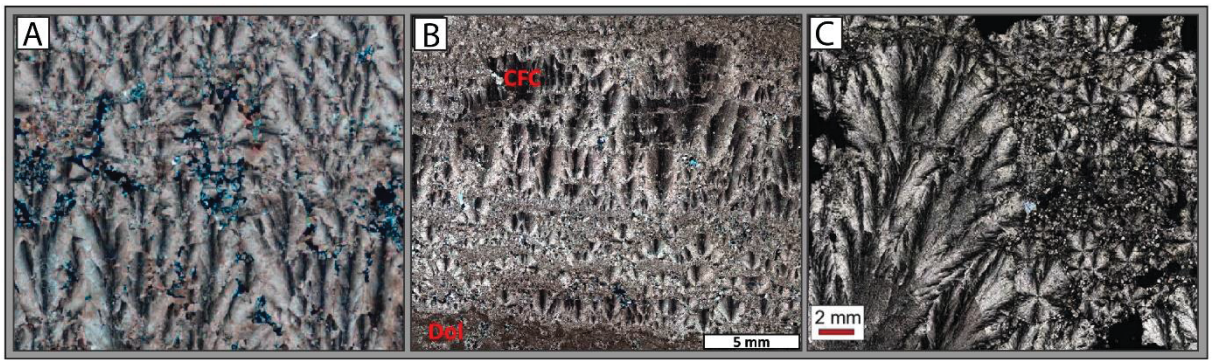

Figure 9: Fascicular calcite (shrubs) from Presalt Transitional Sequence. A. Calcite crystals aggregates with fascicular optical structure (Herlinger et al., 2017); B. Fascicular calcite crust intercalated with mudstones and spherulites, partially replaced by dolomite (Lima et al., 2019); C. Fascicular calcite associated with calcite spherulites (Gomes et al., 2020);

The fascicular calcite growth-framework and inter-crystalline aggregates are also responsible for the coalescent aggregates' primary porosity. This porosity often appears enlarged by the dissolution process. Furthermore, frequently cemented/replaced by dolomite (saddle, blocky or microcrystalline) (Fig. 9B) and silica (microcrystalline, chalcedony spherulites, prismatic, blocky, or mosaic fabric) (Herlinger et al., 2017; Lima et al., 2020, 2019) and interpreted as abiotic precipitation due to evaporation and CO_2 loss (Lima et al., 2019; Wright and Tosca, 2016). Their Formation is related to available space for vertical growth and ionic supply disponibility, frequently associated with the calcite spherulites nucleation (Fig. 9C), directly linked to the water-sediment interface (Herlinger et al., 2017; Lima et al., 2019). They grow thick and laterally, possibly associated with water chemistry changes due to a less arid period or CO_2 input by hydrothermal activity (Herlinger et al., 2017; Lima et al., 2019).

(4) Microbialites:

Microbialites are mentioned in the Presalt Transitional Sequence (Barnett et al., 2018; Muniz and Bosence, 2015; Saller et al., 2016). However, they lack detailed studies showing evidence of microbial influence|induction since just microbial presence does not imply their action on framework construction. For example, they lack studies with scanning electron microscopy (SEM) showing calcification of the Extracellular Polymeric Substances (EPS) Sheath Structures and other bacterial-related structures (Bahniuk, 2013; Dupraz et al., 2009; Riding and Awramik, 2000). Therefore, to understand carbonate related to microbial activities, only macroscopic and thin-section descriptions are insufficient because they can leave doubts

and lead to misunderstanding. The same consideration must be applied to interpreting the biotic or abiotic origins.

3.3.2 Dolomitization

Dolomite is a diagenetic component, commonly filling interstitial framework or vugular porosity (Fig. 10A). They appear in blocky (Fig. 10B), saddle (Fig. 10C), and microcrystalline habits, rarely observed in mosaic habits. Sometimes seems to replace primary and diagenetic mineral paragenesis. This dolomitization process varies from incipient to intense and can overlie or destroy the original mineralogical fabric. Furthermore, dolomite substituting stevensite sediments appears preferable to calcite spherulites. The absence of silica inclusion indicates a chronology with the dolomitization occurring before the silicification process in the pre-salt Sequence (Herlinger et al., 2017; Lima et al., 2020, 2019).

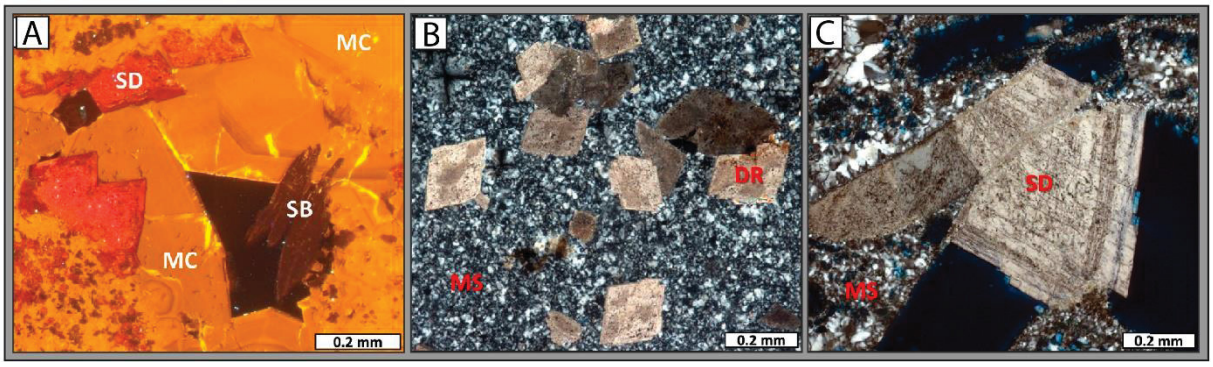

Figure 10: Dolomite from the Presalt section. A. Cathodoluminescence image of dolomite associated to macrocristaline calcite; B. Blocky dolomite associated to microcristaline silica; C. Saddle dolomite associated to microcristaline silica (Lima et al., 2019).

3.3.3 Silicification

Represents silicified samples (cherts), where the original fabric appears partially or totally replaced, and the secondary porosity (fracturing and vugular) is commonly filled by silica. The described features are chalcedony (Fig. 11A), silica spherulite aggregates, microcrystalline (Fig. 11B), macrocrystalline silica (Fig. 11C), and mosaic or prismatic quartz rims. Silicification is defined as after dolomitization since some silicified samples preserve dolomitized components (De Luca et al., 2017; Herlinger et al., 2017; Lima et al., 2020, 2019; Teboul et al., 2019).

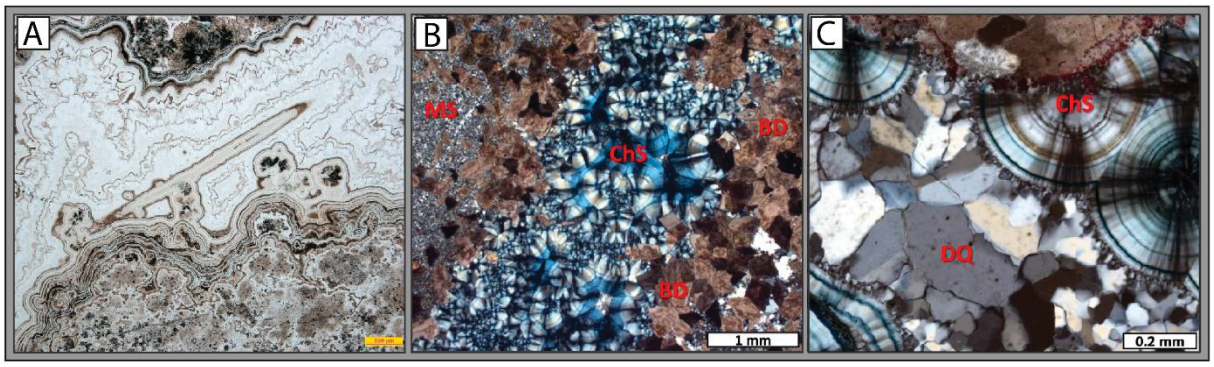

Figure 11: Silica cementation on Presalt lithofacies. A. Layers of chalcedony filling vugular porosity (De Luca et al., 2017); B. Microcrystalline silica associated with block dolomite and vugular porosity filled by silica spherulites; C. Chalcedony spherulites, and silica macrocrystalline (Drusiforme quartz) (Lima et al., 2019).

Moreover, in the pre-salt section, many features are related to fluid circulation, such as fracturing and dissolution, sulfides precipitation, dolomitization, and silicification of host rocks. Consequently, fluid inclusions and isotopic data are required to identify the environmental condition responsible for the genesis of the referred paragenesis (Herlinger et al., 2017; Lima et al., 2019). For example, fluid inclusion measurements in the Campos Basin calcite, quartz, and dolomite show homogenization temperatures between 92° to 152°C (Lima et al., 2020). In addition, fluids measurements at the analogous Kwanza basin show temperatures homogenization around 95° to 115° C (Poros et al., 2017). Thus, despite the variability of habits, dolomite and chert can be a product of common profound burial alteration or hydrothermal alteration (Herlinger et al., 2017).

3.4 FINAL DRIFT | PASSIVE MARGIN SEQUENCE

The Passive margin Sequence (Final Drift) evidences marine deposits from Albian until the Holocene (Fig. 12A). A transgressive deep marine context overlies the evaporites (Fig. 12B). This stage starts with proximal deposits, mostly platform carbonates in a shallow-marine context, followed by distal deposits with deep-water sedimentation (Castro & Picolini, 2014; Milani et al., 2017, Fernandez 2017, Gomez, 2020).

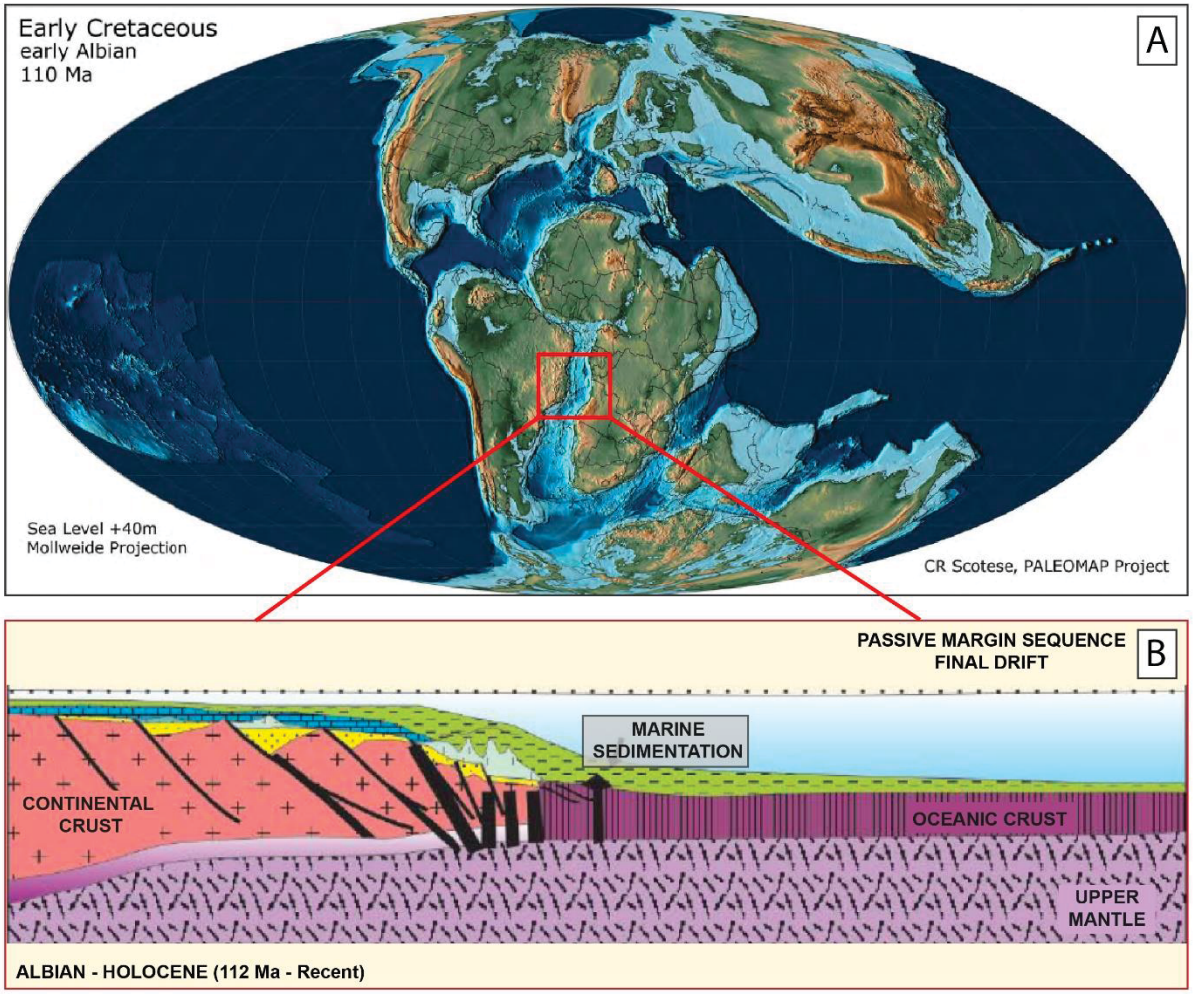

Figure 12: Passive Margin Sequence (Early Cretaceous, Albian – to Holocene). A. Paleogeographic map of Early Albian (110 Ma) (Scotese, 2014); B. The final Drift / Passive margin evolution model illustrates oceanic crust development and marine sedimentation after the transitional Sequence (Cainelli and Mohriak, 1999).

4 CRETACEOUS PERIOD

The name Cretaceous is related to the Greek word derivation Creta, in Latin means chalk, a term used to name carbonates, as initially proposed by Omalius d'Halloy (1822), due to the abundance of carbonates found during the first geological surveys in France. As most of the Pre-salt genesis history occurred during the Lower Cretaceous, it is important to understand the climatic and environmental conditions that prevailed during this period.

The climate on the earth's surface was much hotter than today (Fig. 13), also considered the hottest of the Phanerozoic, with subtropical climate conditions reaching up to the parallels at 45º. In this way, despite controversies and the need for further studies, the average temperature estimated from data compilation of carbonates, reefs, evaporites, coals, and bauxite deposits, ranges around 30ºC for the equator, 14º (winter) - 17ºC (summer) for the poles, and 17º for deep sea during Albian. Since no ice sheet was at the poles, the sea level reached about

200m to 250m above the current level, forming epicontinental seas (Huber et al., 2018; Scotese et al., 2021).

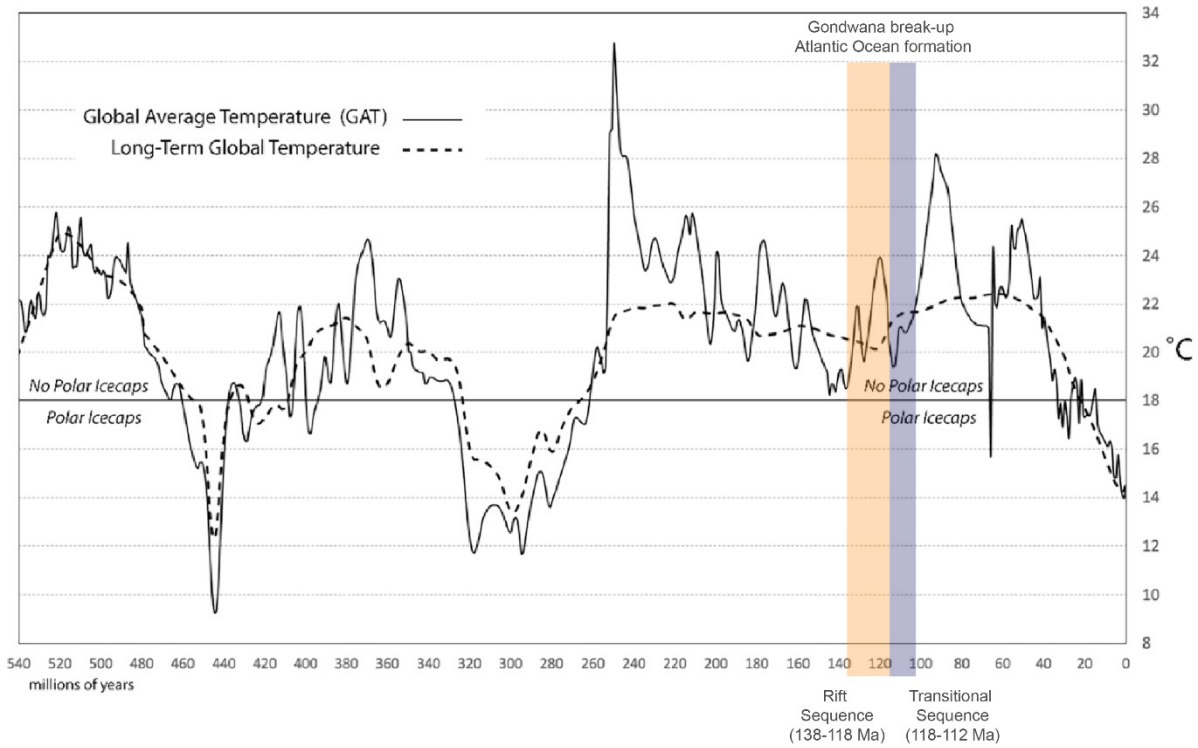

Figure 13: The estimated average temperature for Phanerozoic (Scotese et al., 2021). Highlights during the Gondwana break up and the Atlantic marginal sedimentary basins deposition context (Valanginian to Aptian), with the Rift Sequence (135 – 118 Ma) and Transitional Sequence (118-112 Ma).

CHAPTER 3 – METHODS

ANALYTICAL TECHNICS APPLIED TO FRAGATA WELL CORE SAMPLES

1 INTRODUCTION

This case study concerns the silicification in laminated mudstones obtained from the Pre-salt (Aptian, Macabú Fm. – Campos Basin) located at ultra-deep waters on the South Atlantic Ocean margins. The studied material belongs to FRAGATA well [6DEV-18PA-RJS] accessed with the ANP permission [Official letter nº 424/2019/SDT/ANP-RJ-e, 0f 26/06/2019, SEI – 48610.211854/2019-70], as part of the DIAGENESIS Project - "Diagenesis of the Pre-Salt carbonate sequences and its impact in the exploration and production of hydrocarbon reservoirs" [Grant number 23075.193990/2017-07], from a Technical-Scientific Cooperation between Shell Brazil and the Federal University of Paraná (Lamir Institute).

To provide an integrated geochemical analysis of the diagenetic processes in the Campos Basin. The core is described in high detail (1:100) and includes information on sedimentary facies, deformation structures, and geophysical profiles (gamma-ray, neutron-density, sonic). In addition, rocks were carefully described and sampled during the access. So far, 268 samples (plugs, tablets, and drill cuttings) have been collected and are available for use.

In this context, three core samples were selected from Fragata for a detailed study focusing on silicification processes. This chapter presents a narrative review of the laboratory processing and analytical techniques applied to the selected samples to obtain a detailed characterization of petrography, mineralogy, and geochemistry.

2 FRAGATA WELL - PREVIOUS STUDIES AND SAMPLE SELECTION

The studied material belongs to the Pre-salt reservoirs, specifically to Fragata well, drilled at the Transitional Sequence - Macabú Formation from Campos Basin in the south Brazilian Atlantic continental margin (parallels 20° and 25°). The Campos basin occupies approximately 100,000 km^2 offshore, close to Rio de Janeiro and Espírito Santo states. The Fragata well's drilling occurred from August to November 2010, by DEVON ENERGY BRAZIL, with recovered sampling from 4.858m to 5.185m depth, at block BM-C-34 (C-M-471), where the primary target coordinates are UTM N 360244.51 and E 7430877.80, with well-drilled beginning at N 360248.32 and E 7430913.02.

The recorded profile generated during the process (Fig 1) shows the stratigraphic column composed of carbonates with shale intercalations and the top dominated by halite with anhydrite intercalations. As part of the DIAGENESIS Project, the scientific research developed with the Fragata well in 230 core samples and 110 thin sections from 138 meters (5.015m to 5.152m), involving a combination of analytical methods including petrography (stereo and optical microscope, SEM-EDS, µCT), mineralogy (XRD), geochemistry (FRX, ICP-MS), and isotopic (C&O, Clumped, Sr). In summary, Fragata well is composed of laminated mudstones intercalated with laminites, rudstones, microbialites, and nodules/layers of silica filling porosities, and replacing crystals are largely recorded.

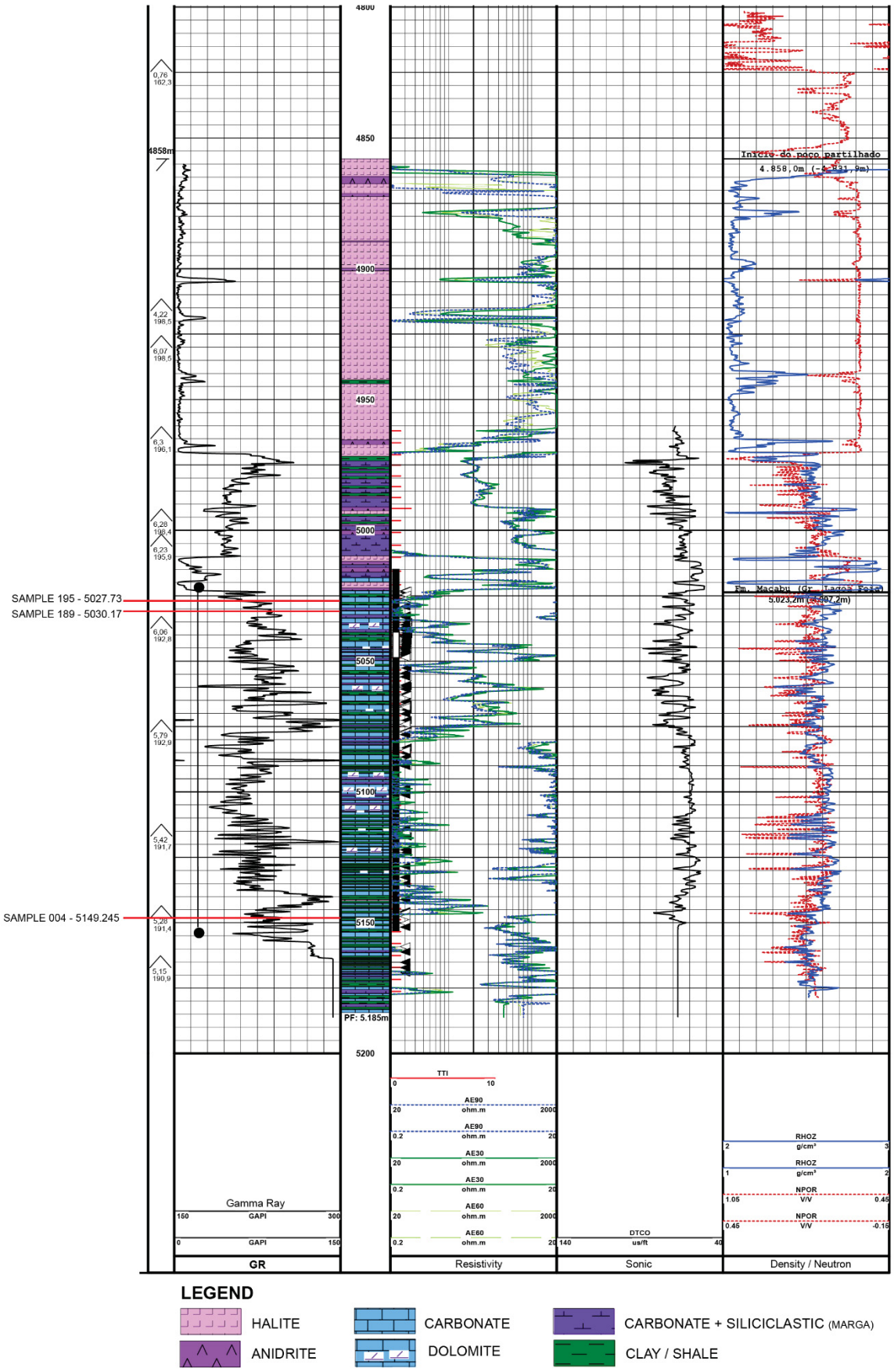

Figure 1: Recorded profile during Fragata well drilling process, with a highlight for the studied sample depth location. Source: Diagenesis Project - Devon drilling data.

3 SAMPLE PREPARATION

The analytical methods applied to the selected samples to obtain a detailed, microscale result. Focus on mineralogical variations directly related to silicification by differentiating textural patterns and mineral groups. The chosen core samples were cut into slices of approximately 1 cm and directed to preparation stages and analytical procedures (Fig. 2).

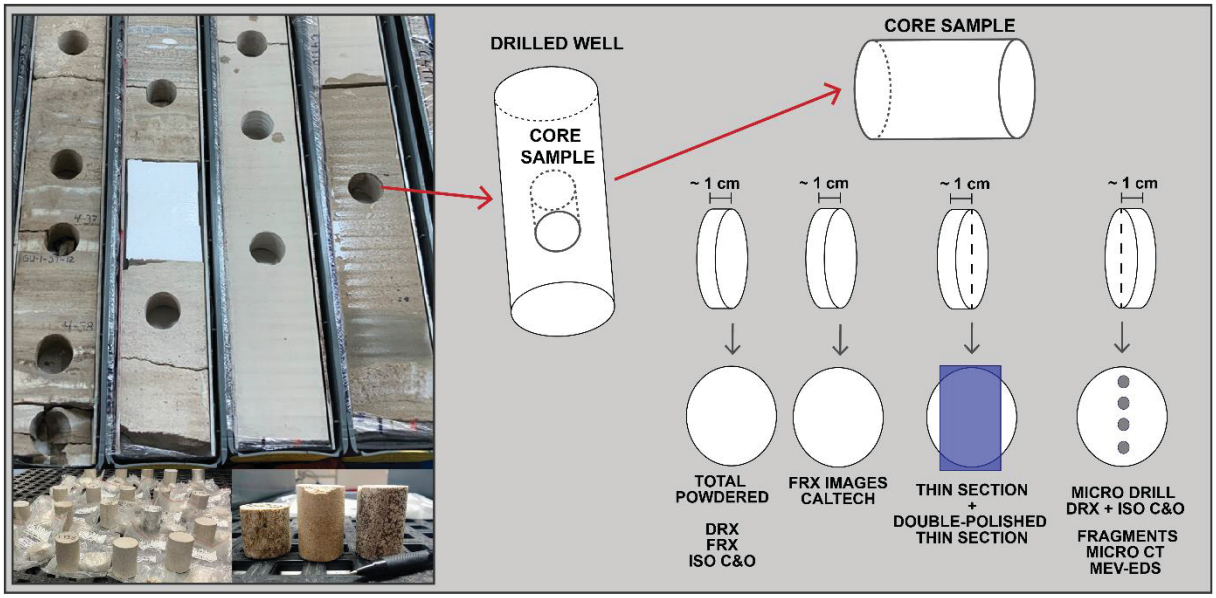

Figure 2: Drilled well and core samples example, with an illustrative cut scheme for preparation and analytical procedures. Photo source: Diagenesis Project previous data.

Three thin sections were confectioned in blue epoxy resin for the petrographic studies. In addition, for testing fluid inclusion studies, two double-polished thin sections were produced. Sample preparation for geochemical and mineralogical analysis took place in two stages. First, a sample piece of approximately seven grams was powdered (325 to 400 mesh) in a tungsten carbide mill (iLamir/UFPR) and submitted to X-ray fluorescence, X-ray diffraction, and C&O stable isotopes according to iLamir routine, for preliminary results.

Detailed samples were collected using a micro-diamond tip drill following mineralogical and textural variation. These samples were submitted to X-ray diffraction to obtain results of variations in mineralogical composition and detect minerals present in smaller proportions not detected in the complete powdered samples analysis and C&O stable isotopes, to observe changes in the isotope signature according to microscale mineralogical and textural variations. In addition, the remaining fragments were brooked and Au|Pd metalized for SEM-EDS analysis to complement the petrographic studies preparation.

3 PETROGRAPHY, MINERALOGY, AND GEOCHEMISTRY ANALYSES

This research involves petrography studies under a stereomicroscope, optical and UV fluorescence microscopy, bright field scanner, scanning electron microscopy (SEM-EDX), X-ray microtomography (μCT), and Micro XRF spectrometer. In addition, to mineralogical and geochemical studies in powdered samples, through X-ray diffraction (XRD), X-ray fluorescence (XRF), and C&O stable isotopes. The carbonates descriptions follow Dunham (1962), modified by Embry & Klovan (1971), porosity classification is according to Choquette and Pray (1970), and mineral abbreviation follows Whitney e Evans (2010) (Choquette and Pray, 1970; Dunham, 1962; Embry and Klovan, 1971; Whitney and Evans, 2010).

3.1 PETROGRAPHY - OPTICAL AND UV MICROSCOPE

Petrographic analysis was the main tool for identifying and characterizing the samples' mineralogical composition, structures, and textures to establish a chronology for the mineralogical assemblage's precipitation order. The petrographic studies began through the macroscopic studies under a stereomicroscope Zeiss Stereo Discovery V12 (magnification 5x to 60x), with Axion Vision Software for image capture.

In sequence, a conventional study with description and image capture under bright field and polarization occurred in a microscopic model Zeiss Stereo Imager.A2m, with an Axion Vision Software (iLamir /UFPR). In addition, Fluorescence studies were made in an Olympus BX51 (CTAF/UFPR), with the Cell^F for image captures. Finally, to optimize bright field studies, thin section scans under the Scanner Zeiss Axio Imager Z2, MetaSystems also consists of the obtained results.

3.2 SCANNING ELECTRON MICROSCOPE WITH X-RAY DISPERSIVE ENERGY

To refine the petrographic studies with high-resolution data regarding mineral identification, morphological features, structural and textural aspects, and chemical composition. The electronic image forms due to electron beam incidence and interaction with the sample surface. The different answer depends on the detector selected, including:

(1) Secondary electrons (SE) - generates high-resolution images, similar to a three-dimensional image, with fidelity to sample topography;

(2) Backscattered electrons (BSE) – consist of high energy and elastic scattering coming from internal levels of the samples, with more fidelity to compositional and density differences; The SEM also can be coupled to an energy dispersion X-ray spectrometer (Energy dispersive

system) allowing chemical analysis, indicating compositional variations in samples, through punctual or field scanning data (Dedavid et al., 2007; Welton, 2003).

Fragments without metallization were submitted to a scanning electron microscopic (SEM-EDS) using a TESCAN VEGA3 LMU EDS type chemical analysis system (Oxford) with AZ Tech software (Advanced) with 80 mm² SDD type detector (CME/UFPR). In addition, Au|Pd - coated thin sections and fragment sample analyses were performed on JEOL6010LA with EDS model EX-94410T1L11. The data acquired consists of secondary electrons images (SE), Cathode images (AUX), and backscattered electrons images (BSE), with chemical composition maps and composition by point obtained through Energy dispersive X-ray spectrometer (EDS).

3.3 COMPUTERIZED MICROTOMOGRAPHY (μCT)

For complement petrographic studies, X-ray computed microtomography analysis quantifies and evaluates pore morphology and morphometry besides the attenuation coefficients from different minerals, allowing a three-dimensional material reconstruction. In addition, the μ-CT dataset enables evaluation of the layers' consistency throughout the sample and the content of various minerals. However, it cannot accurately identify elements and minerals (Nascimento-Dias, 2017; Reis Neto et al., 2018). The microtomography analysis proceeded in a Skyscanner model 1172, with tube voltage 90kV, current 112μA, and 12.8 8μm/pixel resolution (iLamir/UFPR).

3.4 X-RAY DIFFRACTION (XRD) - MINERALOGY

The X-ray diffraction technique identifies mineral phases in the samples and evaluates the semi-quantitative proportion for each mineral. The main principle involved in this technique is the orderly atomic arrangement of mineral crystallographic structure. The minerals form a three-dimensional structure with a periodic and regular pattern along the crystallographic axis. The interplanar distances separating atoms are named d-spacing. Since these interplanar distances have the X-ray wavelengths magnitude order, and each mineral has a characteristic spectrum emission, it is possible to proceed with radiation incidence through the interesting material and record the diffracted photons by this material (Klein and Dutrow, 2012).

The analysis was performed through a Panalytical diffractometer model Empyrean (iLamir/UFPR) with an X-accelerator detector equipped with a Cu tube and High Score software for data treatment. Scans from bulk samples were run from 2θ angles of 3°to 70°, using a step

size of 0.016° and count time of 10.16 s per step. The scan rate is 0.5º/min, under voltage 40kv and current 30mA.

3.5 X-RAY FLUORESCENCE - CHEMISTRY

X-ray fluorescence consists of a multielement analytical technique used to identify the chemical presence (wt.%) of the major earth elements in the form of oxides (CaO, MgO, SiO_2, $Al2O_3$, $Fe2O_3$, Na_2O, K_2O, TiO_2, MnO, and P_2O_5) and trace elements (Ba, Ce, Cu, La, Nb, Nd, Pb, Rb, S, Sr, V, Y, Zn, Zr). This technique allows quantitative and semi-quantitative chemical composition determination. In summary, the method involves driving an X-ray beam to the material, exciting the electrons, causing the primary radiation absorption and secondary radiation emission. Then, with the electrons returning to their low energy level, a photoelectric effect is caused. As a result, each element has its characteristic fluorescence pattern, allowing chemical identification and quantification (Santos, 2013). Quantitative X-ray fluorescence (XRF) was obtained in a Malvern Panalytical model Axios-Max with Rh tube, and the interpretation was under software Super Q 5.3 (iLamir/UFPR).

3.6 CARBON AND OXYGEN STABLE ISOTOPES

C and O stable isotopes analysis under a Gas Bench II and a Thermo Delta V Advantage mass spectrometer (Thermo Fisher Scientific) housed at iLamir/UFPR, following Révész (2002), according to the iLamir routine. Approximately 400 to 600 µg, digested with orthophosphoric acid (72°C). On a V-PDB scale, the results follow reference materials (IAEA-603, IAEA-CO-9, NBS18, NBS19). Standard deviation (1σ) reported the internal variation of 8 to 10 readings of the same preparation (Hoefs, 2009; Révész and Landwehr, 2002).

CHAPTER 4 – RESULTS AND DISCUSSIONS (*Manuscript*[1])

GEOCHEMISTRY APPLIED TO FRAGATA WELL TO STUDY SILICIFICATION IN LAMINATED CARBONATES FROM CAMPOS BASIN, PRE-SALT - BRAZIL.

1 INTRODUCTION

The Brazilian hydrocarbon reservoirs, termed Pre-salt, are among the largest reserves in the world. Their importance resides in society's need for hydrocarbons, widely used as an energy source, fuel, and base for several materials and industrial processes. Therefore, understanding these reservoirs' deposition, diagenesis, and tectonic influences is essential for better use of these resources (Carminatti et al., 2009; Herlinger et al., 2017; Saller et al., 2016).

Located at the South Atlantic margin basins (Campos and Santos - Brazil), the Pre-Salt reservoirs have a specific geological setting with particular features, where the succession consists of the *Upper Rift Sequence* with bivalve and oncoidal rudstones/grainstones deposits, followed by the *Transitional Sequence* represented by non-marine carbonates, both with significant hydrocarbon content sealed by large evaporites layers (Gomes et al., 2020; Herlinger et al., 2017; Lima et al., 2019; Milani et al., 2017; Thomaz Filho and Milani, 2018). The reservoir's quality depends on porosity and permeability, which are directly affected by silicification, dolomitization, dissolution, recrystallization, and cementation processes. Moreover, these aspects are still related to deep burial or hydrothermal fluid circulation through faults and fracture systems. This process essentially results in a secondary paragenesis represented by saddle dolomite, chalcedony, fluorite, sulfides, and sulfates (Barite, anhydrite, sphalerite, and pyrite), also called "exotic" or "unusual" cements (De Luca et al., 2015; Lima et al., 2020, 2019; Wright and Tosca, 2016).

Considering the importance of hydrocarbon reservoirs for society and how diagenetic processes affect the reservoir quality, this research aims to contribute to the knowledge about the Pre-salt hydrocarbon reservoirs, providing an overview and characterization of diagenetic and fluid circulation features based on mineral assemblages. The following results focus on Fragata well core samples from the Pre-Salt section located at South Atlantic margin basins (Campos Basin, Macabu Formation - Transitional Sequence). Moreover, it proposes specifically: (1) distinguish petrographic, geochemical, and isotopic features related to post-depositional processes and fluid circulation; (2) present a detailed description of textural pattern

[1] The manuscript will be submitted to Journal of Marine and Petroleum Geology.

and chemistry variation on the mineral assemblages; (3) characterize the fluid circulation influence, and the micro-environmental chemistry changes;

2 GEOLOGICAL SETTINGS

The Pre-salt reservoirs are located at the Brazilian continental margin of the Central South Atlantic (Fig. 1), inserted in the context of the marginal sedimentary basins. The Brazilian Pre-salt is a succession of sedimentary rocks composed of continental carbonates (source and reservoir) with an important hydrocarbon content around 5000 meters below sea level and sealed by evaporites of the upper layers (Salt layer – seal), which gives rise to the Pre-salt name (Herlinger et al., 2017; Lima et al., 2019; Thomaz Filho and Milani, 2018).

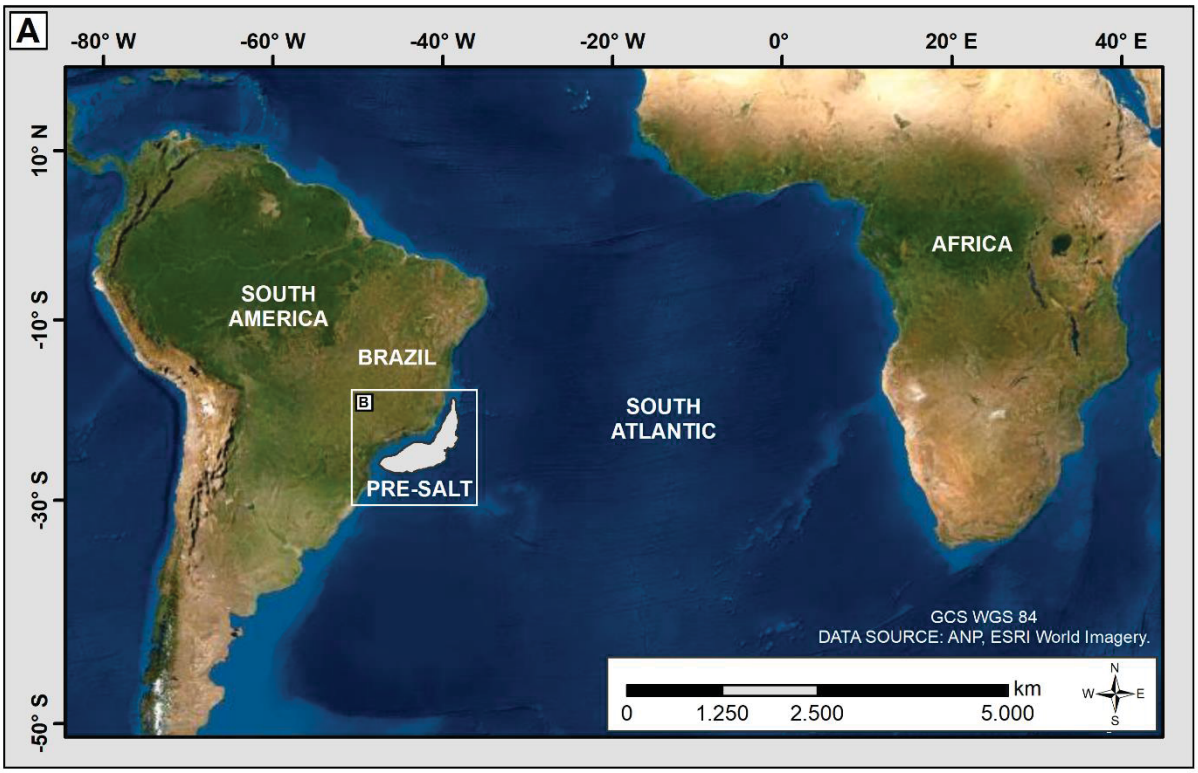

Figure 1: Study area location, Pre-salt in South Atlantic Brazilian margin;

The stratigraphic framework in the Brazilian (Campos and Santos) and African (Angola, Congo, Kwanza) marginal basins evidences their genesis in an extensional context as divergent margin-type basins related to the Gondwana breakup and the Atlantic Ocean formation during the Late Jurassic until the Early Cretaceous. (Carminatti et al., 2009; Castro and Picolini, 2015; Guardado et al., 2000; Mohriak et al., 2012; Saller et al., 2016). The studied lithotypes belong to Fragata well, drilled at Campos Basin, in the south Brazilian Atlantic continental margin (parallels 20° and 25°), which occupies approximately 100.000 km^2 in deep waters close to Rio de Janeiro and Espírito Santos states. The Fragata well's drilling occurred from August to

November 2010, by DEVON ENERGY BRAZIL, with recovered sampling from 4.858m to 5.185m depth, at block BM-C-34 (C-M-471), where the primary target coordinates are UTM N 360244.51 and E 7430877.80, with well-drilled beginning at N 360248.32 and E 7430913.02 (Fig. 2).

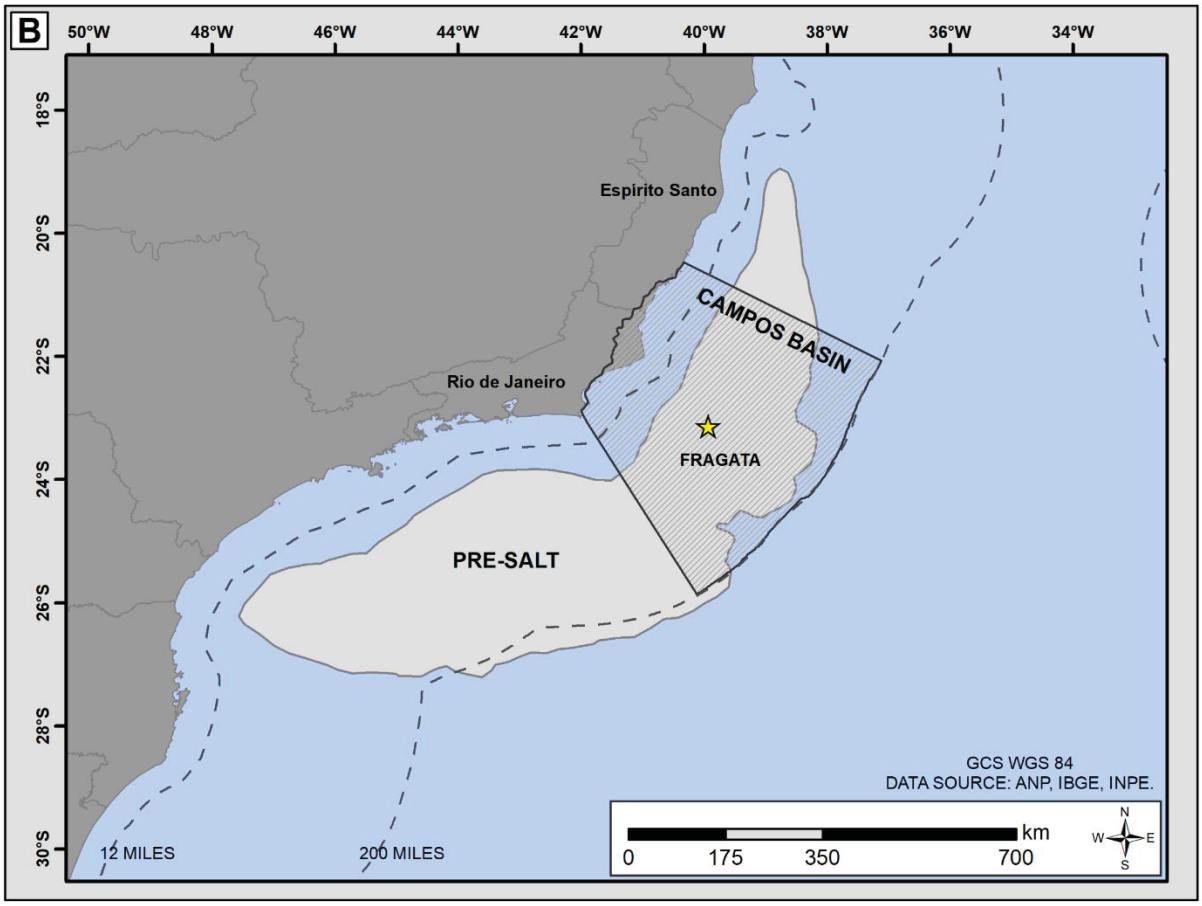

Figure 2: Location of the Fragata well in Campos Basin Pre-salt reservoirs;

The Central South Atlantic Marginal Basins geological record represents three tectonosedimentary units as evidence of the extensional context: (1) Rift Sequence; (2) Transitional Sequence; and (3) Final Drift or Passive Margin Sequence (Cainelli and Mohriak, 1999; Castro and Picolini, 2015; Guardado et al., 2000; Mohriak et al., 2012; Thomaz Filho and Milani, 2018). The tectonosedimentary units are described below, focusing on the Campos basin:

(1) *Rift Sequence* (Lagoa Feia Group, basal interval) - represents the onset of the Central South Atlantic Marginal Basins geological record, starting with an increased lithospheric extension an asthenosphere elevation, around 135 to 118 Ma (Barremian to Aptian rift stage). The tholeiitic volcanism forms the Paraná-Etendeka LIP, followed by continental sedimentation filling elongated deep lakes (Cabiúnas Formation). These flood basalts occur recovered by

fluvial and lacustrine siliciclastic deposits (Itabapoana and Atafona Formation). The Upper Rift is marked by playa-lake and pluvial lake deposits, formed of bivalve/gastropods bioclast and oncolytic deposits, classified as rudstones and grainstones (Coqueiros Formation). The Pre-Alagoas regional unconformity marks the end of the Rift Sequence and also implies elevation and rift section erosion (Castro and Picolini, 2015; Herlinger et al., 2017; Lima et al., 2019; Mohriak et al., 2012);

(2) *Transitional Sequence* (Lagoa Feia Group, upper interval) - characterized by continental to marine sedimentation, dated from 118 to 112 Ma, which recovers the Pre-Alagoas unconformity with lacustrine deposits (Gargaú Formation), clastic deposits (Itabapoana Formation), spherulitic and fascicular carbonates interbedded with argillaceous and laminated carbonates (Macabú Formation). The Pre-salt is hosted in carbonate deposits from Upper Rift and Transitional Sequence (Castro and Picolini, 2015; Herlinger et al., 2017; Lima et al., 2019; Mohriak et al., 2012). In addition, the Transitional Sequence is delimited (sealed) by complete evaporite sequences (Retiro Formation) of anhydrite, halite, and bittern salts (sylvite and carnallite) formed under dry conditions due to the restricted marine incursions from the meridional portion of the Atlantic Ocean (Gomes et al., 2020; Herlinger et al., 2017; Lima et al., 2019; Wright and Tosca, 2016). The Walvis Ridge, associated with the Tristan da Cunha hotspot, is an important barrier in the Pre-salt geological record since the topographic highs prevented marine ingress, allowing fluvial-lacustrine conditions. The Walvis Ridge subsidence at the end of this stage allowed the marine incursions, leading to the evaporite formation (Rochelle-Bates, 2019).

(3) *Final Drift or Passive Margin Sequence* (Macaé and Campos Group) – overlying the evaporites occur proximal marine deposits formed in a deep transgressive context (Macaé Group). This interval ends with a regional unconformity at 93 Ma, followed by the Campos Group deposition with proximal (Emborê Formation), distal (Ubatuba Formation), and turbidites deposits (Carabeus Formation) (Castro and Picolini, 2015; Milani et al., 2017; Thomaz Filho and Milani, 2018).

3 METHODS

Three core samples were selected for a detailed study focusing on silicification processes. The research conducted petrographic, mineralogic, chemistry, and isotopic analyses. Respectively under a stereomicroscope, optical microscope, UV fluorescence microscopy, scanning electron microscopy (SEM-EDX), X-ray microtomography (μCT), X-ray fluorescence spectrometer, X-ray diffraction (XRD), X-ray fluorescence (XRF), C and O stable isotopes (iLamir/UFPR).

3.1 PETROGRAPHY, MINERALOGY, AND GEOCHEMISTRY

Macroscopic studies on core samples were conducted at a stereomicroscope Zeiss Stereo Discovery V12 (magnification 5x to 60x), with Axion Vision Software for image capture. In Sequence, three thin sections with blue epoxy resin for porosity enhancement passed through a petrographic characterization at microscopes with different purposes. First, in a conventional study and images captured on a bright field, polarization occurs under a microscopic model Zeiss Stereo Imager.A2m, with an Axion Vision Software (iLamir /UFPR). In addition, Fluorescence studies were made in an Olympus BX51 (CTAF/UFPR), with the Cell^F for image captures. Finally, to optimize bright field studies, thin section scans under the Scanner Zeiss Axio Imager Z2, MetaSystems also consists of the obtained results.

For high-resolution petrography with chemistry characterization, Au-coated sample fragments were submitted to a scanning electron microscopic (SEM-EDX) for high-resolution petrography and chemistry analysis. They were first analyzed in a TESCAN VEGA3 LMU EDS type chemical analysis system (Oxford) with AZ Tech software (Advanced) with an 80 mm^2 SDD type detector (CME/UFPR). Then, in sequence, the analyses proceed in a JEOL SEM model 6010LA. For complement petrographic studies, X-ray computed microtomography analysis (μCT) in a Skyscanner model 1172 (iLamir/UFPR) quantifies and evaluates pores morphology and morphometry besides the attenuation coefficients from different minerals.

Samples facies descriptions follow Dunham (1962), modified by Embry & Klovan (1971), porosity classification is according to Choquette and Pray (1970), and Mineral abbreviation follows Whitney e Evans (2010) (Choquette and Pray, 1970; Dunham, 1962; Embry and Klovan, 1971; Whitney and Evans, 2010).

Bulk-rock samples were powdered (325 to 400 mesh) in a tungsten carbide mill (iLamir/UFPR) for X-ray fluorescence, X-ray diffraction, and C&O stable isotopes. In addition, XRD and C&O isotopic analysis under punctual sampling by micro-diamond tip drill (iLamir/UFPR) following mineralogical assemblages' variations. Quantitative X-ray

fluorescence (XRF) was obtained in a Panalytical model Axio-Max with Rh tube (iLamir/UFPR) to identify the chemical composition (wt.%) of the major oxides (CaO, MgO, SiO_2, $Al2O_3$, $Fe2O_3$, Na_2O, K_2O, TiO_2, MnO, and P_2O_5) and trace elements (Ba, Ce, Cu, La, Nb, Nd, Pb, Rb, S, Sr, V, Y, Zn, Zr). Mineralogical composition (XRD) through a Panalytical diffractometer model Empyrean (iLamir/UFPR) with an X-accelerator detector equipped with a Cu tube. Scans from bulk samples were run from 2θ angles of 3°to 70°, using a step size of 0.016° and count time of 10.16 s per step.

The distinction between calcite minerals follows Tucker's (1990) classification based on magnesium content: < 4 mol% of Magnesium represents low Mg-calcite, 4 to 19 mol% represents high magnesium calcite, and > 20% of Mg content forms dolomite. 30 to 45 mol % represents calcium-dolomite (disordered dolomite / proto-dolomite), and 45 to 50 mol% represents dolomites. Following Zhang et al. (2010), the chemical composition obtained through XRF in weight percent of oxides was normalized to moles and correlated with d-spacing obtained through XRD (Tucker, 1990; Zhang et al., 2010)

C&O stable isotope analysis under a Gas Bench II and a Thermo Delta V Advantage mass spectrometer (Thermo Fisher Scientific) (iLamir/UFPR). Approximately 400 to 600 µg, digested with orthophosphoric acid (72°C) for two hours. The results on a V-PDB (Vienna Pee Dee Belemnite) scale follow reference materials (IAEA-603, IAEA-CO-9, NBS18, NBS19). Standard deviation (1σ) reported the internal variation of 8 to 10 readings of the same preparation. To observe microscale variations in the signature of the carbon and oxygen stable isotopes present in the silicified portions of the Fragata well, specific and punctual sampling was carried out with a diamond micro-tip drill, with at least three points sampling for each microfacies. Since the sample contains a high proportion of silica than carbonates, the general tendency of the results is according to the average value of the punctual results, with the main trend delimited by the standard deviation (σ) multiplied by three ($\bar{x}$ σ * 3).

4 RESULTS

The following results contain a microscale petrographic, mineralogical, chemistry, and isotopic characterization of three core samples from the Fragata well (Macabú Formation – Campos Basin). The description presents the mineral variations in composition, structural and textural pattern, with the following topics for each sample:

CORE SAMPLE DESCRIPTION (SAMPLE CODE – DEPTH)

1 Petrographic microfacies

Laminated Mudstones

Chert: Granular crypto/microcrystalline silica

Chalcedony: Fibrous crypto/microcrystalline silica

Mega-Quartz: Granular microcrystalline silica

Sulfides (Pyrite), Sulfates (Gypsum and Barite), and organic matter (Carbon)

2 Chemical composition

3 Mineralogical composition

4 Carbon and Oxygen stable isotopes

4.1 CORE SAMPLE DESCRIPTION (CODE 125/20-004 – DEPTH 5149.245m)

The sample 125/20-004 represents a silica layer of about 10 cm in width, located at 5149.245m depth in the Fragata well (Fig. 3A). The core sample, measuring 4 cm in diameter and 4.5 cm in length, consists of a chert layer hosted in a laminated mudstone framework.

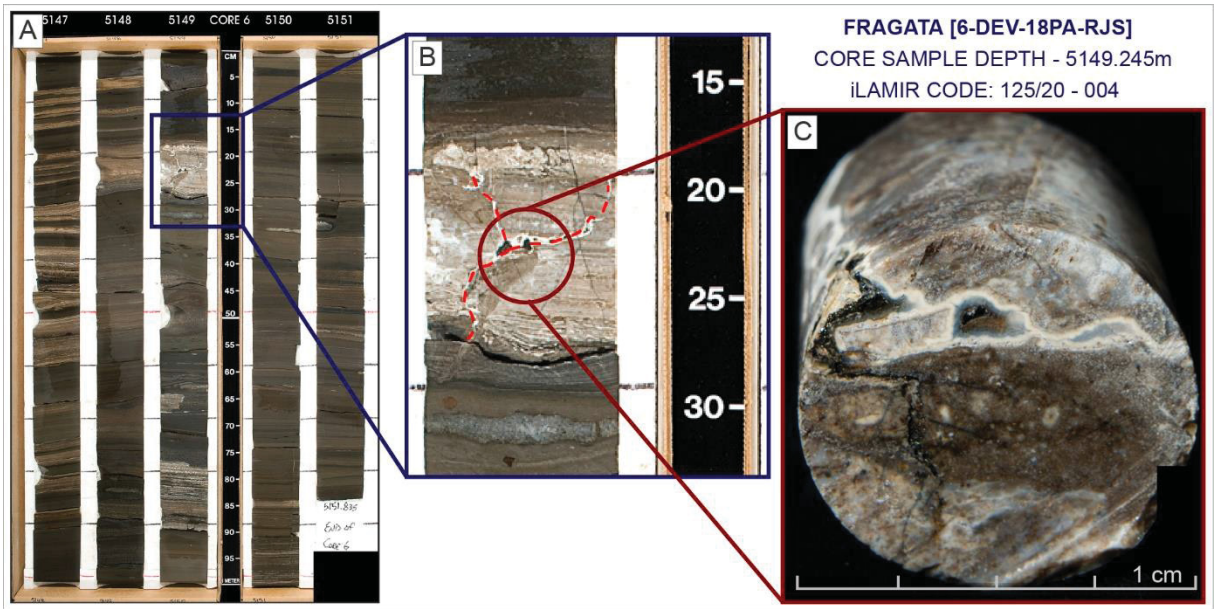

Figure 3: A. Samples from depths 5151 to 5147m; B. Silica layer measuring around 10cm in width, at depth 5149.245m with faulting forming a triple junction; C. Highlight for the core sample 125/20-004, composed by chert with calcite and dolomite, divided by a fault with brecciated material, cemented by chalcedony, in the remaining porosity, displays amorphous organic matter, euhedral quartz crystals, and octahedron pyrite.

Notably, a small fault with brecciated material splits the chert layer. The faulting is restricted to the silica layer, forming a triple junction without crossing the mudstone framework (Fig. 3B). A white chalcedony cements the breccia. The remaining porosity (small megapore, ≈10mm) contains euhedral mega-quartz crystals, octahedron pyrite (sulfides), and amorphous organic matter (bitumen) (Fig. 3C).

4.1.1 Petrographic microfacies

Chert: Granular crypto/microcrystalline silica

The silica layer (Fig. 4A) comprises granular cryptocrystalline (< 4 µm) to microcrystalline (> 4 to10 µm) silica crystals, popularly denominated as *Chert*, in association with carbonate crystals. Since the core sample is divided by a breccia fault, under microscale studies is possible to differentiate textural and structural variation concerning the minerals associated with the chert. For example, while one side contains calcite spherulite crystals (Fig. 4B), the other has blocky dolomite/ankerite (Fig. 4C).

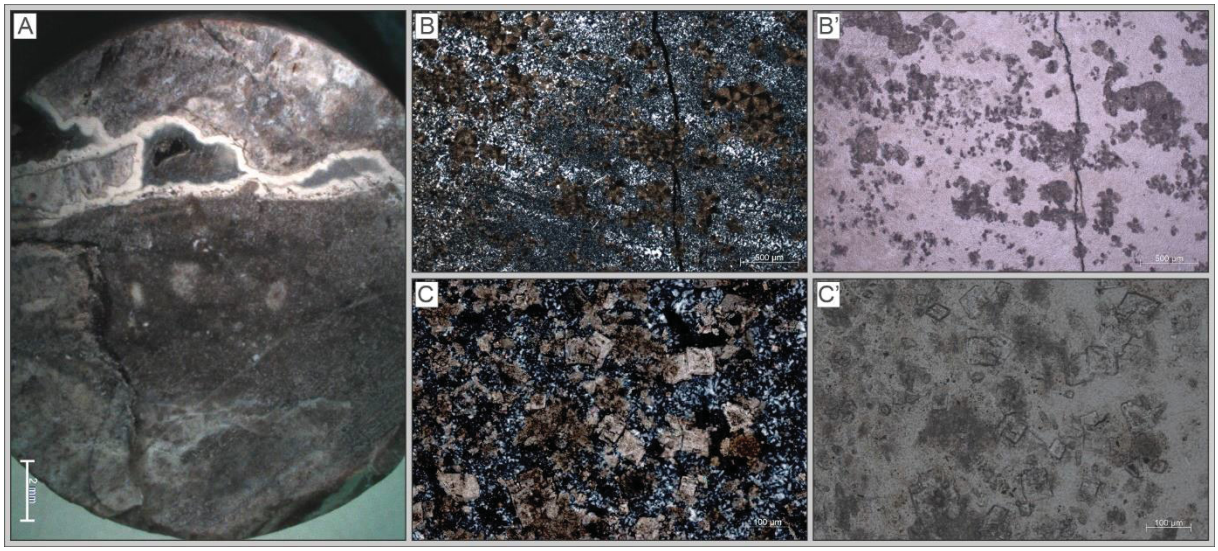

Figure 4: Granular crypto/microcrystalline silica (Chert) optical microscope and stereomicroscope. A. Chert layer, the core sample 125/20-004; B. Calcite spherulites crystals dispersed with floating texture in the middle of chert matrix; C Block dolomite/ankerite in chert matrix;

The calcite spherulite crystals in the middle of the silica layer are inequigranular, measuring between 50 to 200 µm, in a porphyrotopic texture. Approximately 20% of isolated and dispersed euhedral to subhedral calcite crystals floating in granular crypto/microcrystalline silica, indicating flow structure. While the side marked by dolomite contains rhomb and saddle dolomite crystals measuring around 100µm in a porphyrotopic texture where 20% of euhedral crystal occurs dispersed/floating in a granular crypto/microcrystalline silica matrix (Fig. 5A).

The results (XRD, SEM-EDX) evidence a possible, solid solution between dolomite and ankerite due to Fe content (Fig. 5B). Calcite crystals replaced by microcrystalline (> 4 to10 µm) silica also occur, giving a cloudy appearance to the chert (Fig. 5C), possibly due to the presence of EPS associated with the replaced calcite (Fig. 5D). While microcrystalline (> 4 to10 µm) silica replaces calcite crystals, cryptocrystalline (< 4 µm) usually occurs surrounding them (Fig. 5E). Halite is closely associated with silica, occurring as block halite dispersed/floating and also as cryptocrystalline (< 4 µm) halite (Fig. 5F).

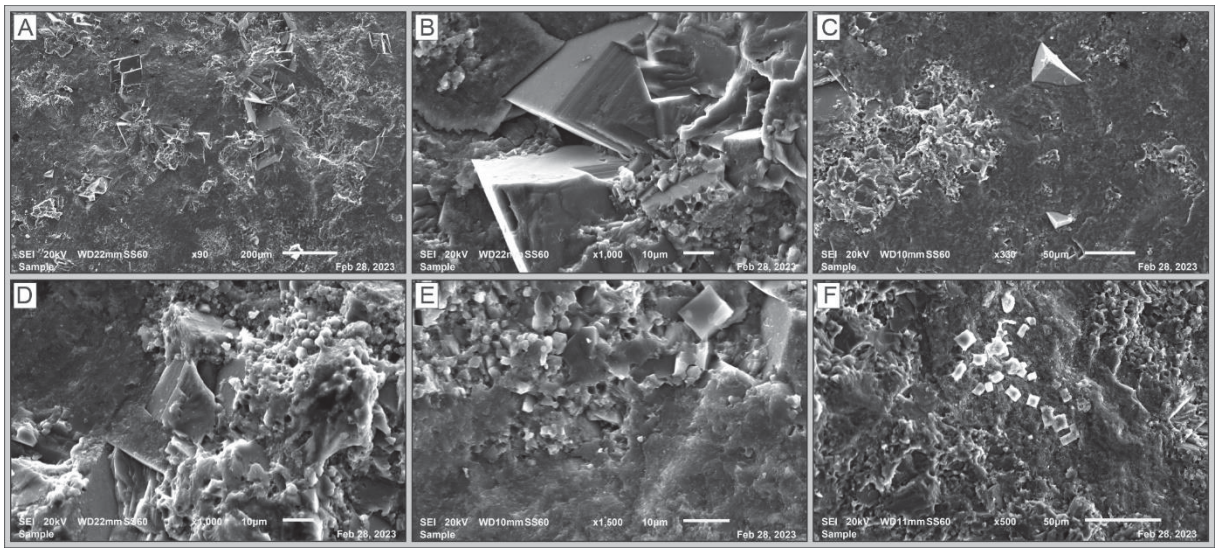

Figure 5: Granular crypto/microcrystalline silica (Chert) SEM images. A. Dolomite/ankerite dispersed/floating in chert; B. Saddle dolomite/ankerite; C. Calcite replaced by silica and halite block floating in cryptocrystalline silica; D. Highlight for EPS content in association with calcite; E. Calcite replaced by microcrystalline silica and surrounded by cryptocrystalline silica; F. Block and cryptocrystalline halite associated with cryptocrystalline silica;

Chalcedony: Fibrous crypto/microcrystalline silica

The petrographic fibrous cryptocrystalline silica, identified as chalcedony, cements the porosity formed by the brecciated fault in the chert layer (Fig. 6A). The white color (Fig. 6B) and the continuous (Fig. 6C) pattern along the pore walls characterize the core samples.

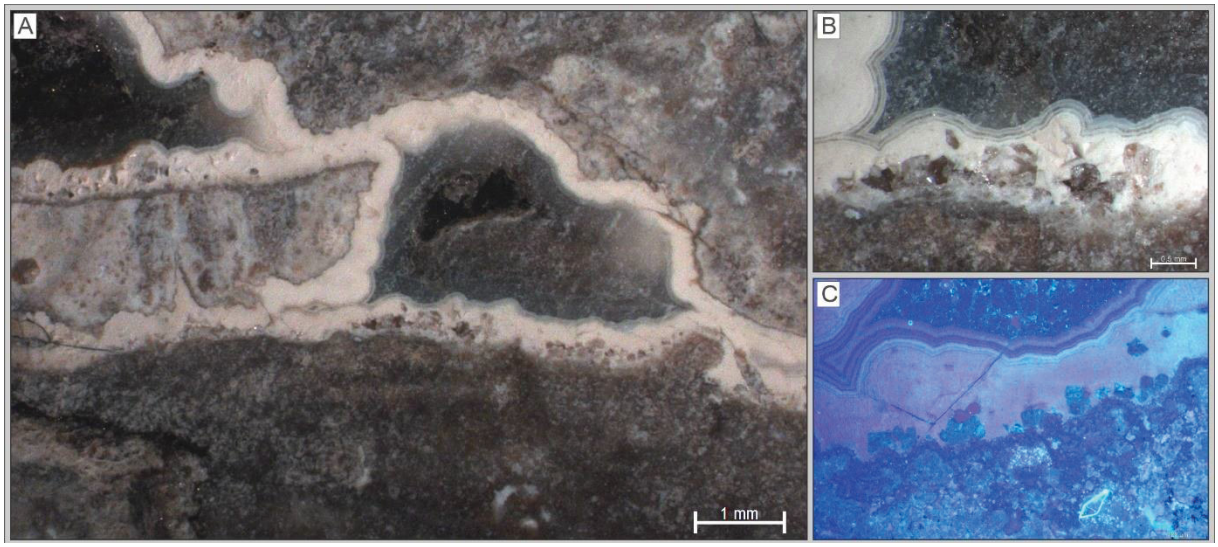

Figure 6: Fibrous cryptocrystalline silica (Chalcedony) at stereomicroscope and UV fluorescence microscope. A. Chalcedony cementing brecciated fault with a continuous pattern; B. Highlight for the white color of the chalcedony; C. Chalcedony under UV with a highlight for the continuous pattern.

Under thin sections and SEM analysis, cryptocrystalline silica (< 4 µm) continuously and perpendicular to the porosity walls stands out, forming an isopachous crust with fibrous and radiated aspects, measuring on average 500 µm in length (Fig. 7A, B). These radial pattern forms fans and hemispheroids, giving the botryoidal habit (spherical shape) to the chalcedony. In addition, spatic calcite and low-Mg calcite rhomb crystals measuring around 50 to 150 µm occur dispersed and sparse at the chalcedony on the underside of the sample (Fig. 7C). Finally, the fibrous cryptocrystalline silica ends with an abrupt transition to granular microcrystalline silica (mega quartz) (Fig. 7D).

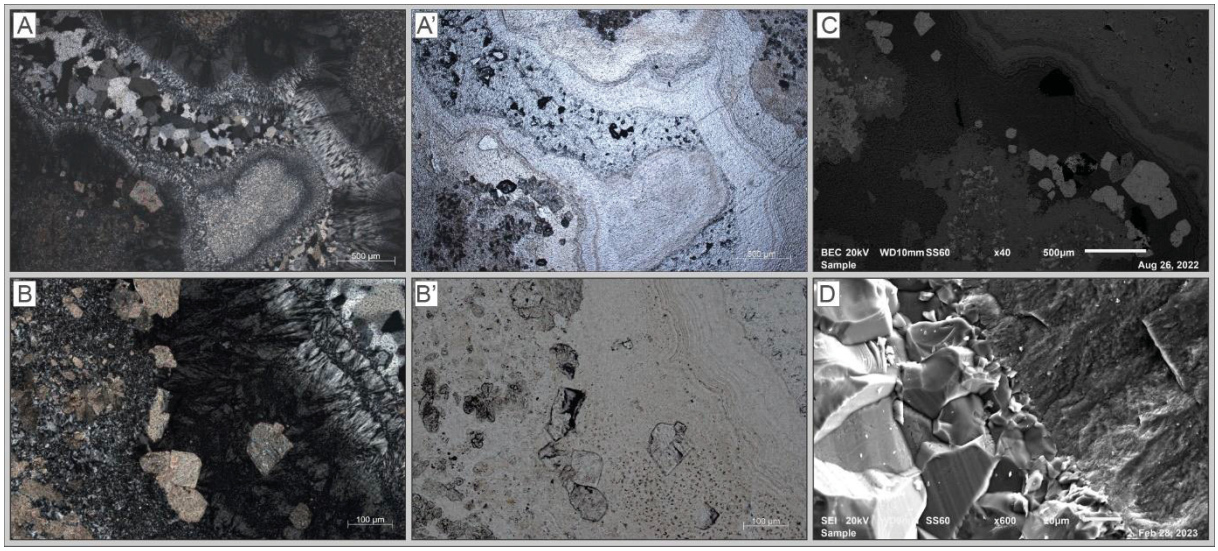

Figure 7: Fibrous cryptocrystalline silica (Chalcedony) at optical and SEM microscope. A, B. Chalcedony with a radiated fibrous aspect, forming fans and hemispheroids; C. Backscattered image showing the transition between chert, chalcedony, and mega quartz, with a highlight for calcite and Ca-dolomite (proto/ disordered dolomite) dispersed in the chalcedony; D. Abrupt contact between chalcedony and mega-quartz;

Mega-Quartz: Granular macrocrystalline silica

The macrocrystalline silica (mega-quartz) occurs, filling the remnant porosity after chalcedony cementation (Fig. 8A). The crystal size varies from 30 µm to 500 µm (very fine to medium crystalline) (Fig. 8B). The quartz crystals, when anhedral, show rectilinear contact, growing as euhedral Drusiform crystals with the normal habit when space is available (Fig. 8C).

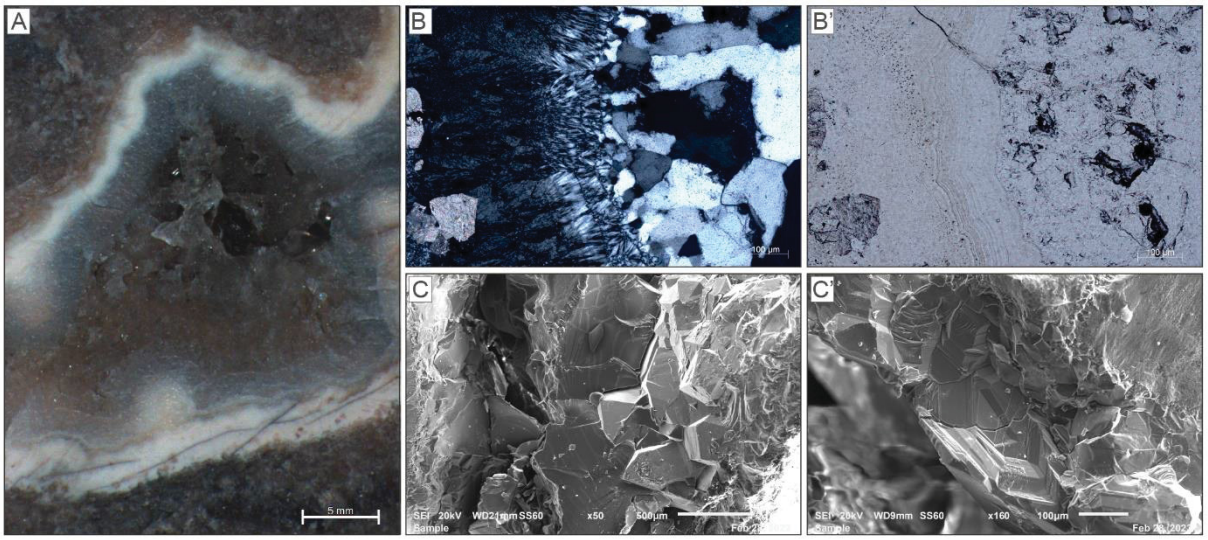

Figure 8: Granular macrocrystalline silica (Mega Quartz); A. Mega quartz filling remaining porosity after chalcedony cementation under a stereomicroscope. B. Highlight for transition between chalcedony to mega-quartz; C. SEM image of Mega-quartz crystals with euhedral normal habit and anhedral with rectilinear contact;

Sulfides (Pyrite), sulfates (Gypsum and Barite), and organic matter (Carbon)

After silicification, the fractures and vuggy porosity remain filled with octahedron pyrite crystals with 50-100 µm (very fine crystalline) (Fig. 9A, B) and amorphous organic matter (bitumen). In addition, rarely gypsum acicular crystals (Fig. 9C) measuring 10-20 µm (microcrystalline) and traces of barite with <10 µm (microcrystalline) also were observed dispersed in the framework.

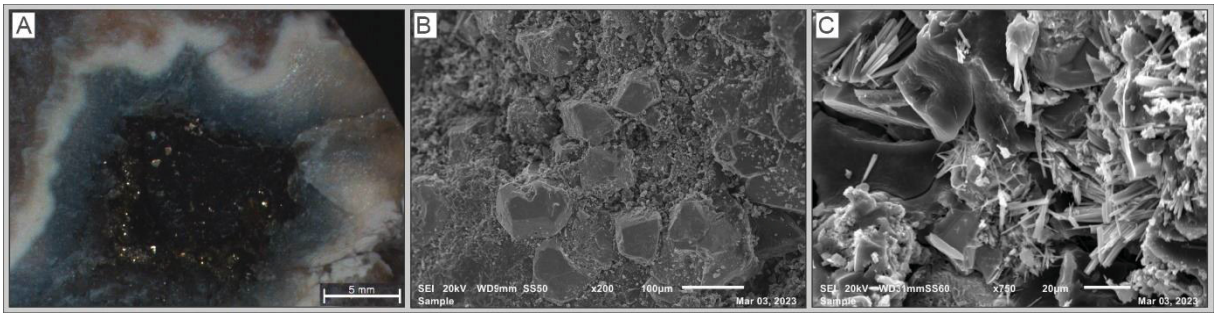

Figure 9: Sulfides (Pyrite) and Sulfates (Gypsum) filling vuggy porosity remaining after the silicification; A. Stereomicroscope image with a highlight for pyrite and amorphous organic matter filling vuggy; B. Octahedron pyrite under SEM; C. Acicular gypsum under SEM;

4.1.2 Chemical composition

Through bulk-rock analysis, the main components given in weight percent oxides: CaO, MgO, SiO_2, Al_2O_3, Fe_2O_3, Na_2O, K_2O, TiO_2, MnO, and P_2O_5.

Major oxides detected in more than 1wt% were (Fig. 10):

- SiO_2 (78.44%) representing the chert (granular crypto to microcrystalline silica), chalcedony (cryptocrystalline silica with fibrous-radial aspect), and mega-quartz crystals (macrocrystalline);
- CaO (10.15%) represents the calcite spherulite, blocky calcite, blocky and saddle dolomite;

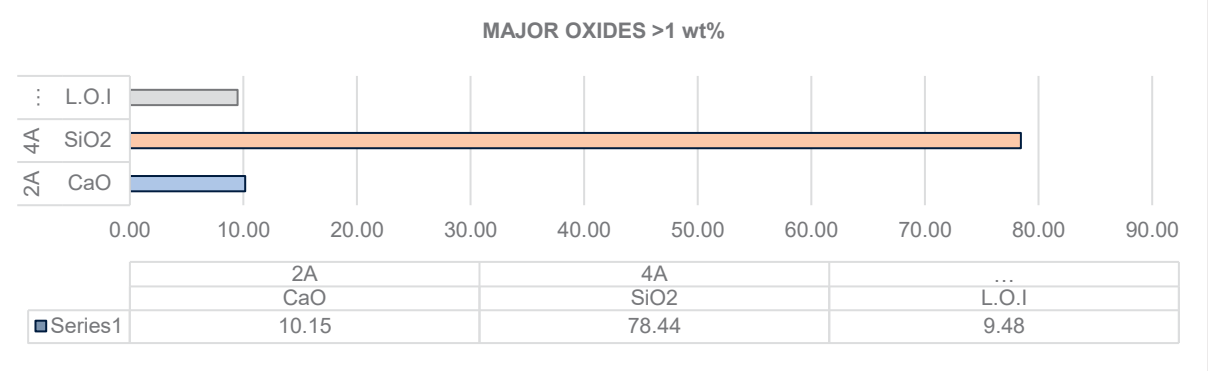

Figure 10: Bulk sample composition regarding Major Oxides detected in more than 1 wt%.

Major oxides detected in less than 1% were (Fig. 11):

- MgO (0.28%) in the forms of blocky and saddle dolomite crystals, probably in solid solution with ankerite through Fe_2O_3 (0.24%).
- Na_2O (0.19%) associated with Cl, forming halite;
- MnO (0.02%) is associated with dolomite/ankerite, possibly in magnesium substitution.
- Al_2O_3 occurs in less than 0.08%, while K_2O, TiO_2, MnO, and P_2O_5 in less than 0.02%.

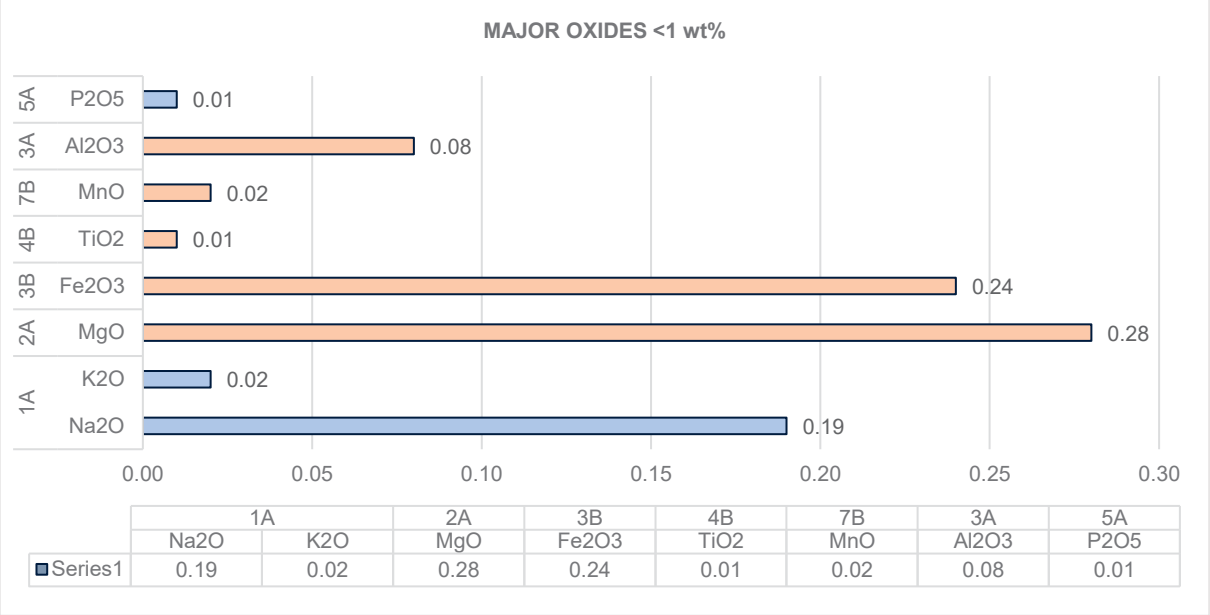

Figure 11: Bulk sample composition regarding Major Oxides detected in less than 1 wt%.

Trace elements detected with more than 100 ppm are (Fig. 12):

- Sulfur (S – 647 ppm), associated with Iron (Fe_2O_3 - 0.24%) forming octahedron pyrite.
- Barium (Ba – 360 ppm) appears as traces of barite.
- Strontium (Sr – 344 ppm) occurs as Calcium substitution.
- Zinc (Zn – 474 ppm) has a highlight in content in vuggy porosity and microfractures.

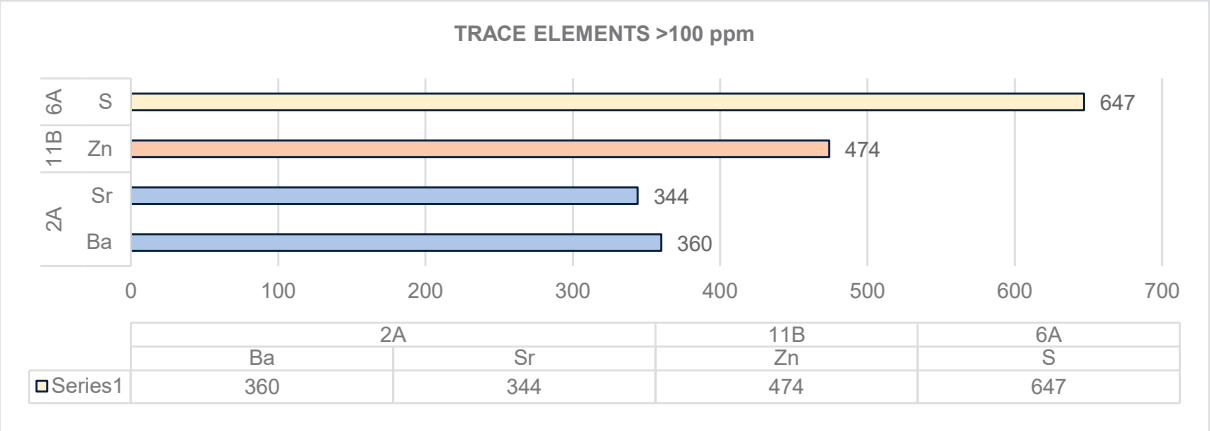

Figure 12: Bulk sample composition regarding Trace Elements detected over 100ppm.

In less than 100 ppm, trace elements detected are (Fig. 13):

- Rubidium (Rb - <3 ppm) and Neodymium (<51 ppm) show an association with silica.
- Vanadium (V – 9 ppm) showing highlight associated with Barium (Ba) and Titanium (Ti)

In less than 100 ppm, trace elements without a clear sample disposition were: Yttrium (Y - <4 ppm), Zirconium (Zr – 32 ppm), Niobium (Nb – 23 ppm), Copper (Cu – 6 ppm), Lead (Pb – 4 ppm), and rare earth elements detected were Lanthanum (La - <51 ppm), Cerium (Ce - <55 ppm).

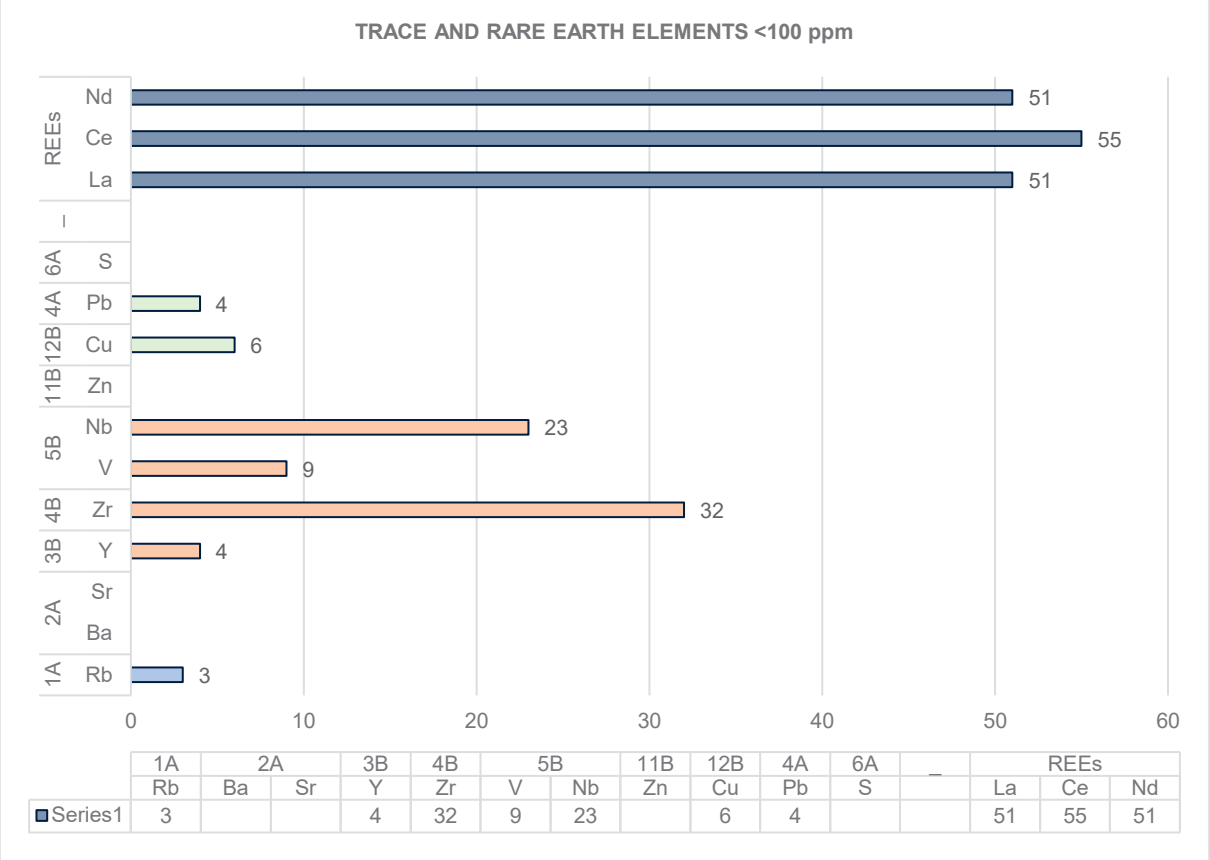

Figure 13: Bulk sample composition regarding Trace and Rare Earth Elements detected in less than 100ppm.

Element distribution through X-Ray Spectrometer images complements mineralogical and chemistry results showing a semi-quantitative chemistry elements distribution, allowing the observation of trace and rare earth elements spectra associated with the main mineralogical phases and structures as fractures, channel, or vuggy porosities (Fig. 14).

The main mineralogical components are carbonates (Calcite, Mg-Calcite, and Dolomite), evidenced through Calcium (Ca), Magnesium (Mg), and Iron (Fe) spectra, with Manganese (Mn) and Strontium (Sr) as trace elements in substitution phases, and Ytterbium detected as rare earth element anomaly. The silica occurs, filling pores and partially replacing carbonate crystals. The chert phase occurs in association with Aluminum (Al) and trace elements Bromine (Br), Palladium (Pd), Rhodium (Rh), Rubidium (Rb), Rhenium (Re), and Zirconium (Zr). In addition, the chalcedony strongly associates Sodium (Na) and Chlorine (Cl).

Trace elements related to fracture, channel, and vuggy porosities are Barium (Ba), Titanium (Ti), Vanadium (V), Zirconium (Zr), and Zinc (Zn).

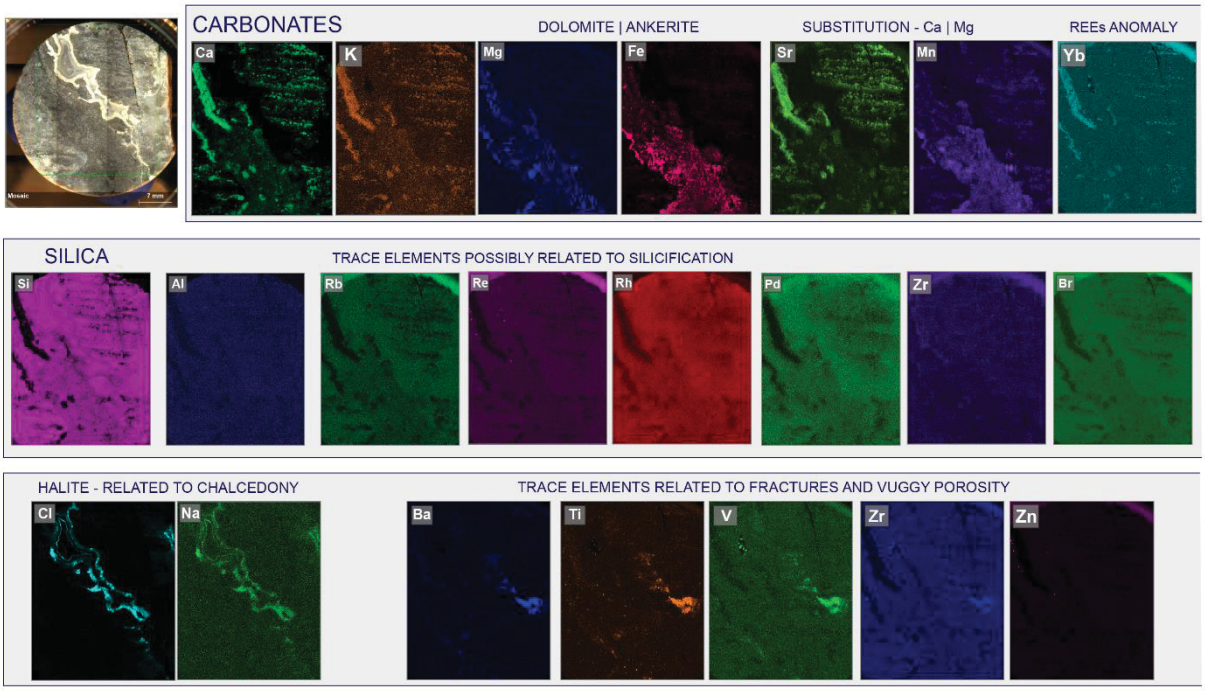

Figure 14: Elements distribution obtained through X-Ray Spectrometer. The elements' combination is according to mineralogical phases and sample structures.

In addition, Bromine (Br), Palladium (Pd), Rhodium (Rh), and Rhenium (Re) were detected by X-Ray Fluorescence Spectrometer Bruker (Caltech), showing association with silica. However, these elements do not appear at XRF through bulk rocks analyzed at the Panalytical.

4.1.3 Mineralogical composition

The sample semi-quantitative mineralogical composition detected through X-Ray Diffraction (XRD) analysis at homogenized and total powdered samples (Bulk rock) results in 83% alpha quartz, 10% low-magnesium calcite, 5% calcite, 2% calcium-dolomite. The micro sampling XRD analysis confirms a semi-quantitative mineralogical composition variation through the sample (Fig. 15), especially regarding dolomite/ankerite solid solution restricted occurrence evidenced in XRF spectra and petrographic analysis.

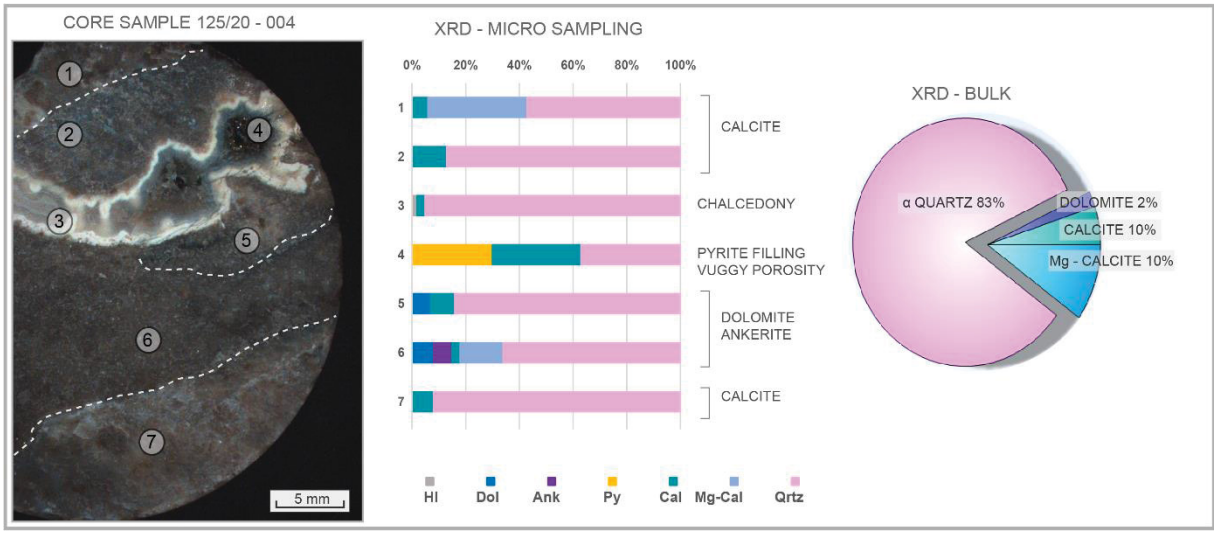

Figure 15: XRD semi-quantitative mineralogical composition for micro-sampling according to mineralogical variation.

4.1.4 Carbon and Oxygen stable isotopes

The isotopic signature is from calcite and low-magnesium calcite crystals, identified through XRD and XRF percentual calculation since the digestion performed in phosphoric acid at 70ºC for 2 hours is insufficient for complete dolomite digestion.

The bulk-rock results are close to the calculated average value for the punctual micro-sampling results: (1) Bulk - $\delta^{13}C$ -1.69 (‰V-PDB) with 0.1σ and $\delta^{18}O$ -0.26 (‰V-PDB) with 0.05 σ; (2) Micro-sampling average ($\bar{x}$ δ) - $\delta^{13}C$ -2.13 (‰V-PDB) with 0.15σ and $\delta^{18}O$ -1.00 (‰V-PDB) with 0.1σ; Notably, most of the values obtained for carbon isotope fall into a trend from the calculated average value and the standard deviation average ($\bar{x}$ σ * 3). However, the oxygen isotope shows greater variability, with most results outside a general trend (Fig. 16).

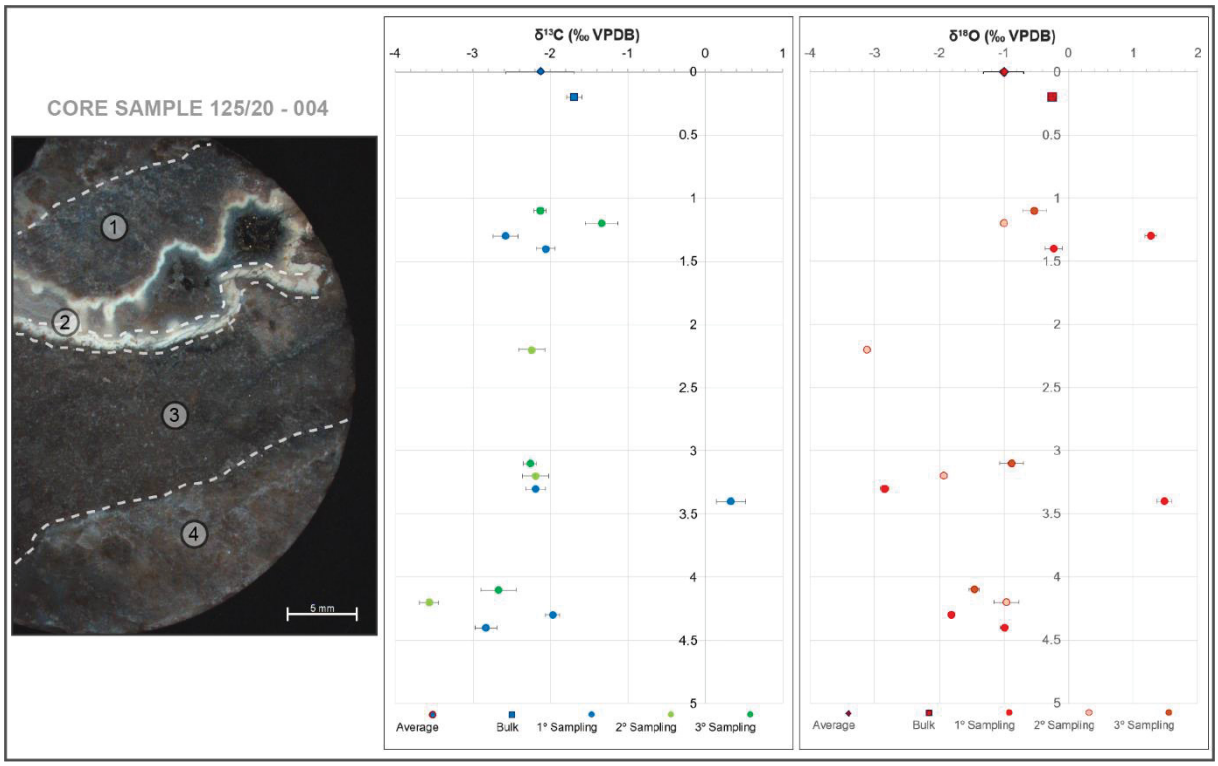

Figure 16: Carbon and oxygen stable isotope ratios from calcite and Low-Mg calcite, with the main trend expected from the estimated average ($\bar{x}$ δ) delimited by the standard deviation ($\bar{x}$ σ * 3).

4.2 CORE SAMPLE DESCRIPTION (CODE 125/20-189 - DEPTH 5030.17m)

The sample 125/20-189 displays a silica layer/nodule of 20 cm width from 5030.17m depth in Fragata well (Fig. 17A). The sample is partially brecciated by micro faults. However, the brecciation does not compromise the mudstones, only affecting the silica layer (Fig. 17B). The faults and fractures, as well as vuggy and channel porosities, are filled by late spatic calcite and traces of barite and pyrite. The core sample selected consists of a chert layer with vuggy porosity cemented by chalcedony and in contact with the laminated mudstone framework (Fig. 17C).

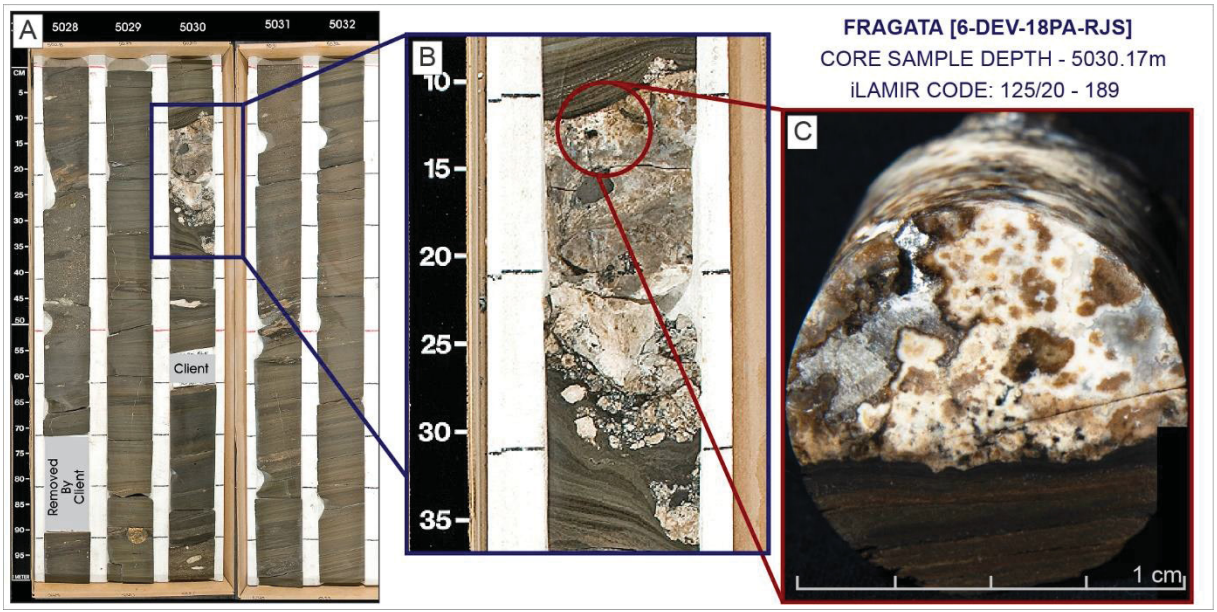

Figure 17: A. Fragata well samples from 5028 to 5032m depths; B. Silica layer of 25cm width, at 5030.10 to 5030.35m depth, partially brecciated; C. Highlight of sample 125/20-189, composed by a laminated mudstone in contact with a chert lens cemented by calcedony, in addition, is notable spathic calcite cementing remaining vuggy porosity.

4.2.1 Petrographic microfacies

Laminated mudstones

The laminated mudstone microfacies occur in contact with a silica lens (Fig. 18A) and comprise mostly mud to silt size (2 – 60 µm) calcite and dolomite/ankerite crystals marked by a laminated structure, in addition to spheroids of calcite (100 µm) scattered in the framework.

The interparticle porosity is filled with amorphous organic matter, and granular microcrystalline silica occurs in small proportions (<30%). In addition, cubic pyrite appears scattered through the mudstone (Fig. 18B, C).

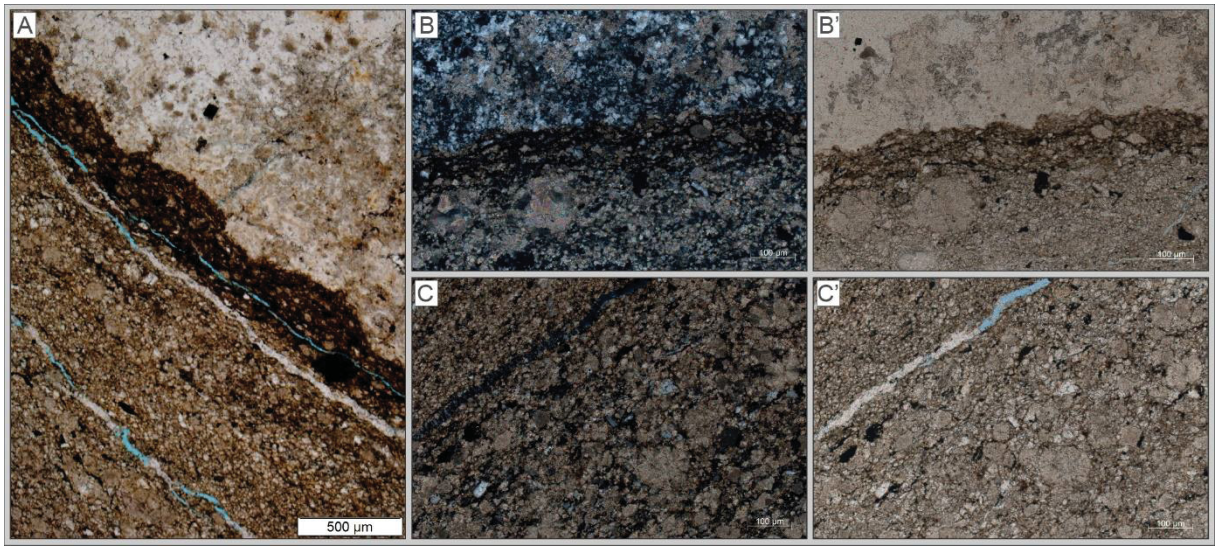

Figure 18: Laminated mudstone under the optical microscope. A. Laminated mudstone in contact with silica lens, and amorphous organic matter (carbon) filling interparticle porosity, traces of cubic pyrite dispersed; B. Contact between mudstone and silica, with a highlight for spheroidal calcite (100 µm) in the mudstone framework; C. Mudstone framework with spheroidal calcite, granular microcrystalline silica, and traces of pyrite.

Chert: Granular crypto/microcrystalline silica

The silica layer in contact with the laminated mudstone (Fig. 19A) comprises granular cryptocrystalline to microcrystalline silica crystals (< 4 to10 µm), commonly denominated *Chert* (Fig. 19B). Dolomite crystals measuring (50 – 100 µm) occurs floating/dispersed in the chert matrix with partial replacement by silica (Fig. 19C). Calcite does not appear in this silica layer. In complement, cubic halite crystals (5 – 10 µm) also are distributed in the silica matrix (Fig. 19D), forming agglomerates (100 – 200 µm).

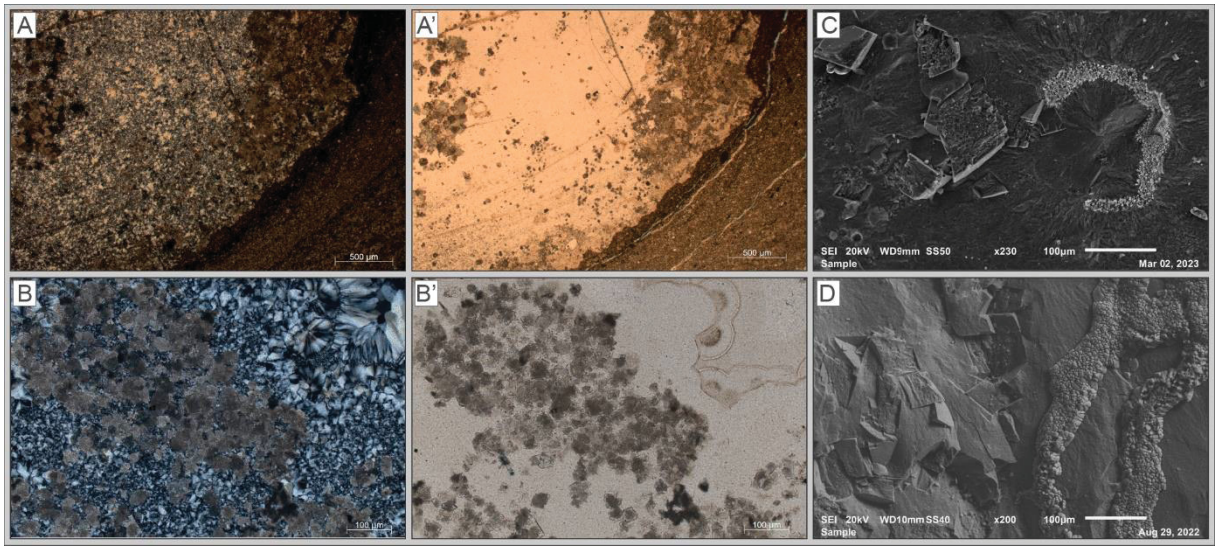

Figure 19: Granular crypto/microcrystalline silica (Chert) under an optical microscope and SEM. A. Contact between chert and laminated mudstone. B. Chert with dolomite crystals; C. Contact between chert and chalcedony with dolomite partially replaced by silica; D. Chert with dolomite and halite.

Chalcedony: Fibrous crypto/microcrystalline silica

The fibrous cryptocrystalline silica, named chalcedony, occurs in cementing vuggy and channel porosities. The white color and spherical form of chalcedony characterize the samples (Fig. 20A). Under thin sections and SEM analysis, two patterns of spheroids are notable: (1) The first spheroid pattern 200 µm in radius cements the chert with a continuous growth pattern dependent on the chert wall. The spheroid nucleus is surrounded by palisade cement (dog teeth cement) (Fig. 20B); (2) The second spheroids pattern is marked by spheres around 50-100 µm in radius, forming clusters of botryoids (< 4 µm). They differ from the first pattern mainly by the absence of the palisade cement (Fig. 20C);

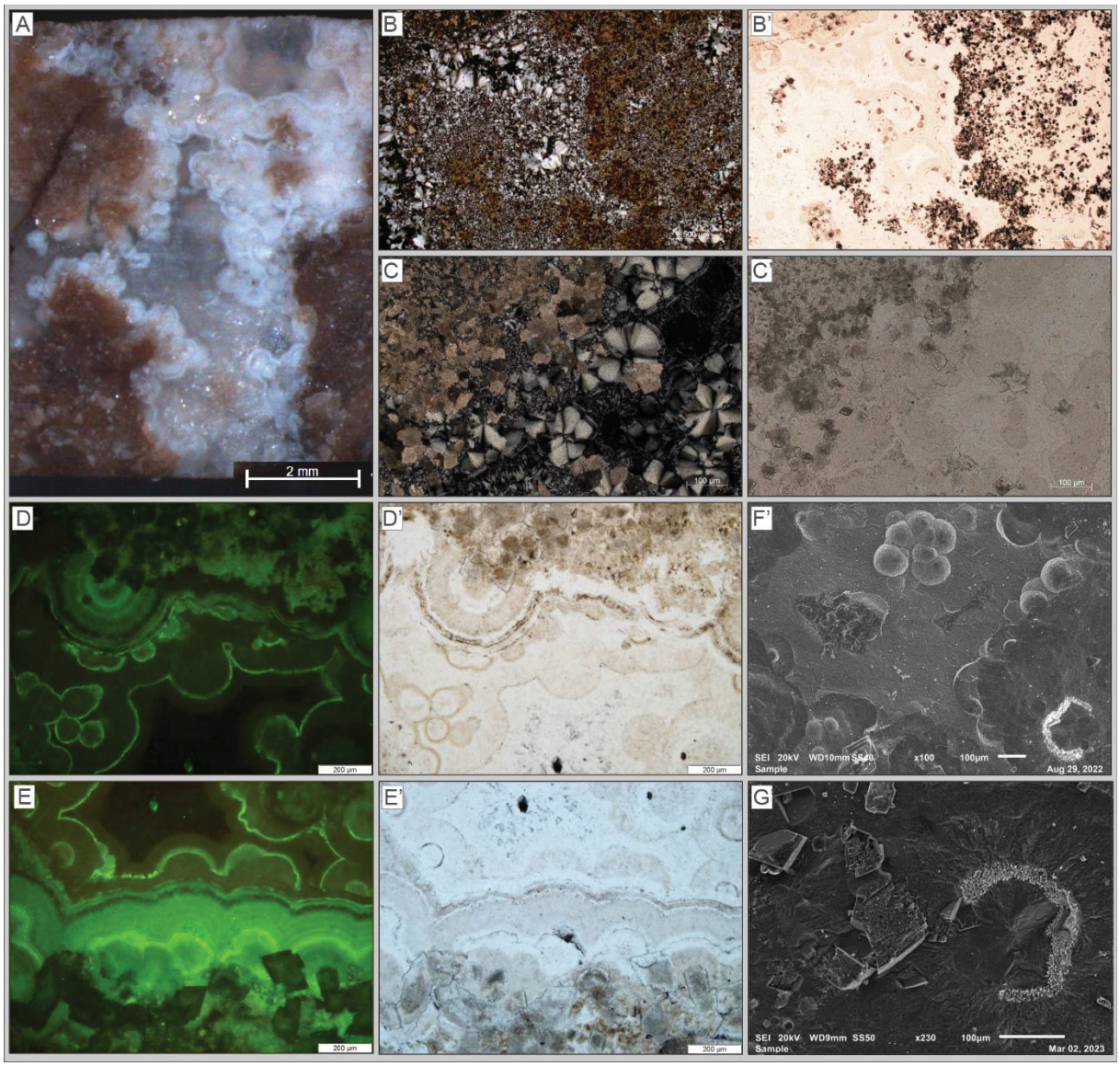

Figure 20: Fibrous cryptocrystalline silica: Chalcedony, two patterns of chalcedony are distinguished under SEM, optical, and UV microscope. A. Chalcedony (white) cement vuggy and channel porosity in chert; B. Chalcedony spheroids surrounded by a palisade (200 µm radius); C. Cluster of spheroids without palisade (50-100 µm radius); D. E. UV image allowing distinction of chalcedony, chert, drusiform quartz, and halite coating evidenced by high UV response; F. Clusters of spheroids/botryoids; G. Halite coating in hemispheroid.

These changes in the texture allow the identification of two different stages for the fibrous cryptocrystalline silica precipitation, clearly observed under UV fluorescence light (Fig. 20D, E). Under SEM, halite crystallite coats the spheroids/botryoids (Fig. 20F). Most halite crystallites are around 1-10 µm, but larger ones occur, especially the crystallites between the spheroids and the palisade that reach 10-50 µm (Fig. 20G). Dolomite rhomb and saddle crystals of about 50 to 100 µm occur scattered at the first pattern of spheroidal chalcedony.

Mega-Quartz: Granular macrocrystalline silica

The macrocrystalline silica (Mega-quartz) occurs, filling the remnant porosity after the chalcedony cementation (Fig. 21A). The crystal size varies from 100 µm to 200 µm (fine crystalline). When space is available, the quartz crystals grow as euhedral drusiform crystals with the normal and pseudohexagonal habit, while anhedral crystals show rectilinear contact.

After all the silicification phases, amorphous organic matter (bitumen) fills the remaining porosity with traces of barite (Fig. 21B). Spathic calcite is also observed as a late cementation phase, filling vugular and channel porosities after the silicification (Fig. 21C).

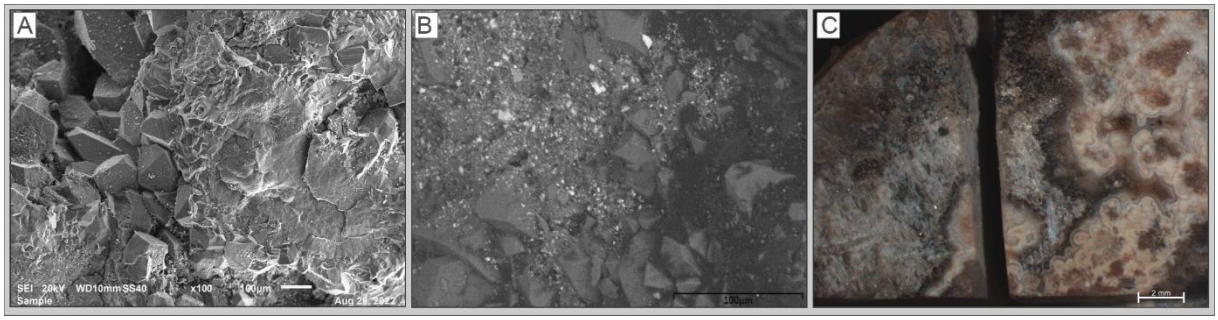

Figure 21: Macrocrystalline silica: Mega-Quartz under SEM and Spathic calcite under a stereomicroscope. A Mega-quartz completing the silicification sequence; B. Mega-quartz and remaining porosity filled by amorphous organic matter and traces of barite; C. Spathic calcite filling remaining porosity;

4.2.2 Chemical composition

The main compounds of the laminated mudstone lithofacies in contact with the silica layer, given in major oxides, are CaO, MgO, SiO_2, Al_2O_3, Fe_2O_3, Na_2O, K_2O, TiO_2, MnO, and P_2O_5.

Major oxides detected in more than 1wt% were (Fig. 22):

- SiO_2 (62.47%) in the form of quartz α.
- CaO (11.23%) occurs as calcite crystals in the laminated mudstone.
- MgO (4.79%) comprehends dolomite crystals predominantly associated with chert, forming solid solutions between dolomite and ankerite through Fe_2O_3 (1.48%).

- Al_2O_3 (1.74%) occurs as in the mudstone. However, XRD does not show clay minerals or aluminosilicate.

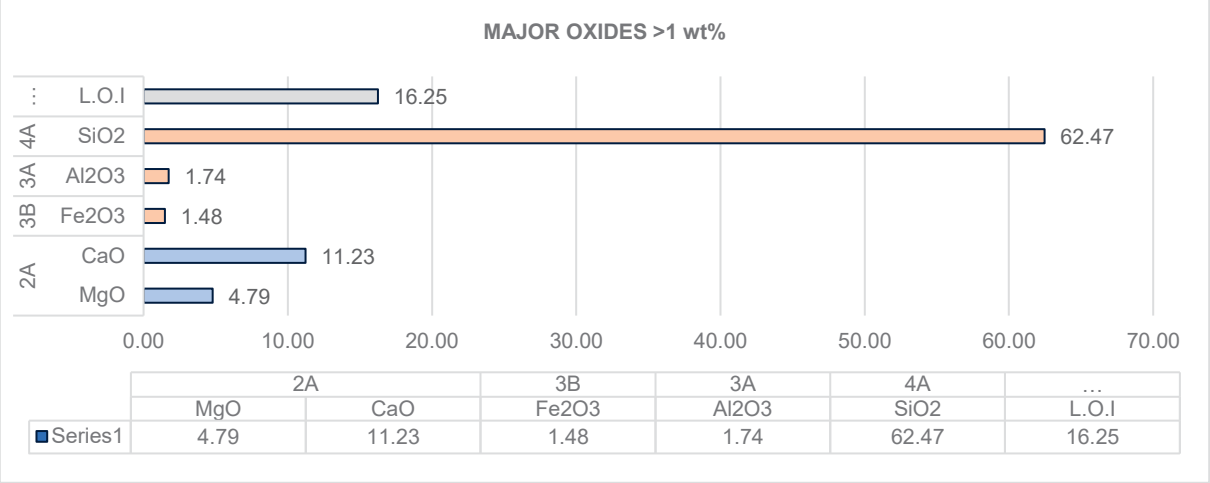

Figure 22: Bulk sample composition regarding Major Oxides detected in more than 1 wt %.

Major oxides detected in less than 1wt% were (Fig. 23):

- Na_2O (0.67%) commonly occurs associated with Cl forming halite.
- K2O (0.32%), with no clear occurrence in the mudstone.
- TiO2 (0.14%) in association with vuggy porosity.
- P_2O_5 (0.14%) occurs in the laminated mudstone.
- Mn (0.04%) is associated with dolomite/ankerite, possibly substituting Magnesium.

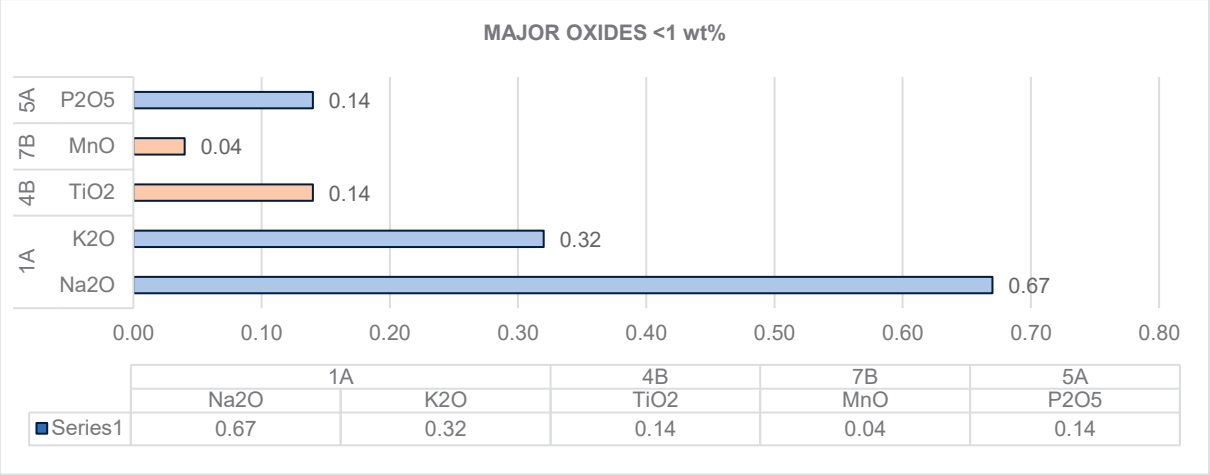

Figure 23: Bulk sample composition regarding Major Oxides detected in less than 1 wt%.

Trace elements detected in more than 100 ppm (Fig. 24) were Sulfur (S - 3947 ppm) commonly occurs associated with Barium (Ba – 242 ppm) forming barite traces and iron (Fe) forming pyrite. In addition, Strontium (Sr – 600 ppm) occurs in substitution for Calcium.

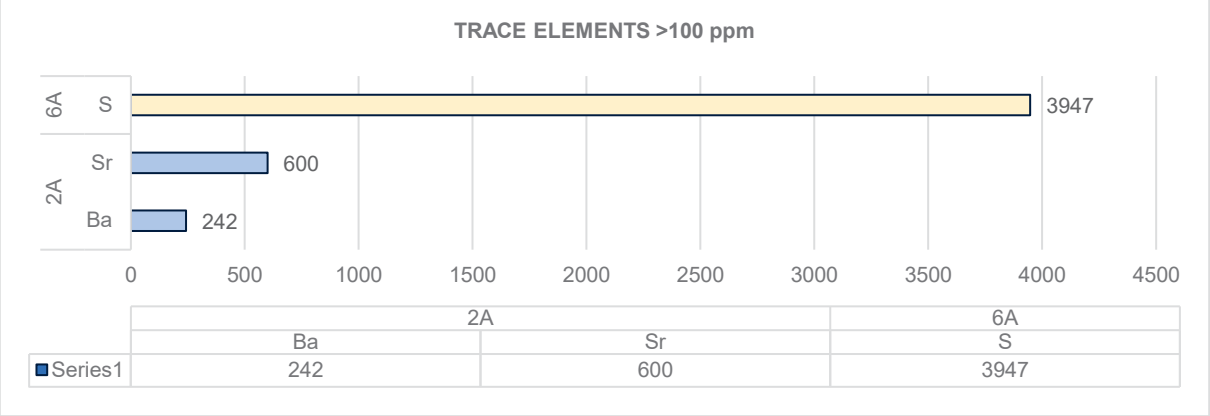

Figure 24: Bulk sample composition regarding Trace Elements detected over 100ppm.

From trace elements detected in less than 100 ppm (Fig. 25):

- Rubidium (Rb - 7 ppm) and Zinc (Zn - <5 ppm) are related to silica.

Trace elements without a clear sample disposition were: Yttrium (Y - <5 ppm), Zirconium (Zr – 31 ppm), Vanadium (V – 60 ppm), Niobium (Nb - 8 ppm), Copper (Cu – 16 ppm), Lead (Pb – 18 ppm), and Rare Earth elements were Lanthanum (La - <41 ppm), Cerium (Ce - <55 ppm), and Neodymium (<52 ppm).

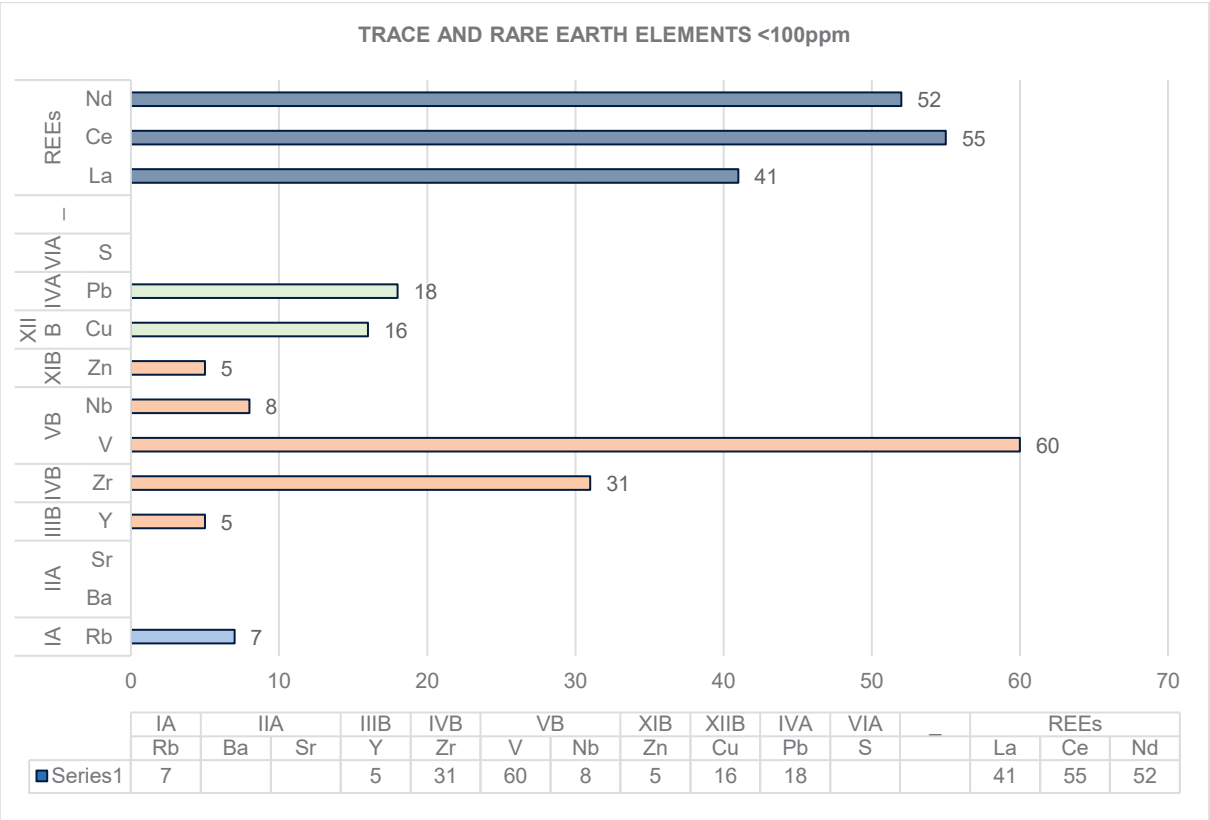

Figure 25: Bulk sample composition regarding Trace Elements detected in less than 100ppm.

A semi-quantitative chemical distribution obtained through X-Ray Spectrometer complements mineralogical results, allowing the observation of trace and rare earth elements spectra associated with the main mineralogical phases and structures as fractures, channels, or vuggy porosities (Fig. 26). The main mineralogical component for the carbonate phase is Dolomite, evidenced by Calcium (Ca), Magnesium (Mg), and Iron (Fe) spectra, with Manganese (Mn) and Strontium (Sr) as trace elements in substitution phases. Potassium (K) does not relate to the mineral assemblages in this sample. Instead, silica occurs, filling porosities and partially replacing carbonate crystals. The chert lens phase occurs in association with Aluminum (Al) and trace elements Bromine (Br), Palladium (Pd), Rhodium (Rh), Rubidium (Rb), Rhenium (Re), and Zirconium (Zr). In addition, the chalcedony strongly associates Sodium (Na) and Chlorine (Cl). Trace elements related to fracture, channel, and vuggy porosities are Barium (Ba), Titanium (Ti), and Sulfur (S), while Zirconium (Zr) also does not show a clear relation.

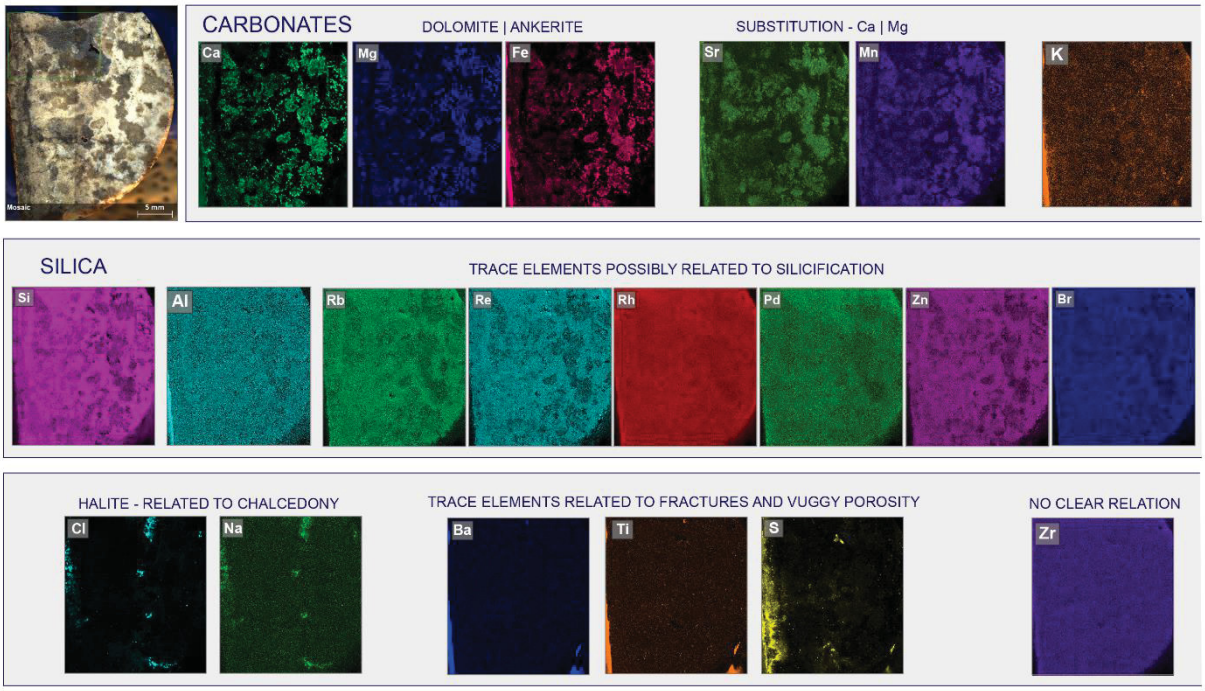

Figure 26: Elements distribution obtained through X-Ray Spectrometer. The elements' combination is according to mineralogical phases and sample structures.

In addition, Bromine (Br), Palladium (Pd), Rhodium (Rh), and Rhenium (Re) were detected by X-Ray Fluorescence Spectrometer Bruker (Caltech), showing association with silica. However, these elements do not appear at XRF through bulk rocks analyzed at the Panalytical.

4.2.3 Mineralogical composition

The sample semi-quantitative mineralogical composition results in 65,7% alpha quartz, 11,1% calcite, 16,2% ankerite, and 7,1% dolomite. The microsampling XRD analysis shows dolomite/ankerite and the absence of calcite in the mudstone framework and silica lens. The Magnesium content (MgO - 4,79 wt%) normalized to moles (30.76 mol%) indicates disordered dolomite (Calcium rich dolomite/proto-dolomite). The Iron content (Fe2O3 – 1.48%) normalized to mol (8.19 mol%) suggests the possibility of a solid solution with Ca-dolomite and Ankerite. In addition, the content of calcite from this sample represents a late/tardy phase of calcite cementation, clearly observed in the petrographic studies (Fig. 27).

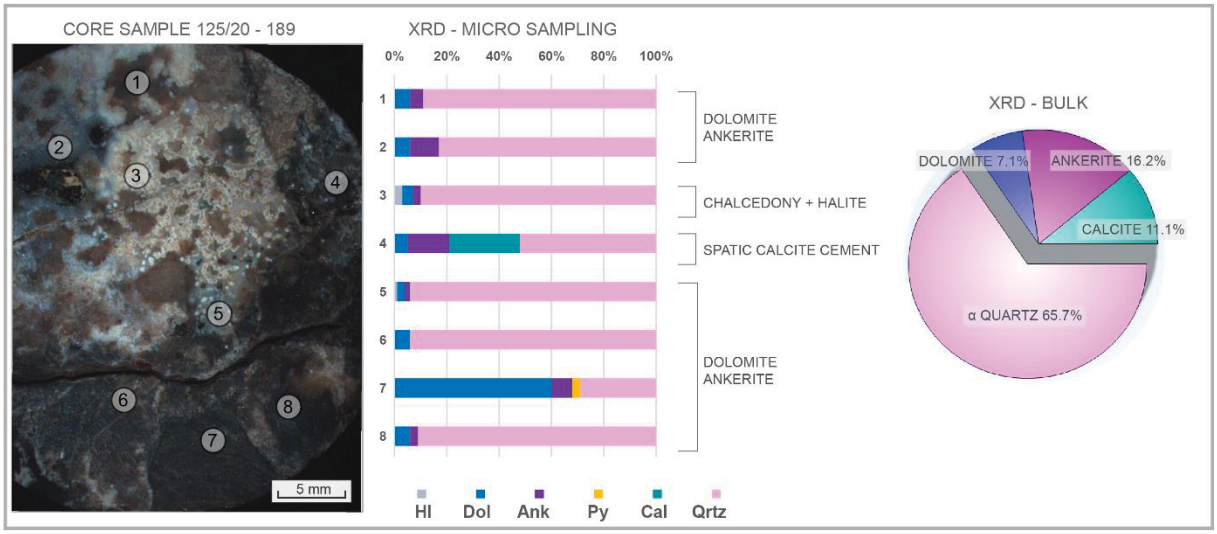

Figure 27: XRD semi-quantitative mineralogical composition for micro-sampling according to mineralogical variation.

4.2.4 Carbon and Oxygen stable isotopes

As estimated through XRD and XRF, the carbon and oxygen stable isotope signatures represent dolomite crystals, possibly in a solid solution with ankerite. In this case, calcite samples occur as a late-cementation phase in vuggy porosity. The main trend is delimited by the standard deviation (σ) multiplied by three ($\bar{x}$ σ * 3). At last, three punctual samples obtained for each microfacies.

The bulk-rock results are close to the calculated average value for the punctual micro-sampling results: (1) Bulk - $\delta^{13}C$ 3.44 (‰V-PDB) with σ and $\delta^{18}O$ 2.70 (‰V-PDB) with σ; (2) Micro-sampling average ($\bar{x}$ δ) for dolomite crystals - $\delta^{13}C$ 2.67 (‰V-PDB) with 0.11σ and $\delta^{18}O$ 1.56 (‰V-PDB) with 0.08σ; (3) In addition calcite cementation average signature without dolomite crystals consists in - $\delta^{13}C$ 0.56 (‰V-PDB) with 0.11σ and $\delta^{18}O$ -0.11(‰V-PDB) with 0.04σ; For this sample, most of the carbon isotope signature for dolomite crystals occur

inside a trend from the calculated average value and the standard deviation average ($\bar{x}\ \sigma * 3$). However, the oxygen isotope shows greater variability, with most results outside a general trend (Fig. 28).

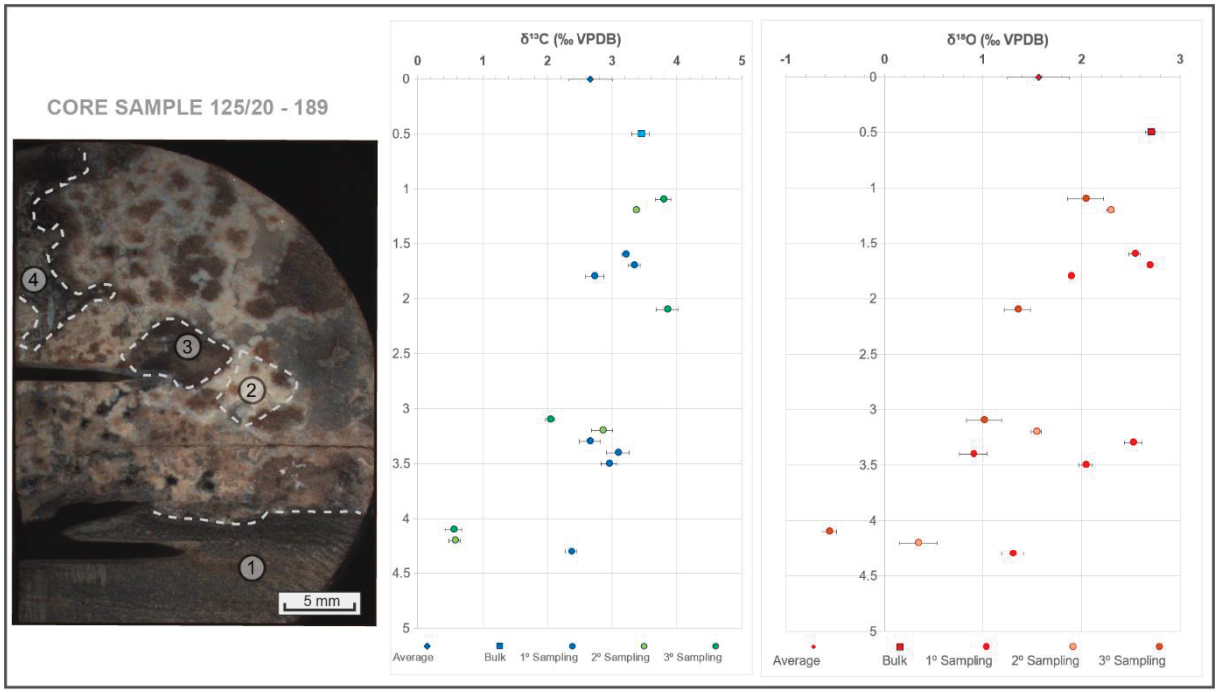

Figure 28: Carbon and oxygen stable isotope ratios from dolomite/ankerite crystals, with the main trend expected from the estimated average ($\bar{x}\ \delta$) delimited by the standard deviation ($\bar{x}\ \sigma * 3$). Two results outside the main tendency represent a late calcite cementation phase.

4.3 CORE SAMPLE DESCRIPTION (CODE 125/20-195 – DEPTH 5027.73m)

The sample 125/20-195 represents the laminated mudstone with small chert layers (Fig. 29A). The core sample is located at 5027.73m in Fragata well (Fig. 29B) and consists of a laminated calcite mudstone with chert layers and stylolites parallel to the lamination (Fig. 29C).

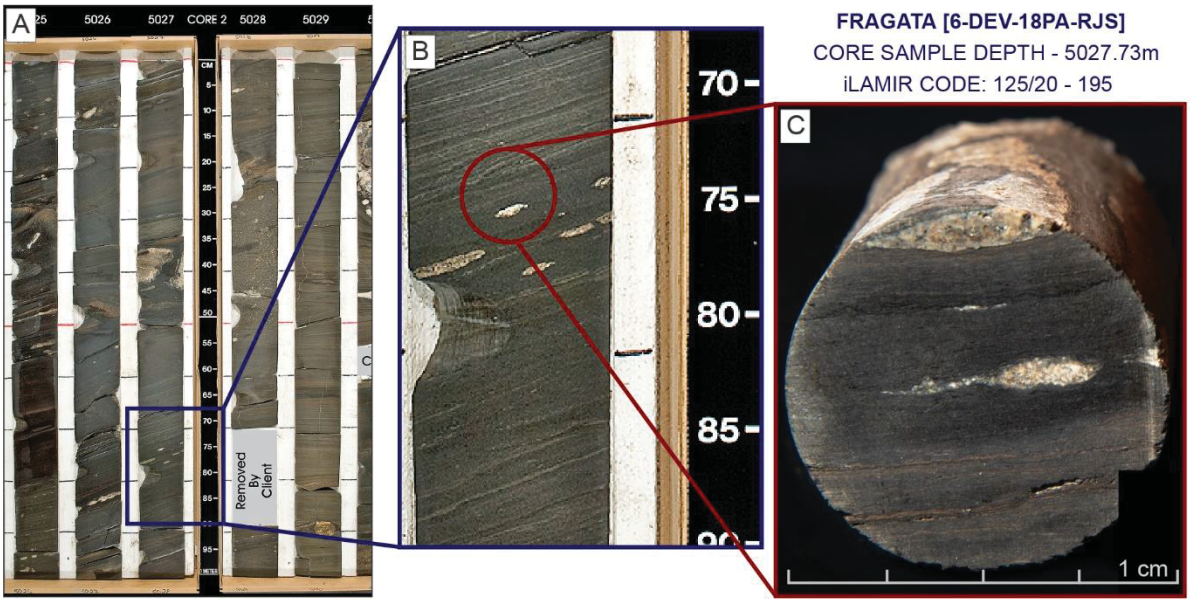

Figure 29: A. Fragata well samples from 5025 to 5029m depths; B. Silica nodules of about 1cm in width, at depth 5027.73 to 5027.80; C. Sample 125/20-195, composed by a laminated mudstone with silica lens/nodules and stylolite parallel to lamination.

4.3.1 Petrographic microfacies

Laminated mudstones

The laminated mudstone (Fig. 30A) consists mostly of equigranular mud/silt-size calcite crystals, measuring around 5-20 µm, partially dolomitized (Fig. 30B) in tangential to sutured contact. Common structures in the mudstone framework are stylolites, in a columnar style with large amplitude, single to swarms (Fig. 30C), with solid residues of aluminum, sulfur, and carbon (Fig. 30D). Some portions are marked by fenestral porosity (Fig. 30E) filled with sulfates (gypsum and barite). The interparticle framework porosity, estimated at 15,4% through µCT, is rich in amorphous organic matter (carbon) (Fig. 30F).

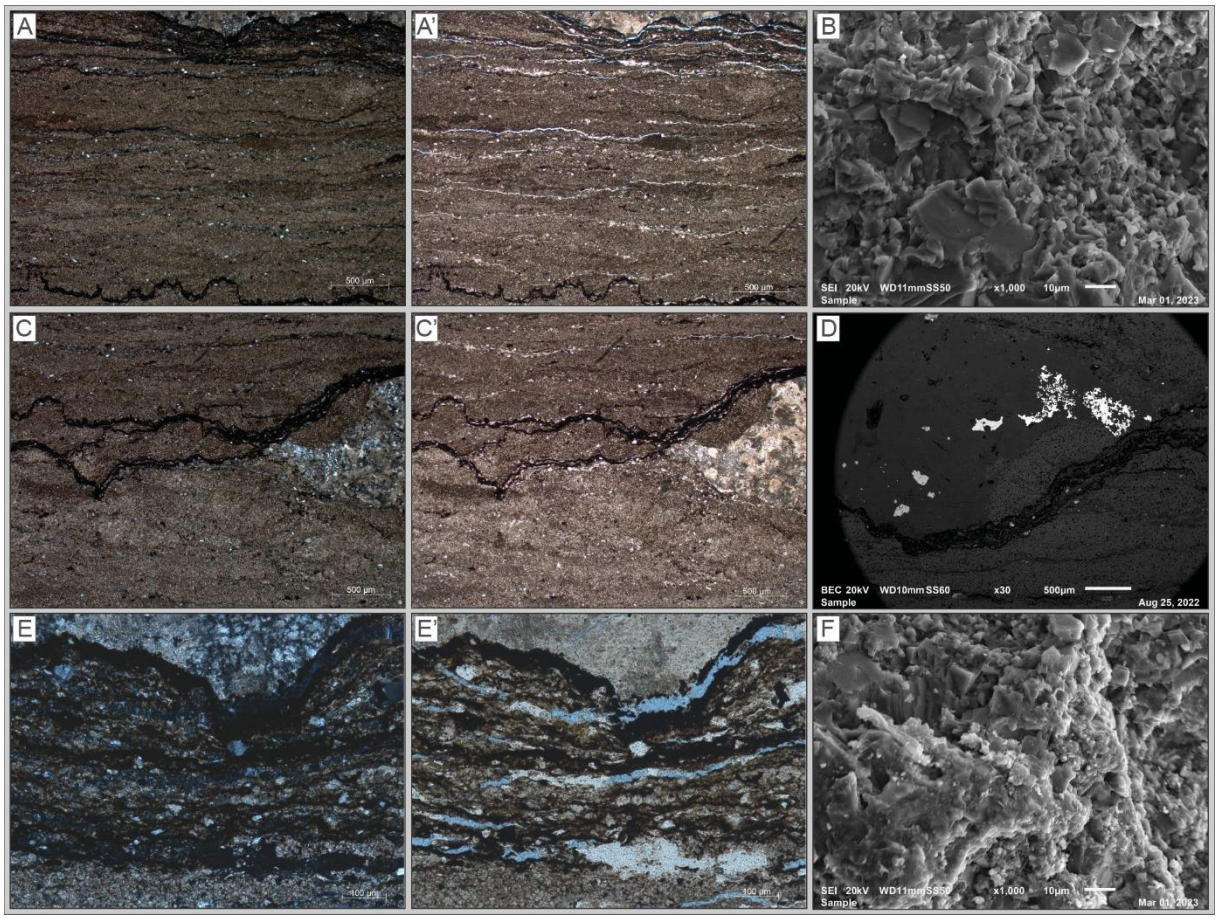

Figure 30: Laminated mudstone under an optical microscope and SEM. A. Laminated mudstone; B. Mud/silt size calcite crystals; C. Stylolite in the laminated mudstone; D. Backscattering image of laminated mudstone, with silica lens filled by barite and stylolite filled solid residues mainly composed by aluminum, sulfur, and carbon; E. Fenestral porosity filled by sulfates as gypsum and barite; F. Mud/silt size calcite crystals associated with organic carbon/amorphous organic matter.

Chert: Granular crypto/microcrystalline silica

The chert layer (<5 mm) occurs parallel to the lamination, predominantly composed of α-quartz with a granular crypto/microcrystalline (< 4 to10 µm) texture, and calcite partially replaced by silica (Fig. 31A). Dolomite (<10 µm) appears as rhomb crystals scattered in the silica matrix, with a floating texture. In addition, cubic pyrite crystals of 50 to 150 µm occur distributed (Fig. 31B). At the same time, barite (stoichiometric) fills vuggy porosity (Fig. 31C) with crystals up to 250 µm (Fig. 31D). Sr-Barite also was detected. Amorphous organic matter occurs in vuggy porosities in the silica layer. Halite crystallites observed (Fig. 31E) and, under SEM, form aggregates and vary in size from 1 µm to 50 µm (Fig. 31F).

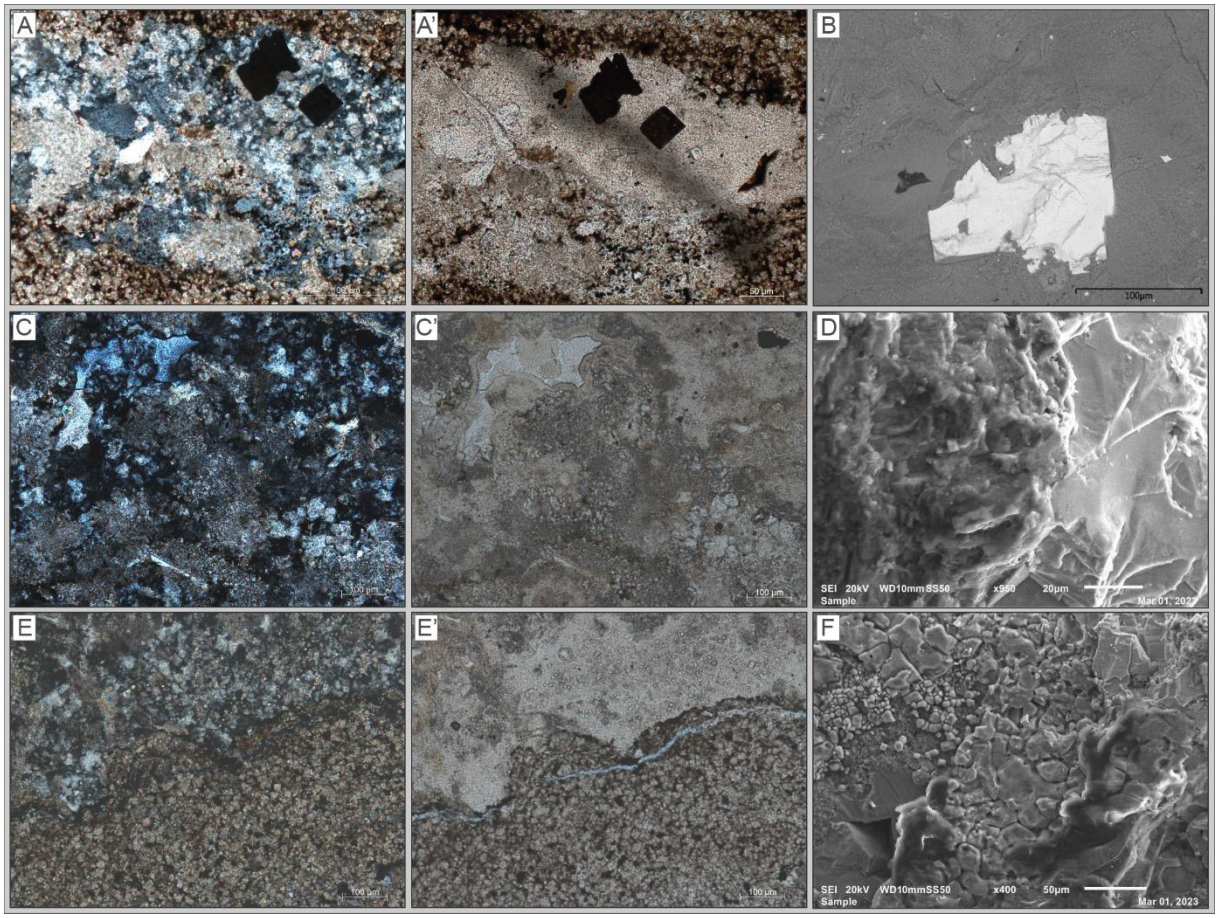

Figure 31: Granular crypto/microcrystalline silica (Chert), under an optical microscope and SEM. A. Silica lens with replaced calcite crystals, cubic pyrite, and organic matter filling interparticle porosity; B. Chert lens with a cubic pyrite and low-Mg calcite replaced by silica; C. Barite filling vuggy porosity; D. Barite crystal; E. Focus for halite crystallites in silica lens evidenced by high relief; F. Halite crystallites forming clusters;

4.3.2 Chemical composition

Through bulk rock analysis, the main composition of the laminated mudstones given in weight percent is:

Major oxides detected in more than 1wt% were (Fig. 32):

- CaO (41.24%), which forms the calcite crystals framework.
- SiO_2 (11.82%) developing silica layers parallel to lamination.
- MgO (1.84%) occurs as Mg-calcite and dolomite crystals.
- Al_2O_3 (2.02%) appears as residual solids in stylolites.

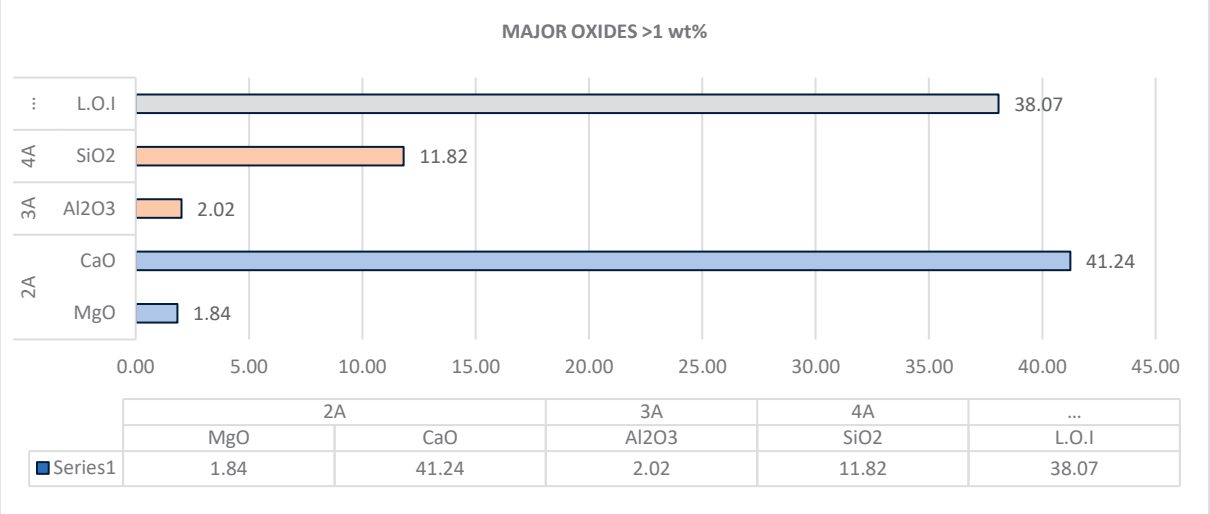

Figure 32: Bulk sample composition regarding Major Oxides detected in more than 1 wt %.

Major oxides detected in less than 1wt% were (Fig. 33):

- Fe_2O_3 (0.94%) is not related to dolomite/ankerite for this sample. However, it relates to sulfur forming cubic pyrite.
- TiO_2 (0.17%) occurrence also is associated with the stylolites.
- Na_2O (0.47%) forms halite in association with Cl.
- K_2O (0.57%) is associated with Al_2O_3 (2.02%). However, XRD does not show aluminum silicates and clay minerals.

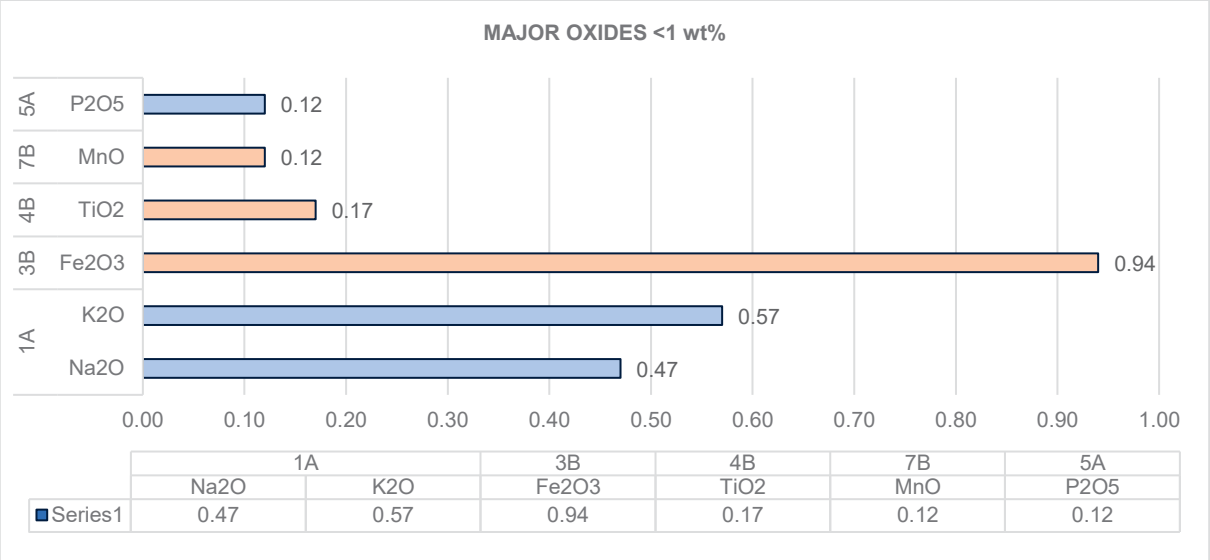

Figure 33: Bulk sample composition regarding Major Oxides detected in less than 1 wt %.

A significant amount of trace elements also was detected, with a highlight for the occurrence of more than 100 ppm (Fig. 34):

- Sulfur (S – 4228 ppm) is associated with iron (Fe) forming octahedron pyrite.

- Barium (Ba – 1045 ppm) compound barite.
- Strontium (Sr – 1757 ppm) occurs associated with calcite in substitution with Calcium.

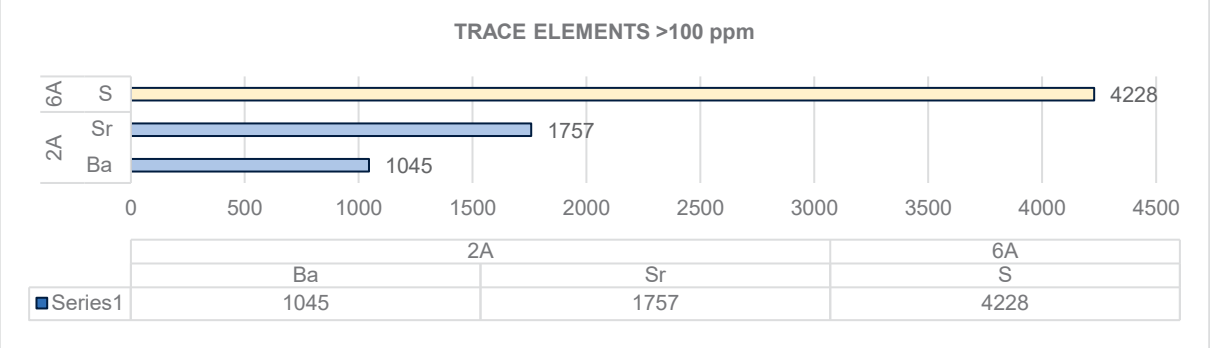

Figure 34: Bulk sample composition regarding Trace Elements detected over 100ppm.

Trace elements detected in less than 100ppm are (Fig. 35):

- Rubidium (Rb - <4 ppm) and Zinc (Zn – 6 ppm) show a relation with silica.
- Zirconium (Zr – 39 ppm), Vanadium (V – 60 ppm) show a correlation with TiO_2 associated with stylolites.

Trace elements without a clear sample disposition are: Yttrium (Y - <4 ppm), Niobium (Nb - <3 ppm), Copper (Cu – 15 ppm), Lead (Pb – 12 ppm), and Rare Earth elements detected were Cerium (Ce - <55 ppm), Lanthanum (La - <40 ppm), Neodymium (<52 ppm).

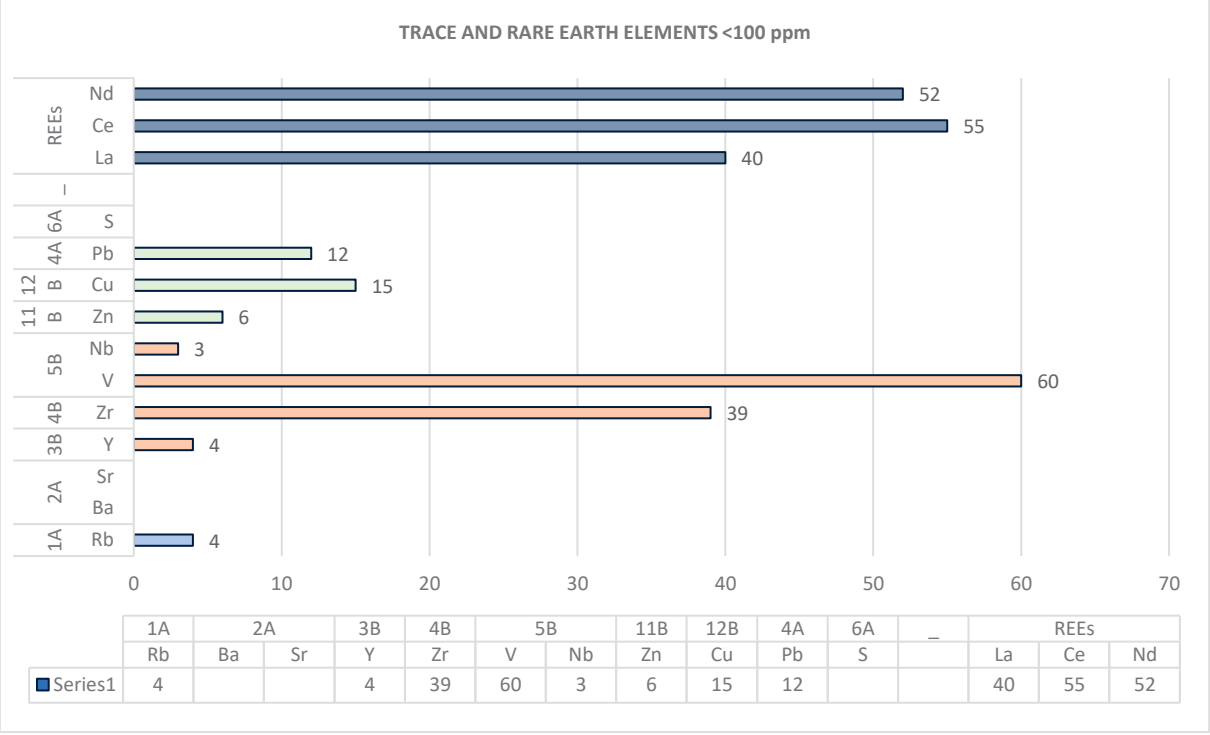

Figure 35: Bulk-rock composition regarding Trace and Rare Earth Elements detected in less than 100ppm.

As a complement to the mineralogical and chemistry data, the semi-quantitative chemistry element distribution associated with the main mineralogical phases and structures (Fig. 36) displays: (1) The main mineralogical component for the carbonates phase (Calcite, Mg-Calcite, and dolomite) is evidenced through Calcium (Ca) spectra, with Strontium (Sr) as trace elements in the substitution phase for calcite. In contrast, Magnesium (Mg) and Manganese (Mn) are in dolomite crystals in substitution phases. Potassium (K) is associated with Aluminum (Al) intercalated with calcite or filling stylolite as solid residues for this sample. Chlorine (Cl) also occurs parallel to the lamination; (2) The silica forms a lens parallel to the lamination in association with trace elements such as Palladium (Pd), Rhodium (Rh), Rubidium (Rb), Rhenium (Re), and Zinc (Zn). Elements related to fenestral porosities with mineral formation are Barium (Ba) and Iron (Fe), partially associated with Sulfur (S), forming Barite and Pyrite. Trace elements such as Titanium (Ti), Vanadium (V), Zirconium (Zr), and the remaining Barium (Ba) and Iron (Fe) are possibly related to the solid residual phase (stylolites) or the fenestral porosity.

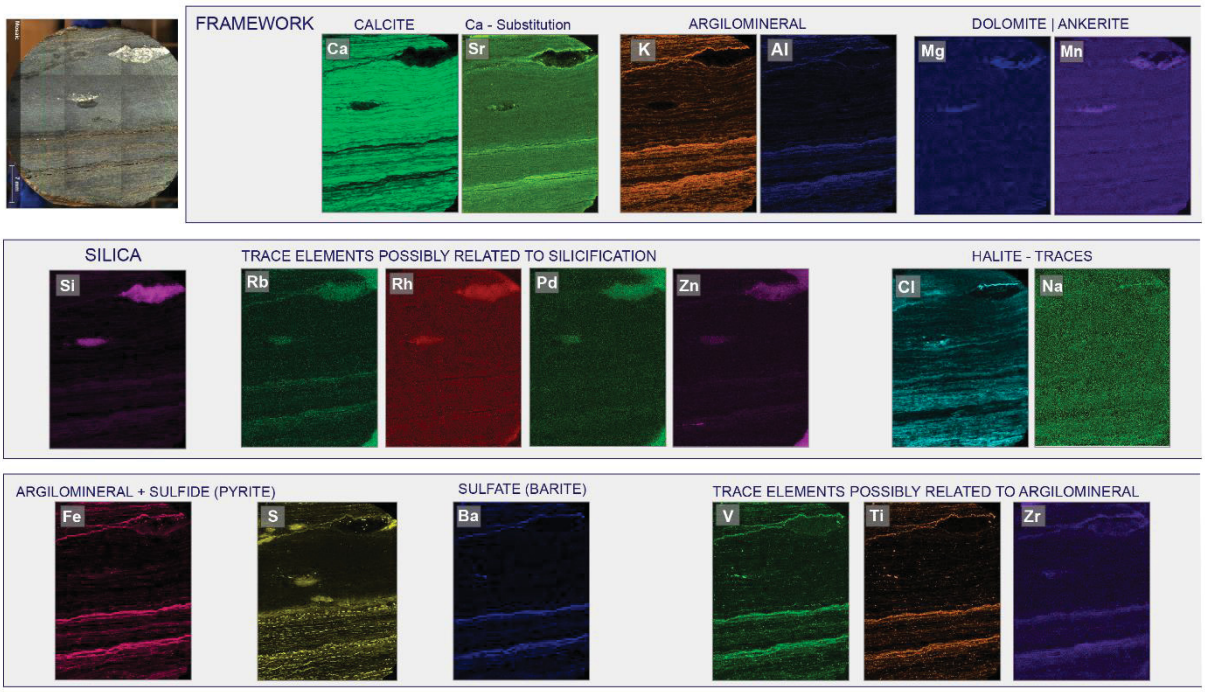

Figure 36: Elements distribution obtained through X-Ray Spectrometer. The elements' combination is according to mineralogical phases and sample structures.

In addition, Palladium (Pd) and Rhodium (Rh) were detected by X-Ray Fluorescence Spectrometer Bruker (Caltech), showing an association with silica. However, these elements do not appear at XRF through bulk rocks analyzed at the Panalytical.

4.3.3 Mineralogical composition

The mineralogical composition resulted in 59% calcite, 21% alpha quartz, 10% low magnesium calcite, and 10% calcium dolomite. The mineralogical composition mainly consists of calcite, with the silica lens parallel to the mudstone lamination. The XRF Magnesium content (MgO 1.84 wt%) normalized to moles (3.63 mol%) indicate Low-Magnesium calcite presence in the framework (Fig. 37).

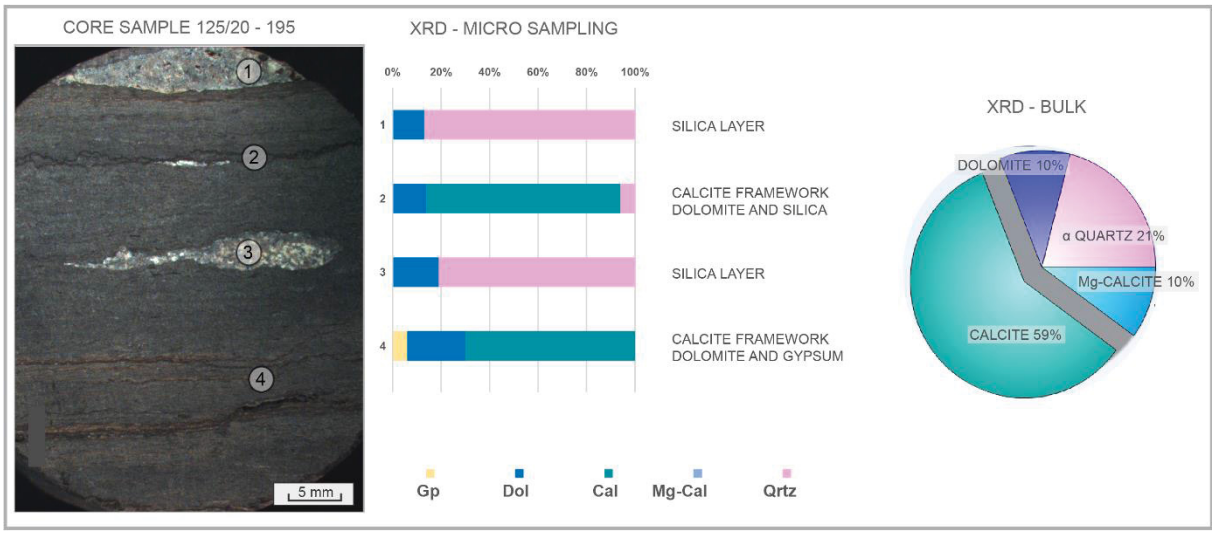

Figure 37: XRD semi-quantitative mineralogical composition for micro-sampling according to mineralogical variation.

4.3.4 Carbon and Oxygen stable isotopes

Three punctual samples were obtained for each microfacies to identify the isotopic signature microscale variation and the general tendency of the results according to the average value, with the main trend delimited by the standard deviation (σ) multiplied by three ($\bar{x}$ σ * 3). The results obtained for homogenized sampling (Bulk) are close to the calculated average value for the punctual micro-sampling results: (1) Bulk - $\delta^{13}C$ 2.35 (‰V-PDB) with 0.15σ and $\delta^{18}O$ 0.48(‰V-PDB) with 0.09σ; (2) Micro-sampling average ($\bar{x}$ δ) for both dolomite and calcite crystals results in - $\delta^{13}C$ 2.68 (‰V-PDB) with 0.10σ and $\delta^{18}O$ 0.77 (‰V-PDB) with 0.09σ; For this sample both carbon and oxygen isotope signature for calcite and dolomite crystals occur inside a trend from the calculated average value and the standard deviation average ($\bar{x}$ σ * 3) (Fig. 38).

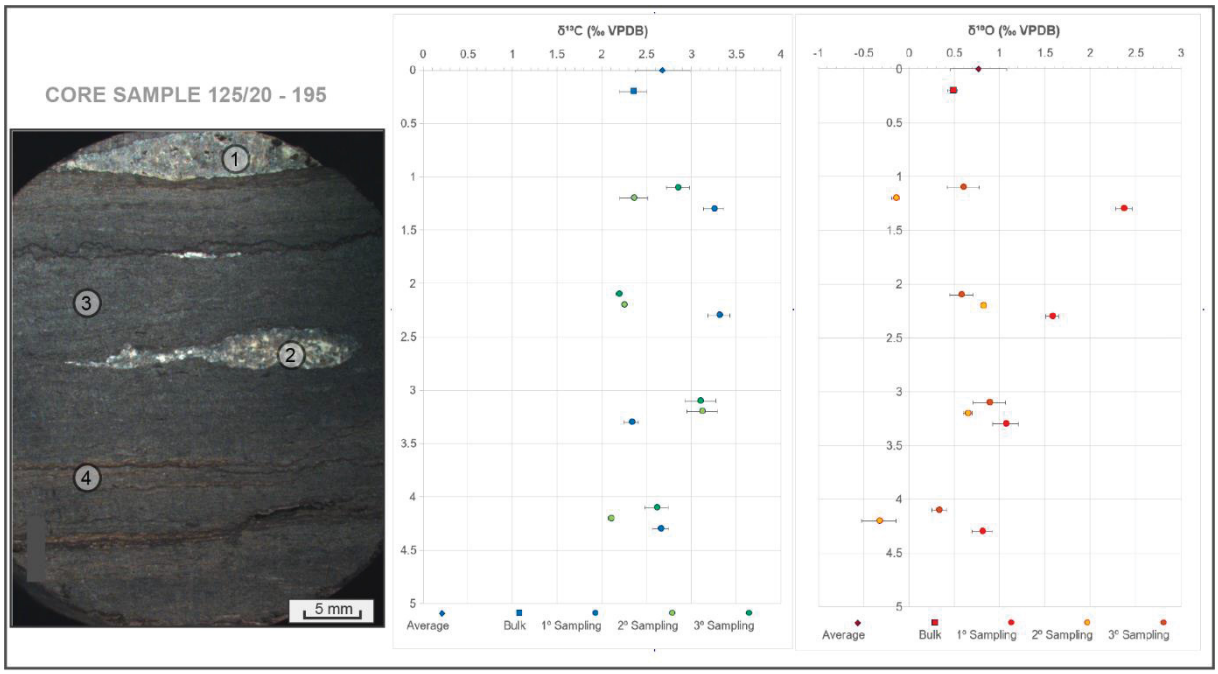

Figure 38: Carbon and oxygen stable isotope ratios from calcite and low-Mg calcite crystals, with the main trend expected from the estimated average ($\bar{x}$ δ) delimited by the standard deviation ($\bar{x}$ σ * 3).

4.5 SUMMARIZED DATA TABLES (XRD, XRF, C&O STABLE ISOTOPES)

Mineralogical compositions obtained through an X-ray diffractometer are summarized in Table 1, where the homogenized bulk rock analysis identifies α-Quartz (Silica Low-temperature polymorph), Calcite, Mg-calcite, Dolomite, and Ankerite.

Table 1: X-ray diffractometer (XRD) bulk composition.

Studied samples mineralogical composition summary			
Sample	**Depth**	**Microfacies**	**Main mineralogical composition (XRD)**
125/20 - 195	5027.73	Laminated mudstone with chert lens	Calcite (59%), Qrtz α (21%), Dolomite (10%), Mg-calcite (10%)
Punctual sampling	01		Qrtz α (87%), Dol (13%)
	02		Cal (80%), Dol (14%), Qrtz α (6%),
	03		Qrtz α (81%), Dol (19%)
	04		Cal (70%), Dol (24%), Gy (6%)
125/20 - 189	5030.17	Laminated mudstone, with chert lens	Quartz α (66,7%), Dolomite (17,1%), Ankerite (16,2%), Calcite (11,1%)
Punctual sampling	01		Qrtz α (89,1%), Dol (5,9%), Ank (5%)
	02		Qrtz α (83%), Ank (11%), Dol (6%)
	03		Qrtz α (90,1%), Dol (4%), Ank (3%), Hl (3%)
	04		Qrtz α (52%), Cal (27%), Ank (16%), Dol (5%)
	05		Qrtz α (94,1%), Dol (3%), Ank (2%), Hl (1%)
	06		Qrtz α (94%), Dol (6%)
	07		Dol (60%), Qrtz α (29%), Ank (8%), Py (3%)
	08		Qrtz α (91%), Dol (6%), Ank (3%)
125/20 - 004	5149.245	Chert lens with chalcedony	Quartz α (83%), Mg- Calcite (10%), Calcite (5%), Dolomite (2%)
Punctual sampling	01		Qrtz α (57%), Mg-cal (37%), Cal (6%)
	02		Qrtz α (87%), Cal (13%)
	03		Qrtz α (96%), Cal (3%), Hl (1%)
	04		Qrtz α (37%), Cal (33%), Py (30%)
	05		Qrtz α (84%), Cal (9%), Dol (7%)
	06		Qrtz α (66,3%), Mg-Cal (16,8%), Dol (7,9%), Ank (5,9%), Cal (3%)
	07		Qrtz α (92%) Cal (8%)

The chemical composition was obtained from homogenized bulk rock through X-ray fluorescence, with results in weight % major oxides in Table 2 and trace elements in Table 3.

Table 2: Major elements distribution through X-ray fluorescence (XRF), results in weight % oxides

Major elements distribution (XRF). Values in weight % oxides.											
Sample	**Depth**	**CaO**	**MgO**	**SiO_2**	**Al_2O_3**	**Fe_2O_3**	**Na_2O**	**K_2O**	**TiO_2**	**L.O.I**	**SUM**
195	5027.73	41.24	1.84	11.82	2.02	0.94	0.47	0.57	0.17	38.07	98.10
189	5030.17	11.23	4.79	62.47	1.74	1.48	0.67	0.32	0.14	16.25	99.77
004	5149.245	10.15	0.28	78.44	0.08	0.24	0.19	0.02	< 0.01	9.48	99.10

Table 3: Trace element detected through X-ray fluorescence (XRF) results in ppm.

Trace element detected (XRF)—values in ppm.															
Sample	**Depth**	**Ba**	**Ce**	**Cu**	**La**	**Nb**	**Nd**	**Pb**	**Rb**	**S**	**Sr**	**V**	**Y**	**Zn**	**Zr**
195	5027.73	1045	55	15	40	3	52	12	4	4228	1757	60	4	6	39
189	5030.17	242	55	16	41	8	52	18	7	3947	600	60	5	5	31
004	5149.245	360	55	6	51	23	51	4	3	647	344	9	4	474	32

Carbon and Oxygen stable isotope ratios (‰V-PDB), with mineralogical composition (XRD) obtained through punctual micro-sampling according to mineral assemblage variation, are summarized in Table 4.

Table 4: Carbon and Oxygen stable isotope ratios according to mineralogical assemblage. Values in ‰V-PDB.

Carbon and Oxygen stable isotope ratios. Values in ‰V-PDB						
Sample	**Depth**	**Drill code**	**$\delta^{13}C$**	**1σ [$\delta^{13}C$]**	**$\delta^{18}O$**	**1σ [$\delta^{18}O$]**
125/20 - 195	5027.73	Bulk	2.35	0.15	0.48	0.09
Punctual sampling		1A	2.85	0.13	0.6	0.1
		1B	2.19	0.03	0.58	0.05
		1C	3.1	0.17	0.89	0.15
		1D	2.61	0.13	0.33	0.06
		2A	2.36	0.16	-0.15	0.15
		2B	2.25	0.02	0.82	0.12
		2C	3.12	0.17	0.65	0.13
		2D	2.1	0.03	-0.33	0.1
		3A	3.25	0.11	2.37	0.09
		3B	2.33	0.08	1.07	0.03
		3C	3.31	0.12	1.58	0.07
		3D	2.66	0.09	0.81	0.07
		Drill average	2.68	0.31	0.77	0.28
Sample	**Depth**	**Drill code**	**$\delta^{13}C$**	**1σ [$\delta^{13}C$]**	**$\delta^{18}O$**	**1σ [$\delta^{18}O$]**
125/20 - 189	5030.17	Bulk	3.44	0.13	2.70	0.03
Punctual sampling		1A	3.79	0.12	2.04	0.07
		1B	3.85	0.17	1.35	0.16
		1C	2.04	0.07	1.01	0.03
		1D	No signal			
		2A	3.37	0.03	2.29	0.03
		2B	No signal			
		2C	2.85	0.16	1.54	0.1
		2D	No signal			
		3A	2.66	0.16	2.52	0.08
		3B	3.09	0.18	0.90	0.11
		3C	2.95	0.12	2.04	0.09
		3D	No signal			
		3E	No signal			
		3F	3.21	0.05	2.54	0.06
		3G	3.34	0.09	2.69	0.07
		3H	2.73	0.14	1.89	0.07
		Drill average	3.08	0.35	1.89	0.24

Sample	Depth	Drill code	$\delta^{13}C$	1σ [$\delta^{13}C$]	$\delta^{18}O$	1σ [$\delta^{18}O$]
125/20 - 004	5149.245	Bulk	-1.69	0.10	-0.26	0.05
Punctual sampling		1A	-2.13	0.08	-0.53	0.04
		1B	No signal			
		1C	-2.26	0.09	-0.88	0.05
		1D	-2.67	0.23	-1.46	0.19
		2A	-1.34	0.21	-1	0.18
		2B	-2.24	0.17	-3.12	0.13
		2C	-2.19	0.17	-1.93	0.18
		2D	-3.56	0.12	-0.96	0.08
		3A	-2.58	0.16	1.27	0.09
		3B	-2.06	0.12	-0.23	0.14
		3C	No signal			
		3D	-2.19	0.13	-2.85	0.07
		3E	0.33	0.19	1.48	0.11
		3F	-1.97	0.09	-1.81	0.03
		3G	-2.83	0.14	-0.99	0.06
		Drill average	-2.13	0.44	-1.00	0.31

5 DISCUSSIONS

In summary, the mineralogy of the studied samples represents a chronological sequence of events starting with (1) Laminated carbonates deposition (Syn-sedimentary), followed by compaction (Syn-sedimentary to Eo/Mesodiagenesis), stylolitization and dolomitization in a post-depositional phase (eo/mesodiagenesis); (2) In sequence, occurs three silicification phases, starting with chert, followed by chalcedony cementation, and Mega-Quartz growth (mesodiagenesis); (3) Finally, the last process reflected in the mineral assemblage concerns the migration of organic matter associated with sulfidation (mesodiagenesis) allowing precipitation of barite, Sr-barite, acicular gypsum, cubic and octahedron pyrite. Therefore, the next topic aims to elucidate the conditions required for the genesis of the mineral assemblage described in the studied samples, summarized in Table 5.

Table 5: Paragenetic sequence of the mineral assemblage.

Paragenetic Sequence Processes / Products	Syn-depositional	Burial Diagenesis	
		Eodiagenesis	Mesodiagenesis
Laminated Mudstone	----------		
Compaction	?------	----------	--------
Stylolitization		?----------	--------
Dolomitization		----------	-------
Chert silicification			? -------
Chalcedony cementation			-------
Drusiform/Mega-Quartz			-------
Sulfates (Barite, Gypsum)			----------
Sulfides (Pyrite)			----------
Amorphous Organic Matter			---------

5.1 FRAMEWORK - CARBONATES

5.1.1 Framework deposition (Laminated mudstones)

As previously described, the Fragata well sampling represents the Pre-salt Transitional Sequence as part of the Gondwana compartmentation and Atlantic Ocean formation (Aptian – Lower Cretaceous, Local stage Alagoas) (Castro and Picolini, 2015; Mohriak et al., 2012; Wright and Tosca, 2016). The main lithology drilled (Macabú Fm. section) consists of laminated mudstones, while the top (Retiro Fm. section) consists of anhydrite and halite. The sampled lithologies information added to previous studies indicates a transition to an evaporitic system (Farias et al., 2019; Sonnenfeld, 2001). The observed mineral assemblage consists of calcite and Low-Mg calcite. Due to increasing positive ratios, the Carbon and Oxygen Isotopic

data show a general evaporative trend. It is important to emphasize that the Fragata sampling occurs at the top of the transitional sequence, close to the salt layers, explaining the predominance of laminated mudstones with evaporitic tendency, and restricted stromatolite/microbial presence.

Considering the Pre-salt Transitional Sequence, some studies show the occurrence of microbialites (stromatolites) (Hendry et al., 2021; Saller et al., 2016) above the bioclastic grainstones and rudstones (*Coquinas* from Upper Rift Sequence) (Herlinger et al., 2017; Lima et al., 2019; Muniz and Bosence, 2018) with sampling mostly related to the onsetting of carbonate platform overlapping a lacustrine environment. On the other hand, studies with samples from the top of the Transitional Sequence show lithologies mainly composed of calcite in the form of laminated mudstones, spherulites, and shrubs, usually with evaporitic trends for carbon and oxygen stable isotopes (Farias et al., 2019; Hendry et al., 2021). The main interpretation regarding the possibility of developing an evaporitic system for the region occurs around the Walvis Ridge Vulcanic Belt, which prevented marine incursions (Farias et al., 2019; Rochelle-Bates, 2019).

5.1.2 Burial Compaction and Stylolitization – Eodiagenesis to Mesodiagenesis

Mechanical and chemistry compaction represents important evidence of diagenesis (Eodiagenesis to mesodiagenesis) action in the studied laminated mudstone framework concerning two main aspects: (1) the stylolitization features settled before the chert phase as evidenced by petrography; and (2) the possibility of Magnesium ions availability – from remobilization to a possible source for dolomitization;

The compaction processes evidenced by the carbonates tangential to sutured contacts, with portions subjected to the high-pressure solution evidenced by stylolitization (Choquette and James, 1987; Flügel, 2010) containing solid, insoluble residues such as aluminum, sulfur, salts (halite), and high carbon content. The petrographic relation between the compacted framework and the silica layers/nodules indicates some compaction degree, with the silicification starting after the stylolite development.

Despite the lack of clay minerals and aluminosilicates in XRD, the petrophysical parameter in Fragata well indicates the presence of clay/shale (Chap. 3 - Methods). Furthermore, aluminum as an insoluble residue in stylolite suggests the possibility of Magnesium remobilization from clay minerals and a source for dolomitization (Choquette and James, 1987; Flügel, 2010; Warren, 2000).

5.1.3 Dolomitization – Eodiagenesis / Mesodiagenesis

The term "Dolomite problem" have been among the discussion topics by scientists over the past 170 years because dolomite is not a simple or usual mineral. The genesis of dolomite crystals can be primary (direct precipitation - rare) or secondary (diagenetic replacement – more common) (Flügel, 2010; Tucker, 1990; Tucker and Bathurst, 2009; Warren, 2000). Dolomite presence in the Brazilian Pre-salt Upper Rift and Transitional Sequence is recorded in many previous studies from Campos (Herlinger et al., 2017; Lima et al., 2019) and Santos Basins (Farias et al., 2019; Gomes et al., 2020), commonly described as saddle and blocky dolomite, with some cases evidencing zoned pattern. They appear to fill framework or vuggy porosities or as a mineral replacement. Lima et al. (2019, 2020) suggested that dolomitization occurs before the silicification process as a pre-existing phase due to the absence of silica inclusions in dolomite crystals (Lima et al., 2020, 2019).

In the Fragata case, dolomite occurs distributed along the well. The detailed studies show the occurrence of Ca-dolomite (disordered dolomite) in rhomb, blocky, and saddle crystals, sometimes with zoned patterns and portions in solid solution between ankerite. The floating textural feature of dispersed dolomite crystals in the middle of the silica matrix strongly indicates the dolomitization before silicification (Chert phase). In addition, the absence of dolomite and calcite crystals related to chalcedony and mega-quartz means stopping dolomitization availability during the chalcedony cementation phase and drusiform quartz growth for the studied sections.

Considering the Brazilian Pre-salt context and the Fragata well data, the main requirements for dolomitization are attended to since (1) sampling history starts with mineral assemblages evidencing alkaline systems (Calcite and Low-Mg calcite as laminated mudstones) (Gomes et al., 2020; Herlinger et al., 2017; Lima et al., 2020, 2019) with a transition to an evaporitic system (Anhydrite and Halite) (Farias et al., 2019; Rodriguez et al., 2018), which attends the hypersaline brines or schizohaline waters circulation requirement; (2) compaction and stylolitization evidence with solid residues composed mainly by Al^{3+}, as a partial answer for Mg^{2+} ions availability, in addition to the rifting regional context with tholeiitic magmatism to fulfill the Mg and Fe ions necessity; (3) geological time from Aptian (Cretaceous) until Holocene, in a carbonate layer covered by large salt layers attend the requirements for long-term dolomitization;

Concerning the temperature elevation required for acceleration of the dolomitization, the process may involve the heating by geothermal gradient due to increased depth (Kohout convection model). In addition, for confirmation of hydrothermal dolomitization possibilities,

temperature data comparing dolomite related to faults with hydrothermal circulation and the adjacent areas are required to state hydrothermal circulation influence.

5.2 SILICA (MESODIAGENESIS)

The silicification phases observed in this case study, as previously described, occur in three stages: (1) Chert silicification (Granular Microcrystalline Silica); (2) Chalcedony cementation (Fibrous Microcrystalline Silica); (3) Mega-quartz growth (Macrocrystalline Silica). It is important to note that silicification observed in this study probably started after a certain degree of framework burial compaction due to the petrographic relation between the silica layers/nodules with compaction features such as grain boundaries and stylolitization before chert precipitation, in addition to the textural connection between dolomite/ankerite and calcite with silica.

Previous research in Pre-salt Upper-Rift and Transitional Sequence relates silicification and silica cementation in the Brazilian margin Campos (De Luca et al., 2017; Lima et al., 2020, 2019) and Santos Basins (Gomes et al., 2020) in addition to Congo, Kwanza and Namibia Basins at the African Margin (Poros et al., 2017; Rochelle-Bates, 2019; Saller et al., 2016; Teboul et al., 2019). The silica presence in Pre-salt reservoirs has an important impact on porosity and permeability. However, although several authors report the presence of silicification, just a few studies detail the textural and structural variation related to the silica and the carbonate framework (Lima et al., 2020, 2019; Poros et al., 2017; Teboul et al., 2019).

5.2.1 Physicochemical Availability: Silica versus Carbonates

The main problem involved in the silicification of carbonates concerns the differences in hydrogen ionic potential (pH) necessary for precipitation and stability of minerals formed based on the anionic group carbonate [$X(CO_3)^{2-}$] versus silica (SiO_2).

C*hemical carbonates* have restricted environmental occurrence, usually formed due to water saturation, related to a source rock dissolution allowing cations and anions availability (Ca^{2+}, Mg^{2+}, CO_3^{2-}, $2HCO_3^-$), and subsequent precipitation by CO_2 input or withdrawal, contributing to pH changes.

Silica, on the other hand, has a wide crustal distribution, as the base tetrahedron SiO_2, with its polymerization ability, makes possible a diversity of structural configurations, allowing seven structural arrangements as the basis for most of the rocking-forming minerals. In this way, silicate base minerals compose around 90% of the earth's crust (Dana and Ford, 1960; Klein and Dutrow, 2012), with 64% of crustal rocks based on tectosilicates [unit composition

$(SiO_4)^{4-}$] in three main polymorphs Quartz, Tridymite, and Cristobalite from natural pressure and temperature conditions, with α/β variations according to temperature, in addition to stishovite and coesite as high-pressure compounds (Berry, 1981; Götze, 2009).

The alkaline hydrogen ionic potential (pH), considering surface conditions as 25ºC and 1atm, have an ideal field precipitation for carbonates (Calcite) usually above pH 8.2, with dissolution starting below pH 8 and increasing below pH 4.3 (Capezzuoli et al., 2014; Dupraz et al., 2009; Ford and Pedley, 1996). While, the silica solubility potential works oppositely compared to carbonates, with solubility increasing above pH9 and precipitation with alkalinity reduction in pH<9, and increasing precipitation below pH4. However, despite this potential solubility opposition, there is a minimum co-precipitation window between silica and carbonates under pH 4 to 8, with a maximum solubility of 50 ppm at pH 6 (Bustillo, 2010; Mustoe, 2018; Nicholson K., 1993; Trewin and Fayers, 2004).

When the system temperature increases, the solubility potential for silica also increases, with a critical point under 300ºC (Nicholson K., 1993). In this way, water circulation through convective currents under thermogenic processes influence can be responsible for the dissolution of depth rocks, and upon reaching the surface, waters under high temperature and pressure from the subsurface undergo a loss of temperature and CO_2, with cooling and possible alkalinity increase. In this way, silica-saturated water will consequently face silica precipitation, such as hot springs, volcanism, deep faults, and rift lakes (Bons, 2001; Capezzuoli et al., 2014; Schmidt et al., 2013).

5.2.2 Silica in the Pre-salt Transitional Sequence (Fragata Case – Campos Basin)

To understand the silica present in a carbonate-dominated environment as the Pre-Salt Transitional Sequence (SAG), we need to consider three main points:

(1) Physicochemical availability through the hydrogenic potential influence, considering a high alkalinity environment (possible pH>9), dominated by carbonate precipitation (Laminated mudstones), and the restricted co-precipitation window between carbonates and silica. In this way, the pH is favorable for silica dissolution, with minor reductions allowing silica precipitation (Bustillo, 2010; Mustoe, 2018; Trewin and Fayers, 2004).

(2) The high possibility of thermogenic processes influencing the dissolution potential increased with temperature, considering the system as a transition between a Rift to a Passive Margin phase (De Luca et al., 2017; Lima et al., 2019). As previously reported, silicification

with hydrothermal influence through fluid circulation (Lima et al., 2019; Poros et al., 2017; Teboul et al., 2017).

(3) Two main possible silica sources, as reported in Pre-salt literature, are the tholeiitic volcanism (Cabiúnas Fm.) followed by siliciclastic rocks deposition in layers below the carbonates (Itabapoana and Atafona Fm.) during the Lower Rift Phase (Hauterivian to Barremian - Lower Cretaceous) (Castro and Picolini, 2015; Herlinger et al., 2017; Mohriak et al., 2012).

5.2.3 Silica phases (α - Quartz textural variation)

Due to XRD results, consider the silica polymorphs α- Quartz as the focus of this study. α- Quartz is the variety with stability in low temperature (<573ºC) and pressure (<2GPa) related to surface environments, normally represented in different petrographic and textural aspects as granular microcrystalline (Chert), fibrous microcrystalline (Chalcedony), and macrocrystalline varieties (Mega-Quartz) (Berry, 1981; Götze, 2009; Schmidt et al., 2013).

The hypothesis addressed is that the textural variation of silica could indicate a sequence of crystallization, starting with a silica-rich fluid circulation and first chert silicification and carbonate replacement, followed by changes to allow chalcedony cementation under contact or influence of high salinity fluids, and finally, the precipitation of quartz where space is available from a remaining pure silica saturated-fluid.

Chert silicification

Chert (Granular Microcrystalline Silica) is the first textural variety of α- Quartz identified as layers/nodules in the middle of the studied Fragata well carbonate (Laminated mudstones). The petrographic relation between the chert and the mudstones allows interpretation of the silicification establishment after some degree of compaction and stylolitization, with the chert shifting the mudstones' laminations.

Another important aspect of these samples is the presence of dispersed carbonate crystals (Calcite, Low Mg-Calcite, Ca-dolomite, and Ankerite). While Calcite and Low-Mg Calcite appears highly replaced by silica, Ca-dolomite/Ankerite occurs in rhomb or saddle-zoned crystals without silica replacement, in a floating texture in the silica matrix, suggesting silicification after the dolomitization. In complement to previously interpreted silicification in Campos Basin beginning after dolomitization due to the absence of silica inclusions in dolomite crystals (Lima et al., 2020, 2019).

The results of oxygen-stable isotopes for both calcite and dolomite show an irregular distribution outside the standard deviation range of the average and bulk-rock value, indicating oxygen sensitivity to heating, allowing to include the possibility of the thermogenic process involved in the silica-rich fluid circulation. In a petrographic ordination of events, the next aspect involving the studied samples concerns the presence of fractures and brecciation, not trespassing on the framework, suggesting that the brittle broken is probably due to compaction and weight. In addition, the channels and vuggy porosity in the chert evidence a dissolution episode through the weakness plans.

Chalcedony cementation

The Chalcedony (Fibrous Crypto/Microcrystalline Silica) is found in a wide range of geological environments, igneous, metamorphic, and sedimentary, often filling spaces and cavities, such as vesicles, moldic, channels, and vuggy porosities. It also can occur as a cement component in sedimentary rocks or forming pseudomorph due to replacement (Navarro et al., 2017; Schmidt et al., 2013; Trewin and Fayers, 2004).

Chalcedony in the Fragata case is a cementation phase inside the chert layers/nodules in fractures, faults, vuggy, and channel porosities. It is important to highlight the absence of carbonate crystals (Calcite, Low Mg-Calcite, Ca-dolomite, and Ankerite), with just a few crystals trapped during the cementation cycle, suggestive of dolomitization ends before chalcedony cementation starts.

Concerning the abundance of halite (NaCl) associated with chalcedony, most of the halite accompanies the intergrowth features of chalcedony in large crystals forming aggregates but also occurs as crypto/micro crystallites in the silica matrix, given the white color of the samples. Studies in Pre-salt rocks require care because the salt in the adjacent layers and the mud used in drilling can cause contamination of the material by infiltrating the rock porosity (Rochelle-Bates, 2019; Rosin, 2021).

However, in this case, the absence of salt in certain microfacies, and its abundance related to chalcedony, is a strong indication that salt (halite) is part of the original mineralogical assembly and there is a genetic implication of a hypersaline fluid action in the precipitation of chalcedony, possibly under a mixing water influence.

Mega-Quartz Growth

The last silica textural variation in Fragata samples refers to translucent and transparent Mega-Quartz crystals (Granular Microcrystalline Silica) directly dependable on abundance and

remaining pure silica. Considering the drusiform quartz as clean crystals, filling vuggy, channel, and cavities after the chalcedony cementation enable us to infer a pure silica saturated-fluid circulation, in complement to the transparent aspect evidences the absence of major oxides at SiO_2 cationic sites, in this last silica phase.

5.3 SULFIDATION WITH HYDROCARBON MIGRATION – (MESODIAGENESIS)

After the silicification events, the remaining porosities (vuggy, channel, and fractures in silica layers, and fenestral porosities for the framework) are filled by sulfides (cubic and octahedron pyrite), sulfates (acicular gypsum, barite, and Sr-barite), and amorphous organic matter (carbon). In this last diagenetic phase, the mineral assemblage indicates the pH, oxygen fugacity, and temperature for the organic carbon (C) associated with Sulfur (S) migration.

Barite ($BaSO_4$) commonly forms a solid solution series with Celestine ($SrSO_4$) and Anhydrite ($CaSO_4$). The geological significance of Barite refers to the fact that most of the existing Barite on the Earth's surface forms due to a mixture of fluids, one of which must contain barium (Ba) from silicates, and the other contains sulfur (S) from a swallow and oxidized environment. Consequently, barite is observed in various geological settings, with precipitation from temperatures below 400ºC and pressure below 2 kbars (Hanor, 2019; Klein and Dutrow, 2012).

Since barite is redox-sensitive, the presence of this mineral allows paleo-redox and paleohydrology reconstructions. Celestine distribution is geologically restricted in comparison to Barite. Their occurrence reflects special geological conditions with Strontium (Sr) concentration over Barium (Ba), mostly of the Celestine occurrence appears implicates in reactions from hypersaline Sr-bearing fluids with gypsum ($CaSO_4*2H_2O$) and anhydrite ($CaSO_4$) (Hanor, 2019; Klein and Dutrow, 2012).

For the Fragata case study, Barite and Sr-Barite were detected in the mineral assemblage (SEM-EDX), and traces of acicular gypsum (SEM-EDX / XRD). The association of Barite, and Sr-Barite with cubic and octahedron pyrite, combined with the absence of other iron oxides (hematite, galena, sphalerite, magnetite, and pyrrhotite) delimits a range of hydrogen ionic potential (pH: 1 to 5) and oxygen fugacity (log fO_2: -45 to -55) (Hanor, 2019), in a phase of Sulfur (S) mobilization through organic matter migration (Dembicki, Jr., 2017).

6 CONCLUSIONS

The Fragata well lithology represents the upper part of the Transitional Sequence in the geological context of the Brazilian Pre-Salt (Aptian – Lower Cretaceous), with sampling from laminated, spherulitic and fascicular carbonates (Macabú Fm.), to evaporites as anhydrite and halite (Retiro Fm.). This study emphasizes the silicification processes through a combination of petrographic, geochemical, and isotopic data. We demonstrate that the silica has three textural variation patterns starting with Chert (Granular Microcrystalline Silica), followed by Chalcedony (Fibrous Microcrystalline Silica) cementation, and finally ends with Mega-Quartz growth (Granular Macrocrystalline Silica).

The mineralogical assemblage associated with silica also varies according to each texture difference: (1) Chert associated with carbonate crystals (Calcite, Low Mg-Calcite, Ca-Dolomite/Ankerite) dispersed in a floating texture; (2) Chalcedony cementing porosities, marked by carbonate absence, and abundance of halite (NaCl) as the probable factor responsible by the white color; (3) Drusiform/Mega-Quartz growth when space is available, ending the silicification with translucent and transparent quartz crystals. The last minerals phases disposed of in these samples filling the porosities after the silicification are sulfates such as Barite, Sr-Barite, and traces of acicular Gypsum, in addition to the octahedron and cubic pyrite associated with amorphous organic matter (Carbon).

The silicification phases observed in the Fragata case are possibly related to a post-depositional process, due to the petrographic relation between carbonate crystals and the silica, with the silicification starting after some degree of compaction, stylolitization, and dolomitization. In addition, dissolution from adjacent layers (Itabapoana Fm.) and reprecipitation may be under thermogenic processes influence as one of the main possible sources for the silica layers/nodules in the system.

ACKNOWLEDGMENTS

We express our gratitude to the two projects that support this research: (1) Diagenesis Project [Grant number 23075.193990/2017-07] from Shell Brazil; (2) GeoQI Project [Grant number 23075.039121/2022-97]. Both as a Technical-Scientific Cooperation with the Paraná Federal University (UFPR) / LAMIR Institute, in compliance with the provisions of Law 9,478 of August 6, 1997 (Petroleum Law) and Clause 22.2 of the Concession Contract executed with ANP (National Petroleum, Natural Gas, and Biofuel Agency). We thank ANP for providing the studied material allowing sampling and destructive analysis [SEI/ANP – Official document number 424/2019/SDT-e-ANP. Process number 48610.211854/2019-70].

We thank Lamir Institute/UFPR for providing support and infrastructure and the iLamir team for all collaborations. In addition, we are grateful for CME/UFPR (Centro de Microscopia Eletrônica), CTAF/UFPR (Centro de Tecnologias Avançadas em Fluorescência) for petrographic analysis, and CALTECH (Californian Institute of Technology) for XRF spectrometer analysis.

Funding: This research has major financial support (April/2021 to October/2022) from Shell Brazil through the Diagenesis Project - *Diagenesis of Pre-Salt non-marine carbonate sequences and its impact on Exploration and Production of hydrocarbon reservoir* [Grant number 23075.193990/2017-07]. With complimentary support (November/2022 to June/2023) from Petrobras S.A through GeoQI Project - *High-Resolution Geochemical Characterization in the Aptian Sequence of the Santos Basin* (through the technique of Clustered Isotopes and Sr in situ) [Grant number 23075.039121/2022-97].

REFERENCES

Alonso, G.E., 2022. Characterization and faciological description of the Vega Verde Travertine System in Botijuela, Quaternary-Argentine South Puna. Universidade Federal do Paraná.

Antunes, R. de C., 2021. Modelo deposicional das coquinas do Campo de Búzios, Bacia de Santos. Universidade Federal do Paraná.

Bahniuk, A.M.R., 2013. Coupling Organic and Inorganic Methods to Study Growth and Diagenesis of Modern Microbial Carbonates , Rio de Janeiro State , Brazil : Implications for Interpreting Ancient Microbialite Facies Development. ETH ZURICH.

Barnett, A.J., Obermaier, M., Amthor, J., Juk, K., Camara, R., Sharafodin, M., Bolton, M., 2018. Origin and significance of thick carbonate grainstone packages in non-marine successions : a case study from the Barra Velha Formation, Santos Basin. AAPG Annu. Conv. Exhib. 1–5.

Berry, L.G., 1981. Polymorphism. Minerogy. https://doi.org/https://doi.org/10.1007/0-387-30720-6_110

Bons, P.D., 2001. The formation of large quartz veins by rapid ascent of fluids in mobile hydrofractures. Tectonophysics 336, 1–17. https://doi.org/10.1016/S0040-1951(01)00090-7

Bustillo, M.A., 2010. Chapter 3 Silicification of Continental Carbonates, Developments in Sedimentology. Elsevier. https://doi.org/10.1016/S0070-4571(09)06203-7

Cainelli, C., Mohriak, W.U., 1999. General evolution of the eastern Brazilian continental margin. Lead. Edge 18, 1–5. https://doi.org/10.1190/1.1438387

Capezzuoli, E., Gandin, A., Pedley, M., 2014. Decoding tufa and travertine (fresh water carbonates) in the sedimentary record: The state of the art. Sedimentology 61, 1–21. https://doi.org/10.1111/sed.12075

Carminatti, M., Dias, J., Wolff, B., 2009. From Turbidites to Carbonates: Breaking Paradigms in Deep Waters, in: In: Offshore Technology Conference. Houston, pp. 4–7. https://doi.org/10.4043/otc-20124-ms

Castro, R.D. De, Picolini, J.P., 2015. Principais aspectos da geologia regional da Bacia de Campos, in: Kowsmann, R.O. (Ed.), Geologia e Geomorfologia: Caracterização Ambiental Regional Da Bacia de Campos, Atlântico Sudoeste. Elsevier, Rio de Janeiro, pp. 1–12. https://doi.org/10.1016/B978-85-352-6937-6.50008-2

Choquette, P., James, N.P., 1987. Diagenesis in Limestones - The Deep Burial Environment. Geosci. Canada 4, 3–35.

Choquette, P.W., Pray, Ll.C., 1970. Geologic Nomenclature and Classification of Porosity in Sedimentary Carbonates. Am. Assoc. Pet. Geol. Bull. 54, 207–250. https://doi.org/10.1306/5d25c98b-16c1-11d7-8645000102c1865d

Crist, B., Schultz, J.M., 2016. Polymer spherulites: A critical review. Prog. Polym. Sci. 56, 1–63. https://doi.org/10.1016/j.progpolymsci.2015.11.006

Dahanayake, K., 1978. Sequential position and environmental significance of different types of oncoids. Sediment. Geol. 20, 301–316. https://doi.org/10.1016/0037-0738(78)90060-X

Dana, E., Ford, W., 1960. Dana's manual of mineralogy, 15th ed, John Wiley & Sons, Inc. New York.

De Luca, P., Carballo, J., Filgueiras, A., Pimentel, G., Esteban, M., Tritlla, J., Villacorta, R., 2015. What is the role of volcanic rocks in the Brazilian pre-salt? 77th EAGE Conf. Exhib. 2015 Earth Sci. Energy Environ. 1686–1690. https://doi.org/10.3997/2214-4609.201412890

De Luca, P.H.V., Matias, H., Carballo, J., Sineva, D., Pimentel, G.A., Tritlla, J., Esteban, M., Loma, R., Alonso,

J.L.A., Jiménez, R.P., Pontet, M., Martinez, P.B., Vega, V., 2017. Breaking barriers and paradigms in presalt exploration: The pão de açúcar discovery (Offshore Brazil). AAPG Mem. 113, 177–193. https://doi.org/10.1306/13572007M1133686

Decho, A.W., Visscher, P.T., Reid, R.P., 2005. Production and cycling of natural microbial exopolymers (EPS) within a marine stromatolite. Palaeogeogr. Palaeoclimatol. Palaeoecol. 219, 71–86. https://doi.org/10.1016/j.palaeo.2004.10.015

Dedavid, B.A., Gomes, C.I., Machado, G., 2007. Microscopia Eletronica de Varredura - Aplicações e preparação de amostras - Materiais Poliméricos, metálicos e semicondutores, Dados Internacionais de Catalogação na Publicação (CIP). EDIPUCRS- Instituto de Pesquisa e Desenvolvimento, Porto Alegre.

Défarge, C., Gautret, P., Reitner, J., Trichet, J., 2009. Defining organominerals: Comment on "Defining biominerals and organominerals: Direct and indirect indicators of life" by Perry et al. (2007, Sedimentary Geology, 201, 157-179). Sediment. Geol. 213, 152–155. https://doi.org/10.1016/j.sedgeo.2008.04.002

Dembicki, Jr., H., 2017. Interpreting Crude Oil and Natural Gas Data, in: Dembicki, Jr., H. (Ed.), Practical Petroleum Geochemistry for Exploration and Production. Elsevier, Amsterdan, pp. 135–188. https://doi.org/10.1016/b978-0-12-803350-0.00004-0

Dorneles, V.A.C., 2018. Caracterização Geoquímica e Geomicrobiológica de Microbialito da Lagoa Salgada, Estado do Rio de Janeiro. Universidade Federal do Paraná.

Dunham, R.J., 1962. Classification of Carbonate Rocks According to Depositional Texture., in: Classification of Carbonate Rocks. pp. 108–121.

Dupraz, C., Reid, R.P., Braissant, O., Decho, A.W., Norman, R.S., Visscher, P.T., 2009. Processes of carbonate precipitation in modern microbial mats. Earth-Science Rev. https://doi.org/10.1016/j.earscirev.2008.10.005

Embry, A., Klovan, E., 1971. Alate Devonian reef tract on northeastern Banks Island , N . W . T. Bull. Can. Pet. Geol. 19, 730–781. https://doi.org/10.35767/gscpgbull.19.4.730 Article history Cite

Farias, F., Szatmari, P., Bahniuk, A., França, A.B., 2019. Evaporitic carbonates in the pre-salt of Santos Basin – Genesis and tectonic implications. Mar. Pet. Geol. 105, 251–272. https://doi.org/10.1016/j.marpetgeo.2019.04.020

Flügel, E., 2010. Microfacies of Carbonate Rocks, Microfacies of Carbonate Rocks. https://doi.org/10.1007/978-3-642-03796-2

Ford, T.D., Pedley, H.M., 1996. A review of tufa and travertine deposits of the world. Earth-Science Rev. 41, 117–175. https://doi.org/10.1016/s0012-8252(96)00030-x

Gomes, J.P., Bunevich, R.B., Tedeschi, L.R., Tucker, M.E., Whitaker, F.F., 2020. Facies classification and patterns of lacustrine carbonate deposition of the Barra Velha Formation, Santos Basin, Brazilian Pre-salt. Mar. Pet. Geol. 113, 104176. https://doi.org/10.1016/j.marpetgeo.2019.104176

Götze, J., 2009. Chemistry, textures and physical properties of quartz — geological interpretation and technical application. Mineral. Mag. 73, 645–671. https://doi.org/10.1180/minmag.2009.073.4.645

Gouveia, F., 2010. Tecnologia nacional para extrair petróleo e gás do pré-sal. Conhecimento & Inovação 6, 30–35.

Guardado, L. r., Spadini, A. r., Brandão, J.S.L., Mello, M. r., 2000. Petroleum system of the Campos Basin, Brazil., in: Mello, M. r., Katz, B.J. (Eds.), Petroleum Systems of South Atlantic Margins. AAPG Memoir, pp. 317–324.

Hanor, J.S., 2019. Barite-celestine geochemistry and environments of formation. Sulfate Miner. Crystallogr. Geochemistry, Environ. Significance 40, 193–275. https://doi.org/10.2138/rmg.2000.40.4

Heaney, P.J., 1993. A proposed mechanism for the growth of chalcedony. Contrib. to Mineral. Petrol. 115, 66–74. https://doi.org/10.1007/BF00712979

Heaney, P.J., Veblen, D.R., Post, J.E., 1994. Structural disparities between chalcedony and macrocrystalline quartz. Am. Mineral. 79, 452–460.

Hendry, J., Burgess, P., Hunt, D., Janson, X., Zampetti, V., 2021. Seismic characterization of carbonate platforms and reservoirs: An introduction and review. Geol. Soc. Spec. Publ. 509, 1–28. https://doi.org/10.1144/SP509-2021-51

Herlinger, R., Zambonato, E.E., Ros, L.F.D.E., 2017. Influence of diagenesis on the quality of lower cretaceous Pre-salt lacustrine carbonate reservoirs from northern Campos basin , offshore Brazil. Jourmal Sediment. Res. 87, 1285–1313. https://doi.org/10.2110/jsr.2017.70

Hoefs, J., 2009. Stable Isotope Geochemistry, 6th ed. Springer, Berlin.

Huber, B.T., MacLeod, K.G., Watkins, D.K., Coffin, M.F., 2018. The rise and fall of the Cretaceous Hot Greenhouse climate. Glob. Planet. Change 167, 1–23. https://doi.org/10.1016/j.gloplacha.2018.04.004

Klein, C., Dutrow, B., 2012. Manual of Mineral Science, 23rd ed. bookman, Porto Alegre.

Lima, B.E.M., Fernando, L., Ros, D., 2019. Deposition , diagenetic and hydrothermal processes in the Aptian Pre-Salt lacustrine carbonate reservoirs of the northern Campos Basin , offshore Brazil. Sediment. Geol. 383, 55–81. https://doi.org/10.1016/j.sedgeo.2019.01.006

Lima, B.E.M., Ribeiro, L., Luiz, A., Pestilho, S., Fernando, L., Ros, D., 2020. Deep-burial hydrothermal alteration of the Pre-Salt carbonate reservoirs from northern Campos Basin , offshore Brazil : Evidence from petrography , fluid inclusions , Sr , C and O isotopes. Mar. Pet. Geol. 113, 104–143. https://doi.org/10.1016/j.marpetgeo.2019.104143

Lofgren, G., 1971. Spherulitic textures in glassy and crystalline rocks. J. Geophys. Res. 76, 5635–5648. https://doi.org/10.1029/jb076i023p05635

Logan, B.W., Rezak, R., Ginsburg, R.N., 1964. Classification and Environmental Significance of Algal Stromatolites. J. Geol. 72, 68–83. https://doi.org/10.1086/626965

Magill, J.H., 2001. Spherulites: A personal perspective. J. Mater. Sci. 36, 3143–3164. https://doi.org/10.1023/A:1017974016928

Mattos, R.F. de, 2016. Caracterização geoquímica, faciologica e permo-porosa de carbonatos continentais do Japáo. Universidade Federal do Paraná.

Mercedes-Martín, R., Brasier, A.T., Rogerson, M., Reijmer, J.J.G., Vonhof, H., Pedley, M., 2017. A depositional model for spherulitic carbonates associated with alkaline, volcanic lakes. Mar. Pet. Geol. 86, 168–191. https://doi.org/10.1016/j.marpetgeo.2017.05.032

Mercedes-Martín, R., Rogerson, M.R., Brasier, A.T., Vonhof, H.B., Prior, T.J., Fellows, S.M., Reijmer, J.J.G., Billing, I., Pedley, H.M., 2016. Growing spherulitic calcite grains in saline, hyperalkaline lakes: Experimental evaluation of the effects of Mg-clays and organic acids. Sediment. Geol. 335, 93–102. https://doi.org/10.1016/j.sedgeo.2016.02.008

Milani, E.J., Jahnert, R.J., França, A.B., 2017. Bacia de Campos. Bol. Geociências da Petrobras 15, 511–529.

Mohriak, W., Nemcok, M., Enciso, G., 2012. South Atlantic divergent margin evolution : rift-border uplift and

salt tectonics in the basins of SE Brazil. https://doi.org/10.1144/SP294.19

Muniz, M.C., Bosence, D.W.J., 2018. Lacustrine carbonate platforms: Facies, cycles, and tectonosedimentary models for the presalt Lagoa Feia Group (Lower Cretaceous), Campos Basin, Brazil. Am. Assoc. Pet. Geol. Bull. 102, 2569–2597. https://doi.org/10.1306/0511181620617087

Muniz, M.C., Bosence, D.W.J., 2015. Pre-salt microbialites from the Campos Basin (offshore Brazil): Image log facies, facies model and cyclicity in lacustrine carbonates. Geol. Soc. Spec. Publ. 418, 221–242. https://doi.org/10.1144/SP418.10

Mustoe, G.E., 2018. Mineralogy of non-silicified fossil wood. Geosci. 8. https://doi.org/10.3390/geosciences8030085

Nascimento-Dias, B.L. do, 2017. Aplicações multidisciplinares da microtomografia de raios X e sua utilização na caracterização e análises não-destrutivas de materiais. Rev. Bras. Física Tecnológica Apl. 4, 26–41. https://doi.org/10.3895/rbfta.v4n2.6984

Navarro, G.R.B., Zanardo, A., Montibeller, C.C., 2017. Tectossilicatos: Quartzo. Minerais Comuns e Econ. Relev. 1–7.

Nichols, G., 2009. Sedimentology and Stratigraphy, 2nd ed. Wiley-Blackwell, Chichester.

Nicholson K., 1993. Fluidos Geotermicos, quimica y tecnicas de exploración, Springer Verlag.

Oliveira, E.C. de, Rossetti, D.F., Utida, G., 2017. Paleoenvironmental evolution of continental carbonates in West-Central Brazil. An. Acad. Bras. Cienc. 89, 407–429. https://doi.org/10.1590/0001-3765201720160584

Oste, J.T.F., Rodríguez-berriguete, Á., Dal Bó, P.F., 2021. Depositional and environmental controlling factors on the genesis of Quaternary tufa deposits from Bonito region , Central-West Brazil. Sediment. Geol. 413, 105824. https://doi.org/10.1016/j.sedgeo.2020.105824

Perry, R.S., Mcloughlin, N., Lynne, B.Y., Sephton, M.A., Oliver, J.D., Perry, C.C., Campbell, K., Engel, M.H., Farmer, J.D., Brasier, M.D., Staley, J.T., 2007. Defining biominerals and organominerals: Direct and indirect indicators of life. Sediment. Geol. 201, 157–179. https://doi.org/10.1016/j.sedgeo.2007.05.014

Poros, Z., Jagniecki, E., Luczaj, J., Kenter, J., Gal, B., Correa, T.S., Ferreira, E., Kathleen, A., Elifritz, A., Heumann, M., Johnston, M., Matt, V., 2017. Origin of Silica in Pre-Salt Carbonates , Kwanza Basin , Angola. AAPG Annu. Conf. Exhib. 51413, 2–3.

Ralph, J., 2023. Chalcedony, in: MINDAT. Hudson Institute of Mineralogy, New York.

Randazzo, A.F., Zachos, L.G., 1984. Classification and description of dolomitic fabrics of rocks from the Floridan aquifer, U.S.A. Sediment. Geol. 37, 151–162. https://doi.org/10.1016/0037-0738(84)90005-8

Reis Neto, J.M. dos, Fiori, A.P., Lopes, A.P., Marchese, C., Pinto-Coelho, C.V., Vasconcellos, E.M.G., Silva, G.F. da, Secchi, R., 2018. A microtomografia computadorizada de raios x integrada à petrografia no estudo tridimensional de porosidade em rochas. Rev. Bras. Geociências 41, 498–508. https://doi.org/10.25249/0375-7536.2011413498508

Révész, K.M., Landwehr, J.M., 2002. δ13C and δ18O isotopic composition of CaCo3 measured by continuous flow isotope ratio mass spectrometry: Statistical evaluation and verification by application to Devils Hole core DH-11 calcite. Rapid Commun. Mass Spectrom. 16, 2102–2114. https://doi.org/10.1002/rcm.833

Riding, R.E., Awramik, S.M., 2000. Robert E. Riding and Stanley M. Awramik (Eds.) Microbial Sediments. New York. https://doi.org/10.1007/978-3-662-04036-2

Rochelle-Bates, N.M., 2019. Deposition and Diagenesis Along the Volcanic Rifted Margins of Angola and

Namibia. University of Manchester.

Rodriguez, C.R., Jackson, C.A.L., Rotevatn, A., Bell, R.E., Francis, M., 2018. Dual tectonic-climatic controls on salt giant deposition in the Santos Basin, offshore Brazil. Geosphere 14, 215–242. https://doi.org/10.1130/GES01434.1

Rosin, J.C. de F., 2021. Potencial do uso de amostras de calha na quimioestratigrafia do pré-sal, Bacia de Santos. Universidade Federal do Paraná.

Rudnick, R.L., Gao, S., 2003. Composition of the Continental Crust, 3rd ed, Treatise on geochemistry. Elsevier Ltd, Wuhan.

Saller, A., Rushton, S., Buambua, L., Inman, K., McNeil, R., Dickson, J.A.D.T., 2016. Presalt stratigraphy and depositional systems in the Kwanza Basin, offshore Angola. Am. Assoc. Pet. Geol. Bull. 100, 1135–1164. https://doi.org/10.1306/02111615216

Santos, E.S., 2013. Espectometria de Fluorescência de raios-X na determinação de espécies químicas. Enciclopédia Biosf.

Schmidt, P., Slodczyk, A., Léa, V., Davidson, A., Puaud, S., Sciau, P., 2013. A comparative study of the thermal behaviour of length-fast chalcedony, length-slow chalcedony (quartzine) and moganite. Phys. Chem. Miner. 40, 331–340. https://doi.org/10.1007/s00269-013-0574-8

Scotese, C.R., 2014. Atlas of Early Cretaceous Paleogeographic Maps, PALEOMAP Atlas for ArcGIS. The Cretaceous, maps 23-31. 2. https://doi.org/10.13140/2.1.4099.4560

Scotese, C.R., Song, H., Mills, B.J.W., van der Meer, D.G., 2021. Phanerozoic paleotemperatures: The earth's changing climate during the last 540 million years. Earth-Science Rev. 215, 103503. https://doi.org/10.1016/j.earscirev.2021.103503

Sibley, D.F., Gregg, J.M., 1987. Classification of dolomite rock textures. J. Sediment. Petrol. 57, 967–975. https://doi.org/10.1306/212f8cba-2b24-11d7-8648000102c1865d

Sonnenfeld, P., 2001. Evaporites, in: Meyers, R.A. (Ed.), Encyclopedia of Physical Science and Technology. Elsevier, California, pp. 653–671.

Teboul, P.A., Durlet, C., Girard, J.P., Dubois, L., San Miguel, G., Virgone, A., Gaucher, E.C., Camoin, G., 2019. Diversity and origin of quartz cements in continental carbonates: Example from the Lower Cretaceous rift deposits of the South Atlantic margin. Appl. Geochemistry 100, 22–41. https://doi.org/10.1016/j.apgeochem.2018.10.019

Teboul, P.A., Kluska, J.M., Marty, N.C.M., Debure, M., Durlet, C., Virgone, A., Gaucher, E.C., 2017. Volcanic rock alterations of the Kwanza Basin, offshore Angola - Insights from an integrated petrological, geochemical and numerical approach. Mar. Pet. Geol. 80, 394–411. https://doi.org/10.1016/j.marpetgeo.2016.12.020

Thomaz Filho, A., Milani, E.J., 2018. Rifting and magmatism associated with the South America and Africa Breakup. https://doi.org/10.25249/0375-7536.2000301017019

Trewin, N.H., Fayers, S.R., 2004. Sedimentary Rocks: Chert. Encycl. Geol. 51–62. https://doi.org/10.1016/B0-12-369396-9/00315-4

Tucker, M.E., 1990. Dolomites and dolomitization models, in: Carbonate Sedimentology. pp. 365–400.

Tucker, M.E., Bathurst, R.G.C., 2009. Carbonate Diagenesis. Carbonate Diagenes. 1–312. https://doi.org/10.1002/9781444304510

Utida, G., 2009. Fósseis em micritos Quaternários da Serra da Bodoquena, Bonito-MS e sua aplicação em estudos paleoambientais. Universidade de São Paulo (in Portuguese with English abstract).

Utida, G., Oliveira, E.C., Tucker, M., Petri, S., Boggiani, P.C., 2017. Palaeoenvironmental interpretations based on molluscs from mid-Holocene lacustrine limestones, Mato Grosso do Sul, Brazil. Quat. Int. 437. https://doi.org/10.1016/j.quaint.2016.11.007

Warren, J., 2000. Dolomite: occurrence, evolution and economically important associations. Earth-Science Rev. 52, 1–81. https://doi.org/10.1016/S0012-8252(00)00022-2

Welton, J.E., 2003. SEM Petrology Atlas, in: Lorenz, J.C. (Ed.), Methods in Exploration. AAPG Publications, Oklahoma, p. 240.

Wenk, H., Bulakh, A., 2004. Important information about silica material and feldspars, in: Minerals: Their Constitution and Origin. Cambridge University Press, Cambridge, p. 635. https://doi.org/10.5860/choice.42-2243

White, W.M., Klein, E.M., 2013. Composition of the Oceanic Crust, 2nd ed, Treatise on Geochemistry: Second Edition. Elsevier Ltd. https://doi.org/10.1016/B978-0-08-095975-7.00315-6

Whitney, D.L., Evans, B.W., 2010. Abbreviations for names of rock-forming minerals. Am. Mineral. 95, 185–187. https://doi.org/10.2138/am.2010.3371

Wright, P., Tosca, N.J., 2016. A Geochemical Model for the Formation of the Pre-Salt Reservoirs , Santos Basin, Brazil : Implications for Understanding Reservoir Distribution. AAPG Annu. Conv. Ehibition 51304, 32.

Zhang, F., Xu, H., Konishi, H., Roden, E.E., 2010. A relationship between d104 value and composition in the calcite-disordered dolomite solid-solution series. Am. Mineral. 95, 1650–1656. https://doi.org/10.2138/am.2010.3414